



HAL
open science

Imagerie polarimétrique active à large spectre pour l'amélioration du contraste et la microscopie.

Lijo Thomas

► **To cite this version:**

Lijo Thomas. Imagerie polarimétrique active à large spectre pour l'amélioration du contraste et la microscopie.. Optique [physics.optics]. Université Paris Saclay (COmUE), 2017. Français. NNT : 2017SACLO008 . tel-01696496

HAL Id: tel-01696496

<https://pastel.hal.science/tel-01696496>

Submitted on 30 Jan 2018

HAL is a multi-disciplinary open access archive for the deposit and dissemination of scientific research documents, whether they are published or not. The documents may come from teaching and research institutions in France or abroad, or from public or private research centers.

L'archive ouverte pluridisciplinaire **HAL**, est destinée au dépôt et à la diffusion de documents scientifiques de niveau recherche, publiés ou non, émanant des établissements d'enseignement et de recherche français ou étrangers, des laboratoires publics ou privés.

NNT : 2017SACL0008

THÈSE DE DOCTORAT
DE L'UNIVERSITÉ PARIS-SACLAY
PRÉPARÉE INSTITUT D'OPTIQUE GRADUATE
SCHOOL

Ecole doctorale n°575

Physique et ingénierie : électrons, photons, sciences du vivant
(EOBE)

Spécialité de doctorat : Physique

par

M. LIJO THOMAS

Broadband active polarization imaging for contrast improvement
and microscopy

Thèse présentée et soutenue à "Palaiseau", le 6 Novembre 2017.

Composition du Jury :

| | | | |
|------|----------------------|--|----------------------|
| M. | EMMANUEL BEAUREPAIRE | Directeur de Recherche École polytechnique, Palaiseau | (Président) |
| M. | XAVIER ORLIK | Maitre de Recherche ONERA, Toulouse | (Rapporteur) |
| M. | LAURENT BIGUÉ | Professeur Université de Haute Alsace | (Rapporteur) |
| M. | FRANÇOIS GOUDAIL | Professeur Institut d'Optique, Palaiseau | (Directeur de thèse) |
| Mme. | MYRIAM ZERRAD | Ingénieur de Recherche Institut Fresnel, Marseille | (Examinatrice) |
| M. | MATTHIEU BOFFETY | Maître de Conférences Institut d'Optique, Palaiseau | (Examineur) |

I dedicate my thesis to my father M.E. Thomas and late mother Rachel Thomas. I thank them for giving me an opportunity to learn and nurture my curiosity.

Acknowledgements

First and foremost, I want to thank my advisor Prof. François Goudail. It has been an honour to be his Ph.D. student. He instilled me scientific, moral and professional values which are necessary to become an experimental physicist. Because of his training, I value hard work, persistence and honesty in doing research more than ever. The joy and enthusiasm, he brought in doing research has inspired me in doing my job with full heart.

I am very grateful to my thesis co-supervisor Dr. Matthieu Boffety for his constant effort and patience to teach me technical and soft skills required to finish my thesis preparation. His professional training has sharpened my critical thinking and presentation skills. He has also been very kind to me.

I acknowledge the support of Dr. Enric Garcia -Caurel, Ecole Polytechnique (France) in preparation of my thesis. He has provided me the apparatus and administrative permission to carry out experiments in his laboratory to calibrate liquid crystal variable retarder.

I thank the members of Carl Zeiss corporate research team (Jena, Germany) for giving me an opportunity to work with phase contrast microscopy set up in the lab. I am grateful to Dr. Lars Stoppe and Dr. Christian Dietrich at Carl Zeiss for their mentorship. The professional experience gained from there expanded my horizons in research.

I also express my gratitude to Dr. Sylvania Pereira, TU Delft (Netherlands) for providing me an opportunity to work in the domain of interferometric coherent Fourier scatterometry. The short stint with her research team helped me to understand how I can use my scientific skills in different scientific domain.

I also thank the organizers of ADOPSYS – Marie Curie initial training network programme for providing this unique opportunity to work with different scientific partners during my Ph.D. The Ph.D project has received funding from European Union seventh framework programme for research, technological development and demonstration under grant agreement no. 608082. The professional and scientific training sessions organized by ADOPYS were beneficial to improve my skill sets in research. The opportunity to discuss and network with other partners have shown me the impact of networking in scientific research output.

I also thank the members of SPIM group, Charles Fabry laboratory at Institut d’Optique for their fruitful discussions and constructive criticism. The social events organized by the team helped me to prepare my thesis with more fun and colour.

Finally, I would like to thank my wife for her constant moral and emotional support. Without her love and support, my Ph.D. journey would not have been smooth. Thank you.

Lijo Thomas
Charles Fabry Laboratory
Institut d’Optique, Palaiseau
October 2017

Contents

| | |
|--|-----------|
| Introduction | 8 |
| 1 General concepts in optical polarization and polarimetric imaging | 9 |
| 1.1 Optical polarization | 9 |
| 1.1.1 Fresnel's wave theory | 9 |
| 1.1.2 Polarization ellipse | 11 |
| 1.1.3 The Poincaré Sphere | 12 |
| 1.1.4 Stokes Parameters | 14 |
| 1.1.5 Mueller Matrix | 17 |
| 1.2 Introduction to polarimetric imaging | 19 |
| 1.2.1 Mueller imaging | 20 |
| 1.2.2 Orthogonal state contrast imaging | 21 |
| 1.3 Conclusion | 22 |
| 2 Active polarimetric imager for contrast optimization under narrow spectrum illumination | 23 |
| 2.1 Formalism of the theory of detection | 23 |
| 2.1.1 The Detection problem | 23 |
| 2.1.2 Criterion for detection in noisy optical images | 24 |
| 2.1.3 Bhattacharya distance as criterion for contrast definition in noisy optical images | 25 |
| 2.2 Design of an active adaptive polarimetric imager for contrast optimization | 29 |
| 2.2.1 Principle of active polarimetric imaging | 29 |
| 2.2.2 Generation and analysis of polarization states of light | 30 |
| 2.2.3 Introduction of phase delay by liquid crystal variable retarder (LCVR) | 33 |
| 2.2.4 Design of active adaptive polarimetric imager for contrast optimization in narrow spectral band | 35 |
| 2.3 Conclusion | 37 |
| 3 Active adaptive polarimetric imager for contrast optimization in broadband polarimetric imaging | 39 |
| 3.1 Theoretical framework | 39 |
| 3.2 Numerical study | 40 |
| 3.2.1 Description of set-up used in the simulation | 40 |
| 3.2.2 Contrast calculation | 42 |
| 3.2.3 Discussion | 49 |
| 3.3 Experimental study | 49 |
| 3.3.1 Description of the experimental set-up | 49 |
| 3.3.2 Results and discussion | 49 |

| | | |
|----------|--|------------|
| 3.4 | Conclusion | 54 |
| 4 | Spectral bandwidth optimization using measurements of multi-spectral Mueller matrices | 55 |
| 4.1 | Calibration of LCVRs for multispectral applications | 55 |
| 4.2 | Contrast optimization in multispectral polarimetric imaging | 56 |
| 4.2.1 | Multispectral Mueller matrix of the scene | 57 |
| 4.2.2 | Numerical study | 59 |
| 4.2.3 | Experimental study | 61 |
| 4.3 | Contrast optimization in broadband polarimetric imaging | 64 |
| 4.3.1 | Numerical study | 64 |
| 4.3.2 | Experimental study | 68 |
| 4.4 | Conclusion | 69 |
| 5 | Polarization based differential phase contrast imaging | 73 |
| 5.1 | Introduction | 73 |
| 5.2 | Polarization based differential phase contrast imaging using LED illumination | 74 |
| 5.2.1 | LED array illumination | 74 |
| 5.2.2 | Differential phase contrast imaging using LEDs | 75 |
| 5.2.3 | LED based polarization differential phase contrast imaging | 78 |
| 5.3 | Experimental study of PDPC imaging | 80 |
| 5.3.1 | Experimental scheme to simulate proposed PDPC imaging scheme | 80 |
| 5.3.2 | Determination of polarizer extinction ratio | 82 |
| 5.3.3 | Results, analysis and discussion | 82 |
| 5.4 | Conclusion | 92 |
| | General conclusions | 93 |
| | Résumé de la thèse | 94 |
| A | Optimal contrast in the case of pure retarders for monoband architecture | 105 |

General Introduction

Context

Polarimetric imagers are useful to reveal information that is invisible to the human eye or to standard intensity imagers. This capability has been successfully applied to several fields such as industrial inspection, remote sensing, or biomedical imaging [1, 2, 3, 4, 5, 6, 7, 8]. There are two types of polarimetric imagers: passive and active. In passive polarimetric imagers, the source of illumination is natural sunlight. Since this light is depolarized, passive systems can only measure how the elements of the scene repolarize the incoming light. Although these systems have shown their capacity in such applications as long range remote sensing, they measure only a small part of the polarization information available in a scene. On the other hand, active polarimetric imagers can control both the polarization state of illumination and the way the polarization state of the light diffused by the scene is analyzed. They are thus sensitive to all the polarization properties of the scene, that are represented by its pixelwise Mueller matrix.

Polarimetric imagers often employ polarization modulation devices based on liquid crystal variable retarders (LCVR) to control the illumination and the analysis of polarization states [8, 9, 10, 11]. These devices are fast and precise, but they control the polarization state of light only at the wavelength they were designed for, and performance loss might be observed if imaging is performed at other wavelengths, due to their spectral dependence. We refer to this phenomenon as polarization chromatic aberration in the remainder of the thesis. If the light source that illuminates the scene has a broad spectrum (for example, a white light source), it is thus necessary to place a narrowband spectral filter in the imaging path [12, 13]. However, spectral filtering significantly reduces the amount of light entering the system and thus the signal-to-noise ratio of polarization images.

A way to overcome this issue is to achromatize the polarization modulators. However, this comes at the price of higher complexity and cost, and this may not be necessary if the objective is not to perform precise measurement of polarization properties, but to improve target detection performance by increasing the target/background discriminability (or contrast).

Recently, this issue has been investigated for passive polarimetric imagers, where the light scattered by the scene is analyzed by a chromatic polarization modulator called Polarization State Analyzer (PSA) based on LCVR [14]. It has been shown that despite the loss of polarization accuracy due to the apparition of polarization chromatic aberrations, the contrast is improved by broadening the spectrum of the light entering the system. Moreover, there is an optimal configuration of the PSA that maximizes this improvement. Thus, we can say that the spectral bandwidth should now be considered as a further parameter to optimize polarimetric imagers.

Objective and organization of the thesis

The first purpose of this thesis work was to address the same problem in the case of active polarimetric imagers where the illumination is also controlled by a chromatic polarization modulator called PSG (Po-

larization State Generator). This is an important challenge to solve since active polarization imagers can provide better contrast than passive ones thanks to the control of the polarization of illumination. However, the problem is more complex since broadening the spectrum now impacts both the PSA and PSG, that must be jointly optimized in order to increase target/background discriminability. We demonstrate that there exists configurations of the PSA and PSG for which the increase of light flux overcomes the polarization property mismatch of the system components caused by spectral broadening. We investigate the theoretical foundations of this result through numerical simulations and validate the results on images acquired with a real-world active polarimetric imager.

The second purpose of this thesis work was to collaborate with a company (Carl Zeiss) in order to improve their differential phase contrast microscopy setup using polarization technologies. I demonstrate that simple polarization devices make it possible to improve its speed of imaging and to reduce experimental complexity with no compromise in image quality.

In the first chapter of this manuscript, I begin with a review of basic concepts of optical polarization such as Fresnel's wave theory, Poincaré sphere, Stokes parameters, and Mueller matrix. Then I proceed to review the polarimetric imaging techniques such as Mueller imaging and orthogonal state contrast imaging which are used during the thesis. The objective of this chapter is to make the reader familiar with the required physical concepts and techniques necessary to appreciate the rest of the thesis.

In Chapter 2, I begin with discussion about the choice of the criteria to evaluate the separation between two regions in noisy optical images. Then I proceed to describe the principle of active polarimetric imaging, different methods of generation and analysis of polarization states of light, the construction of LCVR and how they function to introduce phase delay. In the last section, I discuss the design of active adaptive polarimetric imagers using LCVR and how they can be used for contrast optimization in the presence of illumination with narrow spectral bandwidth.

In Chapter 3, I explain and demonstrate how contrast of polarization image in low light imaging conditions can be improved by allowing wider spectral bandwidth in the imaging system. However, the PSG/PSA configuration optimal for a given wavelength may not be optimal when the spectral band is wider. Indeed, I demonstrate that the contrast can be enhanced further if PSG and PSA configurations are optimized taking into account the spectral bandwidth, the spectral dependence of LCVR response and the scene polarimetric properties. Finally, I note that the used optimization method is an exhaustive search procedure, and is therefore time consuming.

In chapter 4, I put forward a solution to conduct contrast optimization more efficiently with chromatic optical components. It consists in calibrating the variations of the phase delay introduced by chromatic LCVR with wavelength, and in measuring the multi-spectral Mueller matrix of the scene. By this way, I show that it is possible to run contrast optimization numerically with limited accuracy but with a time $(1/10)^{th}$ of exhaustive search. I also show experimentally that there exists an optimal bandwidth for which the contrast obtained with optimal setting of PSG and PSA is maximal.

In the final chapter, I present an application of polarimetric imaging in another domain of research : LED based differential phase contrast microscopy. Differential phase contrast imaging (DPC) using LED illumination is a phase imaging technique to image transparent biological specimen. This method works on the principle that phase gradient of a specimen can be extracted from two images illuminated and recorded at opposite illumination angles. The requirement of two images for the creation of DPC images decreases the speed of imaging and the intermittent flash associated with it may cause inconvenience for the user. The objective of this project is to reduce the number of images required to create DPC image from two to one as well as remove the requirement of intermittent flash. Using the knowledge of polarimetric imaging and after implementation of polarization optics in the imaging path, I show that this objective can be achieved for most biological samples except for birefringent ones.

Chapter 1

General concepts in optical polarization and polarimetric imaging

A review of important concepts in optics and imaging techniques which are necessary to comprehend rest of chapters is laid down here. This chapter discusses about concept of optical polarization, polarization ellipse, Poincaré sphere, Stokes vector, Mueller matrix, polarimetric imaging and liquid crystal variable retarders.

1.1 Optical polarization

Polarization is a fundamental property of light like intensity, wavelength and coherence, naturally detected by insects and many vertebrates other than mammals [15]. The scientific discovery of phenomenon of optical polarization is usually attributed to Erasmus Bartholinus (1670), a Danish mathematician at University of Copenhagen [16]. While working on light propagation through calcite crystals (rhombohedral), he discovered that when a beam of natural incident light propagated through the calcite crystal, two beams emerged with equal intensity, demonstrating that the incident light ray actually contains two type of rays called ordinary ray and extraordinary ray. Since these two rays refract at different angles, the calcite crystal is said to be doubly refractive or birefringent. It is important to note that both rays obey Snell's law but experience different refractive indices.

In 1672, Christian Huygens, a Dutch physicist, who became curious about the phenomenon of double refraction showed that by rotating a second calcite crystal about the direction of incident optical beam, the intensity of one beam was maximized and other beam was extinguished. As he rotated 90° further, the first beam appeared again and second beam got vanished. At a rotation of 45° , the intensities of two rays were equal. Due to this opposite behavior shown by emerging beams, they were said to be polarized.

1.1.1 Fresnel's wave theory

The three major phenomena of light such as interference, diffraction and polarization were explained by Augustin Jean Fresnel (1820)[16]. He proposed a theory of light now known as Fresnel's wave theory. Thereafter, Fresnel and Arago experimentally demonstrated that the optical field consisted of only two orthogonal components in the plane transverse to the direction of propagation. His theory postulated that the orthogonal components were $w_1(\mathbf{r}, t)$ and $w_2(\mathbf{r}, t)$, which he called "optical disturbances" [15]. But we now know that the optical disturbances can be represented by the electric field components of the electromagnetic field. Fresnel hypothesized that the field components are described by two equations known as the wave equations,

$$\nabla^2 E_x(\mathbf{r}, t) = \frac{1}{v^2} \frac{\partial^2 E_x(\mathbf{r}, t)}{\partial t^2}, \quad (1.1)$$

$$\nabla^2 E_y(\mathbf{r}, t) = \frac{1}{v^2} \frac{\partial^2 E_y(\mathbf{r}, t)}{\partial t^2}, \quad (1.2)$$

where $E_x(\mathbf{r}, t)$ and $E_y(\mathbf{r}, t)$ are the optical field components, \mathbf{r} is the radius vector to a point in space measured from the origin of a coordinate system, t is the time, v is the velocity of the waves, and ∇^2 is the Laplacian operator. The field components and the direction of propagation \mathbf{k} form an orthogonal system as shown in figure 1.1

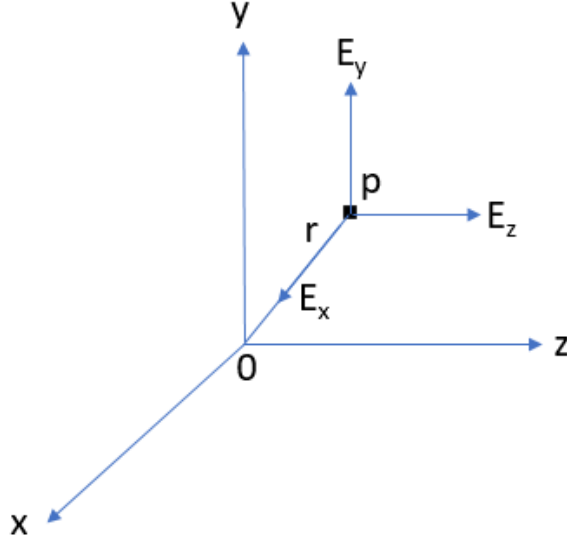


Figure 1.1: Orthogonal system which represents electric field components in x and y direction, and propagation vector \mathbf{k} in a direction perpendicular to both. O is the origin of coordinate system and p is a point in space where \mathbf{r} is the radius vector to that point from the origin.

The solutions of the wave equations are

$$E_x(\mathbf{r}, t) = E_{ox} \cos(\omega t - \mathbf{k} \cdot \mathbf{r} + \varphi_x) \quad (1.3)$$

$$E_y(\mathbf{r}, t) = E_{oy} \cos(\omega t - \mathbf{k} \cdot \mathbf{r} + \varphi_y), \quad (1.4)$$

where \mathbf{k} is the wave number and describes the direction of the propagation, and \mathbf{r} is a radius vector to the point 'p' in the field. In practice, the field is taken to be directed along the z-axis. The two components, above, can then be written as

$$E_x(z, t) = E_{0x} \cos(\omega t - kz + \varphi_x) \quad (1.5)$$

and

$$E_y(z, t) = E_{0y} \cos(\omega t - kz + \varphi_y), \quad (1.6)$$

where $\omega = 2\pi f$ is the angular frequency, $k = 2\pi/\lambda$ is the wave number, E_{0x} and E_{0y} are the maximum amplitudes and δ_x and δ_y are arbitrary phases; the term $\omega t - kz$ is called the propagator. The propagation of these two waves can be graphically represented as shown in figure 1.2.

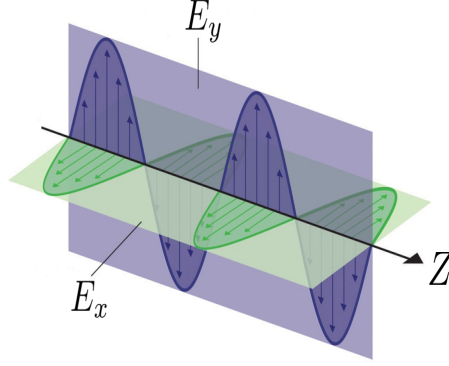


Figure 1.2: Propagation of electric field in the space.

1.1.2 Polarization ellipse

$E_x(z, t)$ and $E_y(z, t)$ as given in equation 1.5 and equation 1.6 describe sinusoidal oscillations of electric field in the x-z and y-z planes as presented in figure 1.2. As the field propagates, $E_x(z, t)$ and $E_y(z, t)$ give rise to a resultant vector. This vector describes a locus of points in space, and the equation of curve generated by these locus of points is given below:

$$\frac{E_x(z, t)^2}{E_{0x}^2} + \frac{E_y(z, t)^2}{E_{0y}^2} - \frac{2E_x(z, t)E_y(z, t)}{E_{0x}E_{0y}} \cos \varphi = \sin^2 \varphi, \quad (1.7)$$

where $\varphi = \varphi_y - \varphi_x$. It is derived by eliminating the time space propagator $wt - kz$ between two equations of $E_x(z, t)$ and $E_y(z, t)$ [17]. The above equation describes an ellipse in its non standard form and shows that at any instant of time the locus of points described by the optical field as it propagates is an ellipse. This behavior is spoken of as optical polarization. Because the equation refers to polarized light, the equation is also called the polarization ellipse. In figure 1.3, the ellipse is shown inscribed within a rectangle whose sides are parallel to the coordinate axes and whose lengths are $2E_{0x}$ and $2E_{0y}$. The presence of the cross term in equation 1.7 shows that the polarization ellipse is rotated, and this behavior is shown in figure 1.3 (rotated $\xi\eta$ coordinate system) where the ellipse is shown rotated through an angle ψ .

The parameters of the polarization ellipse

Let OX and OY be the initial, unrotated, axes, and let $O\xi$ and $O\eta$ be the rotated axes of the polarization ellipse. The angle between OX and $O\xi$, the major axis of unrotated and rotated axes is represented by orientation angle ψ ($0 \leq \psi \leq \pi$). The ellipticity of polarization ellipse is expressed by ellipticity angle χ ($-\pi/4 < \chi \leq \pi/4$). These two angular parameters are defined in terms of E_{0x} , E_{0y} and δ as given below [16] :

$$\tan 2\psi = \frac{2E_{0x}E_{0y}}{E_{0x}^2 - E_{0y}^2} \cos \varphi, \quad 0 \leq \psi \leq \pi, \quad (1.8)$$

$$\sin 2\chi = \frac{2E_{0x}E_{0y}}{E_{0x}^2 + E_{0y}^2} \cos \varphi, \quad -\pi/4 < \chi \leq \pi/4. \quad (1.9)$$

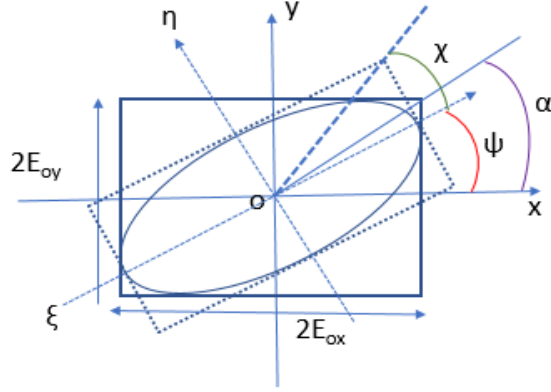


Figure 1.3: Polarization ellipse. Polarization ellipse is inscribed within a rectangle whose sides are parallel to coordinate axes and lengths are equal to $2E_{0x}$ and $2E_{0y}$. The ellipse is rotated at angle ψ (orientation angle) with respect to x-axis, χ is angle of ellipticity and α is axillary angle defined by equation 1.10.

These angles can be expressed completely in trigonometric form by introducing an angle called the auxiliary angle α defined by

$$\tan \alpha = \frac{E_{0y}}{E_{0x}}, \quad 0 \leq \alpha \leq \pi/2. \quad (1.10)$$

then above equations become

$$\begin{aligned} \tan 2\psi &= (\tan 2\alpha) \cos \varphi, \\ \sin 2\chi &= (\sin 2\alpha) \sin \varphi, \quad 0 \leq \varphi \leq 2\pi \end{aligned} \quad (1.11)$$

Degenerate polarization states

The optical field in general is represented as elliptically polarized, but there are several combinations of amplitude and phase that are possible and are very important. These are known as degenerate polarization states. They are linearly horizontal polarized light (LHP), linearly vertical polarized light (RHP), linear $+45^\circ$ polarized light (L+45P), linear -45° polarized light (L-45P), right circular polarized light (RCP) and left circular polarized light (LCP). A schematic description of degenerate polarization states along with mathematical conditions for their existence and corresponding polarization ellipses are shown in figure 1.1.

RCP light rotates clockwise and LCP rotates counter clockwise as it propogates towards observer. This is a widely accepted sign convention.

1.1.3 The Poincaré Sphere

The polarization ellipse is an instantaneous representation of polarized light. But the rotation angle and the ellipticity angle is not directly measurable. This representation added more difficulty to determine

| Polarization state | Graphical representation | Mathematical requirement for their existence |
|--------------------|---|--|
| LHP |  | $E_{0x} = E_0, \quad E_{0y} = 0$ |
| LVP |  | $E_{0x} = 0, \quad E_{0y} = E_0$ |
| L+45P |  | $E_{0x} = E_{0y} = E_0, \quad \delta = 0$ |
| L-45P |  | $E_{0x} = E_{0y} = E_0, \quad \delta = \pi$ |
| RCP |  | $E_{0x} = E_{0y} = E_0, \quad \delta = \pi/2$ |
| LCP |  | $E_{0x} = E_{0y} = E_0, \quad \delta = -\pi/2$ |

Table 1.1: Degenerate polarization states are shown in the figure. LHP - Linearly horizontal polarized light, LVP - Linearly vertical polarized light, L+45P - Linearly +45° polarized light, L-45P - Linearly -45° polarized light, RCP- Right circularly polarized light, LCP- Left circularly polarized light.

new angular parameters of a polarized light after it passes through several optical elements. In 1892, Henri Poincaré addressed this problem and could solve the issue by introducing sphere to represent polarized state of light. The sphere is known as Poincaré sphere. The following figure shows Poincaré sphere in Cartesian (x,y,z axes) and spherical coordinate system ($2\psi, 2\chi$ angles). Assuming the sphere has unit radius, the Cartesian coordinates are related to spherical coordinate system by following relations

$$\begin{aligned} x &= \cos 2\chi \cos 2\psi, & -\pi/2 \leq 2\chi \leq \pi/2, \\ y &= \cos 2\chi \sin 2\psi, & 0 \leq 2\psi \leq 2\pi, \\ z &= \sin 2\chi, \end{aligned} \tag{1.12}$$

where $x^2 + y^2 + z^2 = 1$ for a sphere of unit radius.

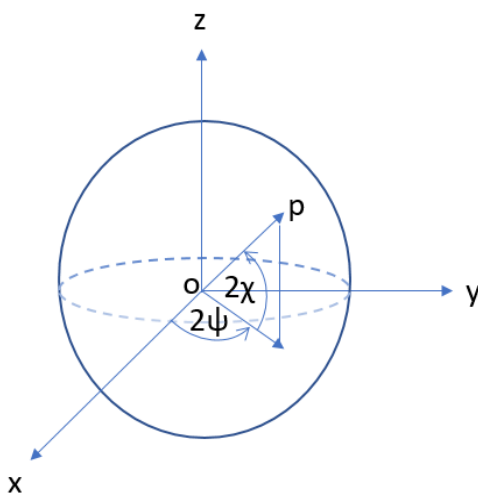


Figure 1.4: Poincaré sphere of unit radius presented in cartesian as well as spherical coordinate system.

Degenerate states on the Poincaré sphere

Any polarized state of light can be represented on Poincaré sphere by coordinate pair ($2\psi, 2\chi$). The degenerate states on the Poincaré sphere are LHP ($0^\circ, 0^\circ$), LVP ($180^\circ, 0^\circ$), L+45P ($90^\circ, 0^\circ$), L-45P ($270^\circ, 0^\circ$), RCP ($0^\circ, -90^\circ$) and LCP ($0^\circ, 90^\circ$). As you can observe from the figure 1.5, all linear polarization states are lying on the equator of sphere, circular polarization states such as left circular polarization states and right circular polarization states are at the north and south pole respectively. Elliptical polarization states are represented elsewhere on the Poincaré sphere.

1.1.4 Stokes Parameters

The representation of light by polarization ellipse is convenient because a single equation can explain different forms of polarization. However this form of representation is inadequate as we deal with depolarization of light. Depolarization is the phenomenon of changing polarized light into unpolarized light. In a plane transverse to the propagation direction, the electric field vector traces out an ellipse or special cases

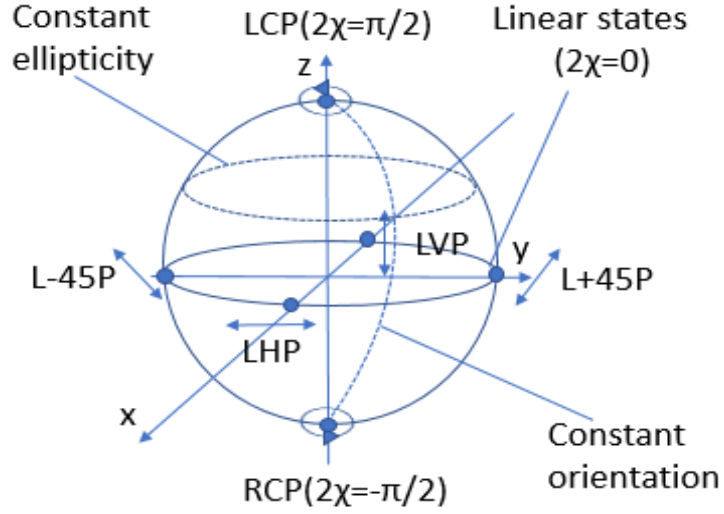


Figure 1.5: Visual representation of degenerate states on the Poincaré sphere.

| Polarization state of light | $(2\psi, 2\chi)$ |
|-----------------------------|------------------------|
| LHP | $(0^\circ, 0^\circ)$ |
| LVP | $(0^\circ, 180^\circ)$ |
| L+45P | $(90^\circ, 0^\circ)$ |
| L-45P | $(270^\circ, 0^\circ)$ |
| LCP | $(0^\circ, 90^\circ)$ |
| RCP | $(0^\circ, -90^\circ)$ |

Table 1.2: The table presents the orientation angle ψ and the ellipticity angle χ of degenerate polarization states of light presented in figure 1.5.

of ellipse (circle/line) in a time interval of 10^{-15} s. Thus following polarization ellipse to observe change in polarization state of light is impossible since time is too short. The other disadvantage of polarization ellipse is that it can represent neither unpolarized light or partially polarized light but completely polarized light. In 1852, Sir George Gabriel Stokes found out that the polarization behavior of light can be represented in terms of observables/measurable [15]. A set of four measurables can represent any polarized state of light. They are known as Stokes parameters. To determine measurable of the polarized light, we take the time average of quadratic forms of the electric field of polarization ellipse. Applying the time average definition to the polarization ellipse then yields the following equation :

$$\begin{aligned}
S_0^2 &= S_1^2 + S_2^2 + S_3^2, \\
\text{where } S_0 &= E_{0x}^2 + E_{0y}^2, \\
S_1 &= E_{0x}^2 - E_{0y}^2, \\
S_2 &= 2E_{0x}E_{0y} \cos \varphi, \\
S_3 &= 2E_{0x}E_{0y} \sin \varphi, \quad \varphi = \varphi_y - \varphi_x.
\end{aligned} \tag{1.13}$$

These four quantities S_0 , S_1 , S_2 and S_3 are the observables of polarized light. They are experimentally measurable and therefore real quantities. The first Stokes parameter S_0 describes the total intensity of the light, S_1 describes the dominance of LHP over LVP light, S_2 describes the dominance of L+45P over L-45P light and S_3 describes the dominance of RCP over LCP light. Stokes parameters are often written in the form of column matrix that is termed as Stokes vector. For example, Stokes vector for an elliptically, purely polarized light is written as

$$\mathbf{S} = \begin{pmatrix} S_0 \\ S_1 \\ S_2 \\ S_3 \end{pmatrix} = \begin{pmatrix} E_{0x}^2 + E_{0y}^2 \\ E_{0x}^2 - E_{0y}^2 \\ 2E_{0x}E_{0y} \cos \varphi \\ 2E_{0x}E_{0y} \sin \varphi \end{pmatrix}$$

The Stokes vectors for the degenerate polarization states are given below :

$$\begin{aligned}
\mathbf{S}_{LHP} &= I_0 \begin{pmatrix} 1 \\ 1 \\ 0 \\ 0 \end{pmatrix}, \quad \mathbf{S}_{LVP} = I_0 \begin{pmatrix} 1 \\ -1 \\ 0 \\ 0 \end{pmatrix}, \quad \mathbf{S}_{L+45P} = I_0 \begin{pmatrix} 1 \\ 0 \\ 1 \\ 0 \end{pmatrix}, \\
\mathbf{S}_{L-45P} &= I_0 \begin{pmatrix} 1 \\ 0 \\ -1 \\ 0 \end{pmatrix}, \quad \mathbf{S}_{RCP} = I_0 \begin{pmatrix} 1 \\ 0 \\ 0 \\ 1 \end{pmatrix}, \quad \mathbf{S}_{LCP} = I_0 \begin{pmatrix} 1 \\ 0 \\ 0 \\ -1 \end{pmatrix},
\end{aligned}$$

where I_0 is the intensity. The Stokes parameters are related to the orientation and ellipticity angles, ψ and χ , associated with Poincaré sphere as follows:

$$\begin{aligned}
S_1 &= S_0 \cos 2\chi \cos 2\psi, \\
S_2 &= S_0 \cos 2\chi \sin 2\psi, \\
S_3 &= S_0 \sin 2\chi,
\end{aligned} \tag{1.14}$$

and

$$\psi = \frac{1}{2} \tan^{-1} \left(\frac{S_2}{S_1} \right), \quad 0 \leq \psi \leq \pi,$$

$$\chi = \frac{1}{2} \sin^{-1}\left(\frac{S_3}{S_0}\right), \quad -\frac{\pi}{4} \leq \chi \leq \frac{\pi}{4}.$$

Stokes parameters can present completely polarized, unpolarized and partially polarized light. The Stokes vector for unpolarized light is given below:

$$\mathbf{S}_{unp} = S_0 \begin{pmatrix} 1 \\ 0 \\ 0 \\ 0 \end{pmatrix},$$

where S_0 is the first Stokes parameter(total intensity). The terms S_1 , S_2 and S_3 are zero because there are no amplitude and phase relations between orthogonal components of electric field. Partially polarized light can be considered as a mixture of completely polarized light and unpolarized light. Therefore we can present its Stokes vector as:

$$\mathbf{S} = S_0 \begin{pmatrix} 1 \\ \mathbf{s} \end{pmatrix} = (1 - \rho)S_0 \begin{pmatrix} 1 \\ \mathbf{s} \end{pmatrix} + \rho S_0 \begin{pmatrix} 1 \\ \mathbf{s} \end{pmatrix}, \quad 0 \leq \rho \leq 1, \quad (1.15)$$

where \mathbf{s} is reduced Stokes vector and ρ is called the degree of polarization(DOP). The DOP is defined as :

$$\rho = \frac{I_{pol}}{I_{tot}} = \frac{\sqrt{S_1^2 + S_2^2 + S_3^2}}{S_0}, \quad 0 \leq \rho \leq 1 \quad (1.16)$$

where I_{tot} is the total intensity. For completely polarized light, $\rho = 1$, unpolarized light, $\rho=0$ and for partially polarized light, the value of ρ is between 0 and 1. Therefore in general we can express relation between Stokes parameters as given below:

$$S_0^2 \geq S_1^2 + S_2^2 + S_3^2, \quad (1.17)$$

where = and > sign point to the condition where light is completely polarized and partially/unpolarized light respectively.

1.1.5 Mueller Matrix

The polarization state of light can be modified by changing the three parameters of the polarization ellipse. They are orthogonal amplitudes and phase between them. This can be achieved by using polarizing optical elements such as polarizers and phase retarders/waveplates but this is a controlled transformation of polarization state of light. The transformation of polarization state of light is also observed when polarized optical beam interacts with polarizing material which shows birefringence, diattenuation or depolarization properties. Let us consider the state of polarization of incident light is represented by Stokes vector \mathbf{S} and state of polarization of outgoing optical beam after interaction with polarizing material is \mathbf{S}' . Assuming that the nature of the transformation of the electric field is linear, it can be shown that \mathbf{S} and \mathbf{S}' are linearly related by transformation matrix known as Mueller Matrix \mathbf{M} . It represents polarizing elements. The mathematical expression for relation is given below:

$$\mathbf{S}' = \mathbf{M}\mathbf{S} \quad (1.18)$$

If we expand the above equation, we get the following relation :

$$\begin{pmatrix} S'_0 \\ S'_1 \\ S'_2 \\ S'_3 \end{pmatrix} = \begin{pmatrix} m_{00} & m_{01} & m_{02} & m_{03} \\ m_{10} & m_{11} & m_{12} & m_{13} \\ m_{20} & m_{21} & m_{22} & m_{23} \\ m_{30} & m_{31} & m_{32} & m_{33} \end{pmatrix} \begin{pmatrix} S_0 \\ S_1 \\ S_2 \\ S_3 \end{pmatrix}. \quad (1.19)$$

All the elements in Mueller matrix \mathbf{M} are real quantities.

Mueller matrix of rotator

One way to change state of polarization is allowing optical field to pass through rotator. The property of a rotator is that it can rotate the polarization ellipse of incoming optical beam but it cannot change the ellipticity of polarization ellipse [18]. The Mueller matrix for rotator is expressed as

$$\mathbf{M}_{rot}(\theta) = \begin{pmatrix} 1 & 0 & 0 & 0 \\ 0 & \cos 2\theta & -\sin 2\theta & 0 \\ 0 & \sin 2\theta & \cos 2\theta & 0 \\ 0 & 0 & 0 & 1 \end{pmatrix}, \quad (1.20)$$

where θ is the angle of rotation. As light propagates through a rotator, the polarization ellipse is rotated by an angle θ and this can be observed from change in the orientation angle in following relation which expresses mathematically such a situation:

$$\begin{aligned} S' = \begin{pmatrix} S'_0 \\ S'_1 \\ S'_2 \\ S'_3 \end{pmatrix} &= \begin{pmatrix} 1 & 0 & 0 & 0 \\ 0 & \cos 2\theta & -\sin 2\theta & 0 \\ 0 & \sin 2\theta & \cos 2\theta & 0 \\ 0 & 0 & 0 & 1 \end{pmatrix} \begin{pmatrix} 1 \\ \cos 2\chi \cos 2\psi \\ \cos 2\chi \sin 2\psi \\ \sin 2\chi \end{pmatrix} \\ &= \begin{pmatrix} 1 \\ \cos 2\chi \cos(2\psi + 2\theta) \\ \cos 2\chi \sin(2\psi + 2\theta) \\ \sin 2\chi \end{pmatrix}. \end{aligned} \quad (1.21)$$

Thus if a polarizer or wave plate with Mueller matrix \mathbf{M} . is rotated through an angle θ with respect to x-axis, the Mueller matrix for rotated component, $\mathbf{M}(\theta)$ is calculated by following relation :

$$\mathbf{M}(\theta) = \mathbf{M}_{rot}(-\theta)\mathbf{M}\mathbf{M}_{rot}(\theta). \quad (1.22)$$

Mueller matrix of polarizer

The optical device that changes the amplitude of light field by selective absorption is known as linear polarizer. The absorption coefficients known as p_x and p_y in amplitude domain are designed differently along x and y- axis of the optical device. For complete absorption, $p_{i=x/y} = 0$ and for complete transmission, $p_{i=x/y} = 1$. Let us consider an ideal linear polarizer whose axis is rotated at an angle θ with respect to x-axis, the Mueller matrix \mathbf{M}_{LP} is represented as[19]

$$\mathbf{M}_{LP}(\theta) = \frac{1}{2} \begin{pmatrix} 1 & \cos 2\theta & \sin 2\theta & 0 \\ \cos 2\theta & \cos^2 2\theta & \sin 2\theta \cos 2\theta & 0 \\ \sin 2\theta & \sin 2\theta \cos 2\theta & \sin^2 2\theta & 0 \\ 0 & 0 & 0 & 0 \end{pmatrix}. \quad (1.23)$$

Thus for $\theta = 0^\circ, 45^\circ, 90^\circ$ and 135° , Mueller matrix of linear polarizer will take following forms:

$$\begin{aligned}
\mathbf{M}_{LHP} &= \frac{1}{2} \begin{pmatrix} 1 & 1 & 0 & 0 \\ 1 & 1 & 0 & 0 \\ 0 & 0 & 0 & 0 \\ 0 & 0 & 0 & 0 \end{pmatrix}, & \mathbf{M}_{L+45P} &= \frac{1}{2} \begin{pmatrix} 1 & 0 & 1 & 0 \\ 0 & 0 & 0 & 0 \\ 1 & 0 & 1 & 0 \\ 0 & 0 & 0 & 0 \end{pmatrix}, \\
\mathbf{M}_{LVP} &= \frac{1}{2} \begin{pmatrix} 1 & -1 & 0 & 0 \\ -1 & 1 & 0 & 0 \\ 0 & 0 & 0 & 0 \\ 0 & 0 & 0 & 0 \end{pmatrix}, & \mathbf{M}_{L-45P} &= \frac{1}{2} \begin{pmatrix} 1 & 0 & -1 & 0 \\ 0 & 0 & 0 & 0 \\ -1 & 0 & 1 & 0 \\ 0 & 0 & 0 & 0 \end{pmatrix}.
\end{aligned} \tag{1.24}$$

Mueller matrix of wave plate

Wave plates are optical devices which have property that incoming optical field experiences a phase shift of $-\phi/2$ along x-axis(slow axis) and $\phi/2$ along y-axis(fast axis). The Mueller matrix of a rotated wave plate is represented as [19]

$$\mathbf{M}_{wp}(\theta, \varphi) = \begin{pmatrix} 1 & 0 & 0 & 0 \\ 0 & \cos^2 2\theta + \cos \varphi \sin^2 2\theta & \cos 2\theta \sin 2\theta (\cos \varphi - 1) & \sin \varphi \sin 2\theta \\ 0 & \sin 2\theta \cos 2\theta (\cos \varphi - 1) & \sin^2 2\theta + \cos \varphi \cos^2 2\theta & \sin \varphi \cos 2\theta \\ 0 & -\sin \varphi \sin 2\theta & -\sin \varphi \cos 2\theta & \cos \varphi \end{pmatrix}, \tag{1.25}$$

where θ, φ are the angle of rotation and phase delay between the eigen polarization states.

For a rotation angle $\theta = 0^\circ$, Mueller matrix of waveplate becomes

$$\mathbf{M}_{wp}(\theta = 0^\circ, \varphi) = \begin{pmatrix} 1 & 0 & 0 & 0 \\ 0 & 1 & 0 & 0 \\ 0 & 0 & \cos \varphi & \sin \varphi \\ 0 & 0 & -\sin \varphi & \cos \varphi \end{pmatrix}. \tag{1.26}$$

There are two kind of non variable wave plates used in optics domain to introduce phase delay in incoming light. They are half wave plate and quarter wave plate. Mueller matrix for a half wave plate is written as

$$\mathbf{M}_{hwp}(\theta = 0^\circ, \varphi = \pi) = \begin{pmatrix} 1 & 0 & 0 & 0 \\ 0 & 1 & 0 & 0 \\ 0 & 0 & -1 & 0 \\ 0 & 0 & 0 & -1 \end{pmatrix} \tag{1.27}$$

and Mueller matrix for a quarter wave plate is written as

$$\mathbf{M}_{qwp}(\theta = 0^\circ, \varphi = \pi/2) = \begin{pmatrix} 1 & 0 & 0 & 0 \\ 0 & 1 & 0 & 0 \\ 0 & 0 & 0 & 1 \\ 0 & 0 & -1 & 0 \end{pmatrix}. \tag{1.28}$$

1.2 Introduction to polarimetric imaging

Polarimetric imaging is a process of measuring the polarization state of light emerging from an optical element or scattered from a scene in order to generate an intensity image which describes polarization properties of the object under observation[2]. This technique provides details such as surface features, shape, roughness etc., and it reveal contrasts when objects in the scene have similar intensity variation but different polarization properties. Polarimetric imaging involves illumination of a scene with polarized

light generated by polarization state generator (PSG) and analyzing polarized light scattered from the scene using polarization state analyzer (PSA). A simple configuration of PSG/PSA contains a linear polarizer and a waveplate but configuration gets complicated as flexibility in polarization state generation/detection increases. A schematic diagram

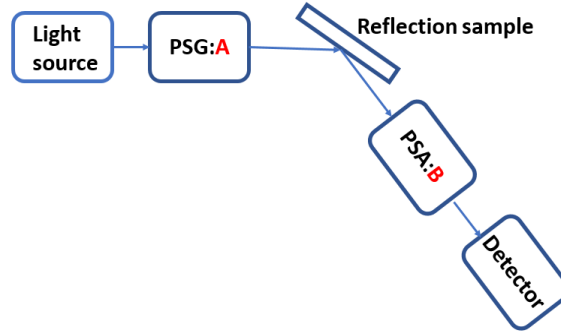


Figure 1.6: Schematic diagram of polarimetric imaging in reflection configuration.

Polarimetric imaging is classified into active and passive polarimetric imaging based on control over generation of polarized light. In active polarimetric imaging, the illumination of sample as well as analysis of polarized light from sample is controlled whereas in passive polarimetric imaging, only analysis of polarization state of light is controlled. There are different types of polarimetric imaging techniques such as Stokes imaging, orthogonal state contrast imaging, Mueller imaging or fully adaptive scalar imaging. I will discuss only few of them in the following section, which are important in the context of my work.

1.2.1 Mueller imaging

The purpose of Mueller imaging polarimeter is to measure spatially dependent polarization properties of sample/optical systems in the form of Mueller matrix. It is possible to compute polarization altering property of sample such as diattenuation, retardance, depolarization and polarizance from Mueller matrix [20]. Diattenuation is the property of an optical element or system whereby the intensity transmittance of the exiting beam depends on the polarization state of the incident beam. The intensity transmittance is a maximum for one incident state, and a minimum for the orthogonal state [21]. Retardance is the polarization dependent phase change associated with a polarizing element or system. The phase of the output beam depends upon the polarization state of input beam [21]. Depolarization is the phenomenon of decreasing the degree of polarization of the input light, and the polarizance consists of increasing the degree of polarization of input light [22].

We consider a Mueller polarimeter which performs 16 measurements to estimate the Mueller matrix of a sample. Let us denote Mueller matrix \mathbf{M} , which is to be estimated as

$$\begin{pmatrix} m_{00} & m_{01} & m_{02} & m_{03} \\ m_{10} & m_{11} & m_{12} & m_{13} \\ m_{20} & m_{21} & m_{22} & m_{23} \\ m_{30} & m_{31} & m_{32} & m_{33} \end{pmatrix} \quad (1.29)$$

We perform 16 measurements because we have 16 variables to estimate. The measurement system contains an unpolarized light source of intensity I_0 , a polarization state generator (PSG) with matrix of states A ,

and a polarization state analyzer (PSA) with a matrix of states \mathbf{B} . The matrices \mathbf{A} and \mathbf{B} contains a set of 4 stokes vectors used in illumination and analysis respectively to acquire Mueller matrix. They are represented as:

$$\mathbf{U} = \frac{1}{2} \begin{pmatrix} 1 & 1 & 1 & 1 \\ \mathbf{s}_1^U & \mathbf{s}_2^U & \mathbf{s}_3^U & \mathbf{s}_4^U \end{pmatrix} \quad (1.30)$$

where $\mathbf{U} = \{\mathbf{A}, \mathbf{B}\}$ and $[1, \mathbf{s}_i^U]^T$ are the unit intensity Stokes vectors of the polarization states used. The intensities measured from the scene are represented as

$$I = I_0 \mathbf{B}^T \mathbf{M} \mathbf{A} \quad (1.31)$$

where T denotes transpose of the matrix, I is a 4×4 matrix containing the intensities obtained from 16 measurements using the polarization states defined in matrices \mathbf{A} and \mathbf{B} . To simplify the equation, we consider that we are determining the Mueller matrix $I_0 \mathbf{M}$, thus equation 1.31 is rewritten as

$$\mathbf{V}_I = [\mathbf{B} \otimes \mathbf{A}]^T \mathbf{V}_M \quad (1.32)$$

where \otimes denote Kronecker product, V_M and V_I are 16 dimensional vectors obtained by reading $I_0 M$ and I in the lexicographic order respectively. To estimate the Mueller matrix (i.e V_M) from intensity measurements (V_I), we just have to invert equation 1.32:

$$\mathbf{V}_M = \{[\mathbf{B} \otimes \mathbf{A}]^T\}^{-1} \mathbf{V}_I = [(\mathbf{B}^T)^{-1} \otimes (\mathbf{A}^T)^{-1}] \mathbf{V}_I \quad (1.33)$$

If the noise is additive Gaussian noise with zero mean or Poisson distributed, then V_M is an unbiased estimator since [23] :

$$\langle \mathbf{V}_M \rangle = [\mathbf{B}^T \otimes \mathbf{A}^T]^{-1} \langle \mathbf{V}_I \rangle = \mathbf{V}_M \quad (1.34)$$

where $\langle \cdot \rangle$ is the ensemble average. The above equation represents Mueller matrix in lexicographic order.

1.2.2 Orthogonal state contrast imaging

Orthogonal state contrast (OSC) imaging is a simple case of active polarimetric imaging used in the domain of remote sensing, machine vision and biomedical applications to detect a target from the background [24, 25]. Imaging consists of illuminating the sample with purely polarized light generated by PSG and light scattered from the sample is analyzed by PSA. This imaging technique requires only two images to define OSC contrast of an image. The first intensity image is generated with the fraction of the backscattered light polarized parallel to the incident light, and the second image with light polarized perpendicular to the incident light.

Let us consider recording two intensity images as given below:

$$I_1(i, j) = \mathbf{S}^T \mathbf{M}(\mathbf{i}, \mathbf{j}) \mathbf{S}, \quad (1.35)$$

$$I_2(i, j) = \mathbf{S}_\perp^T \mathbf{M}(\mathbf{i}, \mathbf{j}) \mathbf{S}, \quad (1.36)$$

where \mathbf{S} represents unit norm, totally polarized Stokes vector, \mathbf{S}_\perp represents Stokes vector orthogonal to \mathbf{S} , $\mathbf{M}(\mathbf{i}, \mathbf{j})$ is Mueller matrix at the pixel with the coordinates (\mathbf{i}, \mathbf{j}) , then OSC contrast is defined as:

$$OSC = \frac{I_1(i, j) - I_2(i, j)}{I_1(i, j) + I_2(i, j)} \quad (1.37)$$

It is to be noted that the polarization state of incident light need not be linear but may be any pure polarized state of light defined on the Poincaré sphere. The OSC image contains information about intensity ($I_1(i, j) + I_2(i, j)$) as well as polarization.

1.3 Conclusion

In this chapter, we discussed the important physical concepts of optical polarization such as Fresnel's wave theory, polarization ellipse, Poincaré sphere, Stokes vectors and Mueller matrix. The Stokes - Mueller formalism is a useful mathematical representation of the interaction of polarized light with matter. We also reviewed two types of polarimetric imaging techniques : Mueller imaging and orthogonal state contrast imaging, which were used extensively in the preparation of this thesis. These physical concepts and imaging techniques are very useful to appreciate the rest of chapters.

Chapter 2

Active polarimetric imager for contrast optimization under narrow spectrum illumination

Contrast optimization of polarimetric images is a subject covering both the field of theory of detection and polarimetric imaging. Therefore, we briefly discuss the theory of detection, the definition of Bhattacharya distance as contrast parameter in noisy optical images, the principle and the architecture of active adaptive polarimetric imagers and finally the theory of contrast optimization in narrow spectral band polarimetric imaging.

2.1 Formalism of the theory of detection

The objective of optimizing contrast in an image is to detect the presence of an object/event of our interest distinctively from its background. We thus have two hypotheses to choose : (a) target is present (b) target is absent. The problem of decision to choose between the two hypotheses is called the detection problem. Generally, we are provided with a data set to determine the right hypothesis. Let us assume that a N-point data set $\{\mathbf{x}(1), \mathbf{x}(2) \cdots \mathbf{x}(N)\}$ is available. To arrive on a decision, we first form a function of the data $T(\mathbf{x}(1), \mathbf{x}(2), \cdots \mathbf{x}(N))$ and then make a decision by comparing its value to a threshold. Determining the function T and mapping it into a decision is the central problem of detection theory [26]. The steps followed in the theory of detection are:

- definition of the problem
- definition of a criterion for detection quality
- determination of an algorithm that optimizes the criterion

and if a statistical noise model is given, it is possible to determine an optimal detection method.

2.1.1 The Detection problem

Let us consider a sample image \mathbf{A} of size $M \times N$ which consists of only two types of regions. Let us call the region of our interest as target (t) and the other region as background (b). The signal in this example is the intensity information $\mathbf{I} = \{I_1, I_2, I_3 \cdots, I_{MN}\}$ contained in each pixel. The signal \mathbf{I} belongs to a set Ω which is in general subspace of $R^{M \times N}$. The set itself is divided in two regions ω_0 and ω_1 . The decision

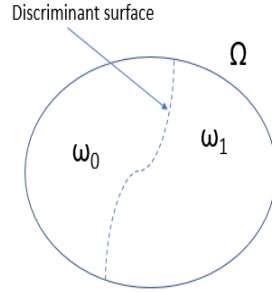


Figure 2.1: Space Ω , decision regions and discriminant surface.

taken on signal is based on which region it belongs to in set Ω . If the signal lies in the region ω_k , it is said to belong to class γ_k . In the present context, there are only two classes : γ_0 (target is absent) and γ_1 (target is present). A discrimination criterion will thus associate each of class γ_k with a region ω_k in the space Ω of all the possible signals. This operation defines the "frontier" between regions known as the discriminating surface. Since the signal \mathbf{I} necessarily belongs to Ω , the set of regions ω_k forms a partition of the space Ω (see figure 2.1).

For any detection problem, the discriminating surface can be represented by a real-value function of the measured signal $g(\mathbf{I})$, such that:

- If $g(\mathbf{I}) < \mu$, one decides that the signal belongs to the class γ_0
- If $g(\mathbf{I}) \geq \mu$, one decides that the signal belongs to the class γ_1

The function $g(\mathbf{I})$ is called the discriminant function and it is important to define the best threshold μ such that least possible classification error is achieved. In the following section, we will discuss the possible errors that can be encountered in a detection problem.

2.1.2 Criterion for detection in noisy optical images

The signal measured by a detector is often perturbed by noise and is thus considered as random vector. This noise generates errors in detection process that are termed as detection errors. Let us introduce some definitions which will allow us subsequently to describe these errors :

- **A priori probability density**, denoted as $P(\gamma_k)$, is the probability of observing an element of class γ_k independently of the signal measurement. In the case of detection problem, $P(\gamma_0) + P(\gamma_1) = 1$ since the signal necessarily belongs to one of the two classes.
- The **likelihood**, denoted as $P(\mathbf{I}|\gamma_k)$, is defined as the probability of observing a realization of the signal knowing the class to which it belongs. Its expression changes with noise model.
- **Bayes relation** : The joint probability density of a priori probability density and likelihood $P(\mathbf{I}, \gamma_k)$, is expressed by Bayes relation $P(\mathbf{I}, \gamma_k) = P(\mathbf{I}|\gamma_k)P(\gamma_k)$.
- The **posterior probability density**, denoted by $P(\gamma_k|\mathbf{I})$, corresponds to the probability that the signal \mathbf{I} observed corresponds to the class γ_k . It is expressed as $P(\gamma_k|\mathbf{I}) = \frac{P(\mathbf{I}, \gamma_k)}{P(\mathbf{I})}$.

There exists only two types of errors in detection problem. They are:

- **Probability of non detection** (P_{nd}): An observer decides that the signal belongs to γ_0 while it actually belongs to γ_1 . This type of error is known as P_{nd} . Mathematically, it is represented as:

$$P_{nd} = \int_{\omega_0} P(\mathbf{I}|\gamma_1)d\mathbf{I} \quad (2.1)$$

It is the probability that a signal belongs to class γ_1 but lies in the region ω_0 , and is thus associated with class γ_0 .

- **Probability of false alarm** (P_{fa}): An observer decides that the signal belongs to class γ_1 whereas it actually belongs to class γ_0 . The probability of this type of error is known as P_{fa} . It is represented as

$$P_{fa} = \int_{\omega_1} P(\mathbf{I}|\gamma_0)d\mathbf{I} \quad (2.2)$$

One would like to reduce the probabilities of occurrence of these two types of errors. Determination of detection algorithm is equivalent to drawing the regions ω_0 and ω_1 in set Ω . One can try to reduce P_{nd} by deciding that $\omega_1 = \Omega$ (whatever the signal) but this increases P_{fa} to 100%. Reducing the size of ω_1 would reduce P_{fa} but it will result in increase of P_{nd} . Therefore, one has to consider a trade off between P_{nd} and P_{fa} .

In fact, the optimal detection algorithm is that which minimizes P_{nd} for a given value of P_{fa} . It can be shown that the discriminant function of this optimal algorithm is the likelihood ratio [26]:

$$R(\mathbf{I}) = \frac{\mathbf{P}(\mathbf{I}|\gamma_1)}{\mathbf{P}(\mathbf{I}|\gamma_0)} \quad (2.3)$$

The "discriminability" of a target and a background is thus given by the detection probability for a given false alarm property obtained when the likelihood ratio detector is used. However, in general, these probabilities are difficult to compute. One thus prefers to use an other approach to define discrimination criteria, that is defined in the next section.

2.1.3 Bhattacharya distance as criterion for contrast definition in noisy optical images

We need to define a criterion capable of characterizing the separation between two sets of data (target and background) for any statistics. From literature survey, we found that Bhattacharya distance is a robust criteria to quantify separability of target from the background which we will call 'contrast' between target and background [27].

The Bhattacharya distance is an asymptotic exponent of the probability of error in a discrimination problem [28, 29]. To understand this concept, let us consider two probability distribution functions (pdf), $P_t(i)$ (target) and $P_b(i)$ (background), which belong to same family of probability laws but have different and unknown parameters. In our case these are probability densities associated with target (t) and background (b). The Bhattacharya distance between these two pdfs is given by the following formula [27]:

$$B_{t,b} = -\ln \left[\int_D [P_t(i)P_b(i)]^{1/2} di \right], \quad (2.4)$$

where D is the domain in which $P_t(I)$ and $P_b(I)$ are defined. The Bhattacharya distance is thus a scalar quantity which quantifies similarity between two distributions. The range of $B_{t,b}$ varies from 0 to $+\infty$. $B_{t,b} = 0$ means a complete overlap between two statistical distributions and $B_{t,b} \rightarrow \infty$ means that two

distributions are well separated. In case of detection problem, positive, large $B_{t,b}$ value is ideal. A visual representation of the evolution of $B_{t,b}$ as a function of the degree of overlapping is shown in figure 2.2. Table 2.1 shows examples of common statistical distributions that may be encountered in optical imaging, their probability density functions and the corresponding Bhattacharya distance.

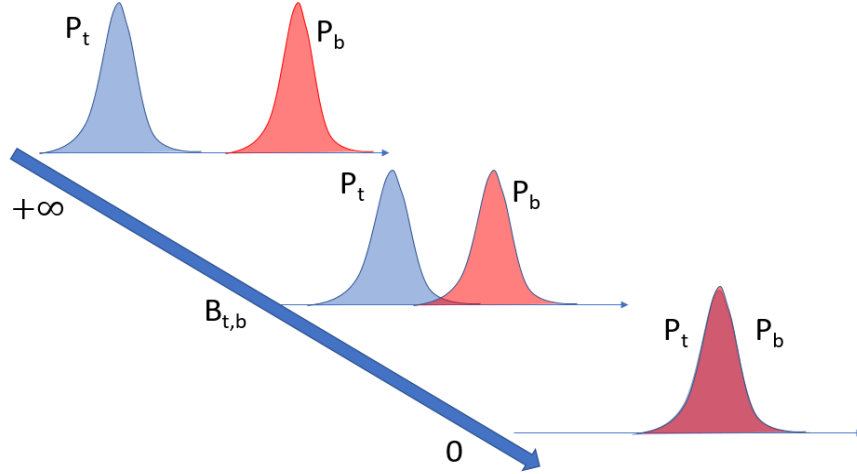


Figure 2.2: Evolution of the Bhattacharya distance ($B_{t,b}$) as a function of overlap of probability distribution functions (P_t and P_b) of two sets of data.

| Statistics | Pdf | $B_{t,b}$ |
|------------|--|---|
| Gaussian | $\frac{1}{\sqrt{2\pi}\sigma} \exp\left[-\frac{(i - \langle i \rangle)^2}{2\sigma^2}\right]$ | $\frac{1}{4} \frac{(\langle i_t \rangle - \langle i_b \rangle)^2}{\sigma_t^2 + \sigma_b^2} + \frac{1}{2} \ln \left[\frac{1}{2} \left(\sqrt{\frac{\sigma_t^2}{\sigma_b^2} + \sqrt{\frac{\sigma_b^2}{\sigma_t^2}}} \right) \right]$ |
| Poisson | $\sum_{n=N} \delta(i - n) \exp(-\langle i \rangle) \frac{\langle i \rangle^n}{n!}$ | $\frac{1}{2} (\sqrt{\langle i_t \rangle} - \sqrt{\langle i_b \rangle})^2$ |
| Gamma | $\left(\frac{L}{\langle i \rangle}\right)^L \frac{i^{L-1}}{\Gamma(L)} \exp\left[-\frac{L}{\langle i \rangle} i\right]$ | $L \ln \left[\frac{1}{2} \left(\sqrt{\frac{\langle i_t \rangle}{\langle i_b \rangle}} + \sqrt{\frac{\langle i_b \rangle}{\langle i_t \rangle}} \right) \right]$ |

Table 2.1: Common statistical distributions, their probability distribution functions (pdf) and corresponding Bhattacharya distance ($B_{c,f}$). i denotes pixel intensity in the image. $\delta(i)$, N , L and σ represents the Dirac distribution, set of integers, order of Gamma statistics and standard deviation respectively.

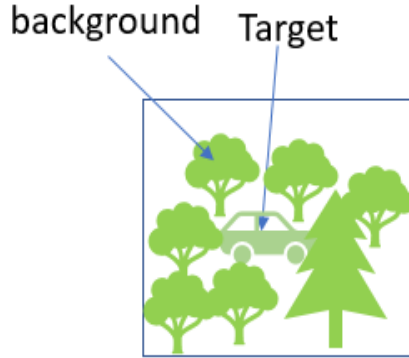


Figure 2.3: Example of scene of interest for target detection applications.

An example to illustrate Bhattacharya distance as seperability criterion

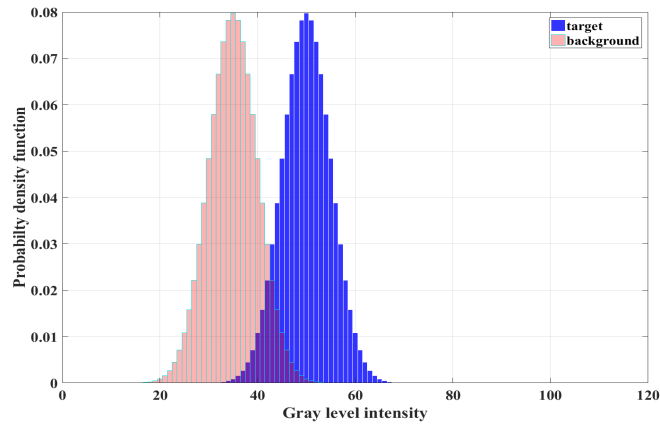
Let us consider the hypothetical scene shown in figure 2.3. The object of our interest in the image is the car painted in green colour. The car is concealed inside woods but a careful observer may detect its presence. This type of scenes are observed in such areas as remote sensing, machine vision, or biomedical imaging. The detection of objects/features in such cases can be challenging due to following reasons: (a) target is not very distinct from background due to its physical properties (b) imaging scenarios are difficult (eg: imaging through turbulence and fog) (c) targets are moving.

The objective is to determine the presence of target in the region of image we choose to analyze. This is an example of binary hypothesis problem that can be solved by the theory of detection. Let us formally define the detection problem as follows. Let H_0 represent the hypothesis in which only background is present and H_1 represent the hypothesis in which the target is present. Since pixel information is the data, we determine the conditional probability density function (pdf) of pixels where we expect the presence of target and background in the image. For simplicity, let us assume that only detector noise is present in the imaging system which can be represented by additive Gaussian noise model. Therefore, we assume that the intensity variance of target and background regions is the same and denoted and denoted σ^2 . Let $\langle i_t \rangle$ and $\langle i_b \rangle$ represent the average intensity of target and background respectively. Then the pdfs of target and background, $p(i|H_1)$ and $p(i|H_0)$ are defined as

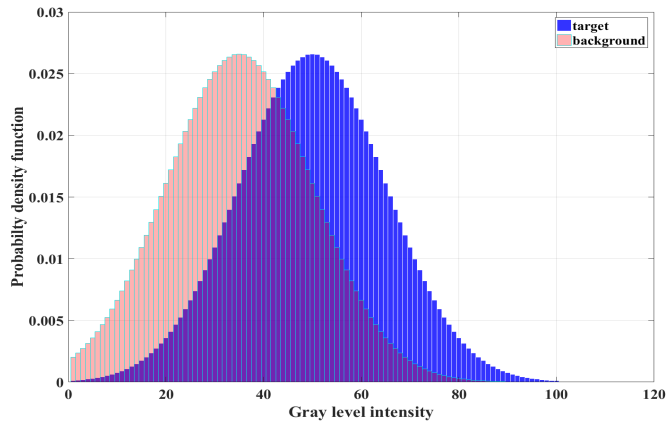
$$\begin{aligned}
 p(i|H_0) &= \frac{1}{\sqrt{2\pi\sigma^2}} \exp\left(-\frac{1}{2\sigma^2}(i - \langle i_b \rangle)^2\right) \\
 p(i|H_1) &= \frac{1}{\sqrt{2\pi\sigma^2}} \exp\left(-\frac{1}{2\sigma^2}(i - \langle i_t \rangle)^2\right).
 \end{aligned}
 \tag{2.5}$$

Let us consider the two following practical examples:

- case A: $\langle i_t \rangle = 50$, $\langle i_b \rangle = 35$, $\sigma^2 = 5$
- case B: $\langle i_t \rangle = 50$, $\langle i_b \rangle = 35$, $\sigma^2 = 15$



(a)



(b)

Figure 2.4: Probability density functions of target ($p(i|H_1)$, blue in colour) and background ($p(i|H_0)$, red in colour) are plotted side by side (a) Case A: $i_t = 50$, $i_b = 35$, $\sigma^2 = 5$ (b) Case B: $i_t = 50$, $i_b = 35$, $\sigma^2 = 15$.

Figure 2.4 shows the histogram of pdfs of these two cases to compare. The only difference between them is the variance values.

Case A in the figure 2.4 shows good separation of the two pdf but case B shows the absence of good separation between them. Case B is least preferred scenario in the detection problem because the error probability would be high due to large overlap of pdfs. The only difference in statistical parameters between case A and case B is variance values. If we calculate $B_{t,b}$ in case A and case B, the values are found out as 22.5 and 7.5 respectively. Therefore, one can conclude that the difference between average intensities of target and background as well as low intensity variance plays a very important role in increasing separability/detection capability and thus reducing the likelihood of errors.

2.2 Design of an active adaptive polarimetric imager for contrast optimization

While conventional imaging systems utilize intensity of light scattered from a scene to detect the presence of objects, polarimetric imaging systems analyze information contained in the polarization state of light coming from the scene. As discussed in the previous chapter, there are passive and active polarimetric imagers. The function of passive polarimetric imagers is to analyze the polarized state of light scattered from the scene and this configuration is widely used in reconstruction of 3D objects, remote sensing etc [30, 31, 2]. On the other hand, active polarimetric imagers illuminate the scene with polarized light and analyze the polarized light scattered from the scene. Though they have complex architecture compared to passive polarimetric imagers, they are preferred for applications such as biomedical applications and industrial inspection [32, 33]. The suitable candidate for contrast optimization is an active polarimetric imager since it offers more degrees of freedom to manipulate. In this section, we discuss about the principle and the design of an active adaptive polarimetric imager, general methods of generation and analysis of polarization states and introduction of phase delay by liquid crystal variable retarders.

2.2.1 Principle of active polarimetric imaging

Figure 2.5 shows a scheme of active polarimetric imaging configuration. The scene in the figure contains three blocks of rough material (translucent scotch tape glued on sand paper made up of large grains) sticked carefully on a smooth material (small grained sand paper). Both are painted in same colour so that they are not recognizable from each other for naked eye/standard imaging system. The objective of active polarimetric imaging system is to discriminate those three blocks of rough material (target) from smooth background. Since the target and background consist of different materials, they have different polarimetric properties. Therefore, we represent the polarization properties of target and background by \mathbf{M}_t and \mathbf{M}_b respectively. A coherent/incoherent light source can be used. If we use incoherent light source such as white light (halogen lamp), a spectral filter must be used in order to measure polarization of light accurately.

The unpolarized light from the source passes through PSG, which in turn transforms unpolarized light into fully polarized light. The polarized state of light generated by PSG is represented as \mathbf{S} with intensity $I_0\mathbf{S}$. The polarized light illuminates the scene. The objects in the scene interact with incident light and change its state of polarization differently due to their unique physical properties. This interaction can be represented as $\mathbf{M}_\bullet\mathbf{S}$, where \mathbf{M} indicates Mueller matrix and $\bullet = \{t,b\}$, the subscripts referring to the target or the background. The polarized light scattered from the scene is projected by polarization state analyzer (PSA) on an eigenstate represented as \mathbf{T} before going through spectral filter to CCD camera. The intensity of light reaching each pixel of the camera is represented as

$$I_\bullet \propto \frac{I_0}{2} \mathbf{T}^T \mathbf{M}_\bullet \mathbf{S}. \quad (2.6)$$

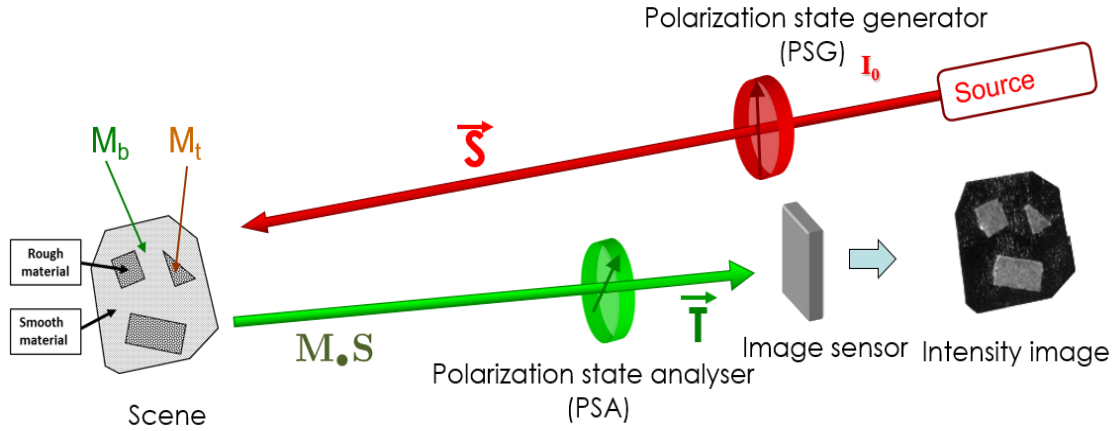


Figure 2.5: A scheme of active polarimetric imaging in reflection configuration.

Thus we get an image with spatially varying intensities which in turn depends upon the state of the PSG and the PSA.

2.2.2 Generation and analysis of polarization states of light

Generation and analysis of polarization states of light are primary tasks in active polarimetric imaging. Therefore, the complexity of PSG/PSA configuration, the accuracy of polarization state generation/analysis and the speed of implementation are important factors to consider while choosing the type of optical configuration. Based on different studies published [34, 35], in the following part, we discuss about different models of PSG/PSA configuration.

Model I : Polarizer and a rotating phase plate

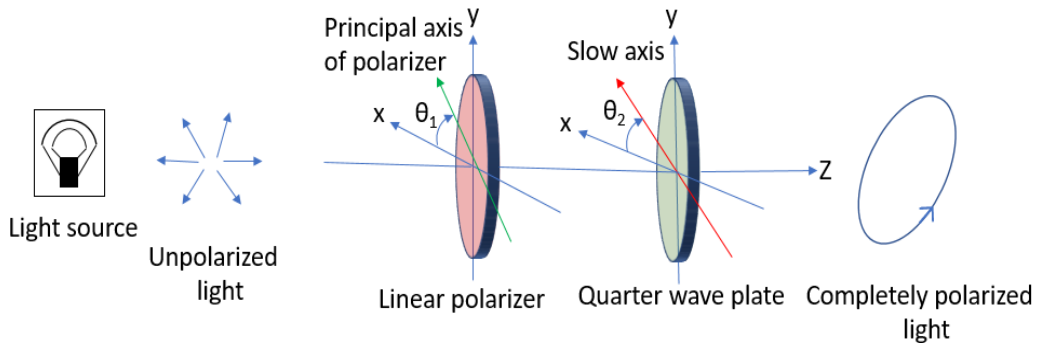


Figure 2.6: Polarizer and rotating phase plate configuration. The polarizer and quarter waveplate is oriented at angle θ_1 and θ_2 respectively with reference to x - axis.

This configuration consists of a linear polarizer and a quarter wave plate which can be rotated mechanically (manually/motor assisted) by the user (see figure 2.6). The polarizer principal axis is kept at angle

θ_1 from x-axis followed by a quarter wave plate whose slow axis is oriented at angle θ_2 . The polarization state of light generated by such a configuration can be mathematically represented as:

$$\begin{aligned} \mathbf{S} &= \mathbf{M}_{wp}(\theta_2, \pi/4)\mathbf{M}_p(\theta_1)\mathbf{S}_{in} \\ &= \begin{bmatrix} 1 \\ \cos 2(\theta_2 - \theta_1) \cos 2\theta_2 \\ \cos 2(\theta_2 - \theta_1) \sin 2\theta_2 \\ \sin 2(\theta_2 - \theta_1) \end{bmatrix}, \end{aligned} \quad (2.7)$$

where \mathbf{S}_{in} , $M_{wp}(\theta_2, \pi/4)$ and $M_p(\theta_1)$ represent the Stokes vector of input light which is unpolarized, Mueller matrices of quarter wave plate and linear polarizer oriented at angle θ_2 and θ_1 respectively. This configuration offers good precision in generation of polarization states. This configuration which requires rotation of optical elements with stepper motors can generate any polarization states of light on Poincaré sphere. However, motor assisted rotation can be a source of problems due to limitation of precise rotation steps and it requires regular recalibration.

Model II : Fixed polarizer and rotating variable phase plate

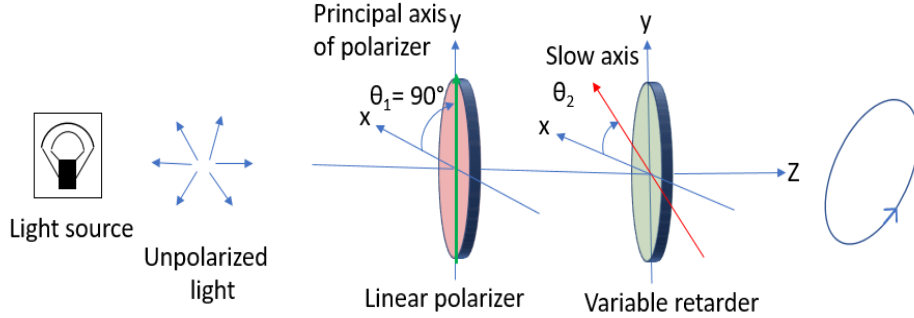


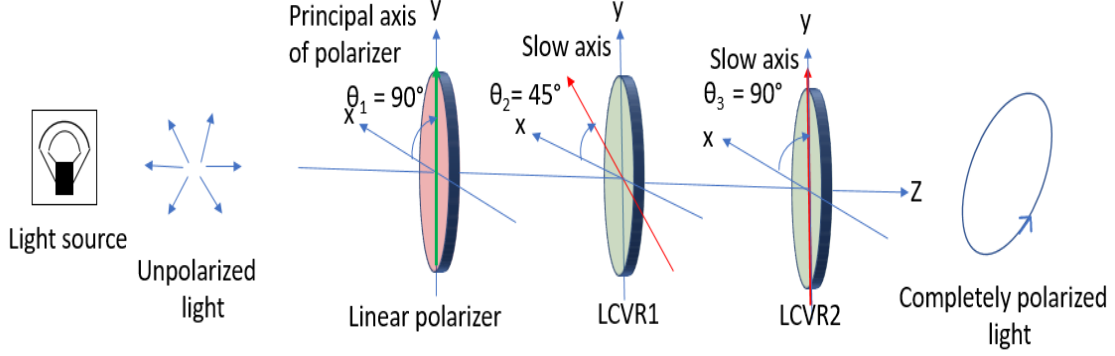
Figure 2.7: Fixed polarizer and rotating variable phase plate.

A second configuration for generating polarization states on Poincaré sphere is shown in figure 2.7. It consists of a linear polarizer whose principal axis is oriented at 90° followed by a variable phase plate whose slow axis is oriented at angle θ_2 with respect to x - axis. The variable retarder can introduce phase delay ϕ from 0 to 2π continuously and it is precise. The variable retarder which works on principle of liquid crystal technology is quick in producing phase delay but sensitive to temperature variations. The Stokes vector produced by such a configuration for unpolarized input light (\mathbf{S}_{in}) is given as

$$\begin{aligned} \mathbf{S} &= \mathbf{M}_{wp}(\theta_2, \phi)\mathbf{M}_p(\theta_1 = 90^\circ)\mathbf{S}_{in} \\ &= \begin{bmatrix} 1 \\ -(\cos^2 2\theta_2 + \cos \phi \sin^2 2\theta_2) \\ (\cos \phi - 1) \cos 2\theta_2 \sin 2\theta_2 \\ -\sin 2\theta_2 \sin \phi \end{bmatrix}, \end{aligned} \quad (2.8)$$

where $\mathbf{M}_{wp}(\theta_2, \phi)$, $\mathbf{M}_p(\theta_1 = 90^\circ)$ are Mueller matrices of the waveplate and the linear polarizer respectively. To describe the polarization state defined on the Poincaré sphere, the LCVR has to be rotated manually or with the help of carefully calibrated stepper motor.

Model III : Fixed polarizer and two variable phase plates



Another configuration of polarization state generator consists of a linear polarizer whose principal axis is oriented at 90° followed by two LCVRs whose slow axes are oriented at 45° and 90° with x - axis. This design is known for its quickness in generating any polarization state on Poincaré sphere and lack of any mechanical moving parts. The Stokes vector generated by such a configuration is computed as:

$$\begin{aligned} \mathbf{S} &= \mathbf{M}_{wp1}(\theta_3, \phi_2)\mathbf{M}_{wp2}(\theta_2, \phi_1)\mathbf{M}_p(\theta_1 = 90^\circ)\mathbf{S}_{in} \\ &= \begin{pmatrix} 1 \\ -\cos \phi_1 \\ \sin \phi_1 \sin \phi_2 \\ -\sin \phi_1 \cos \phi_2 \end{pmatrix}. \end{aligned} \quad (2.9)$$

The alignment of the configuration has to be very accurate in order to get polarization states close to ideal values.

| Configuration | Rotating polarizer, rotating quarter wave plate | Fixed polarizer, rotating variable retarder | Fixed polarizer, two variable retarders |
|---------------|---|---|---|
| Speed | - - | - | ++ |
| Precision | + | + | + |
| Moving parts | - - | + | ++ |

Table 2.2: A comparison of different types of optical configurations feasible to generate and analyze polarization states are displayed. Three important features of them are put into comparison and their grades are in ascending order of interest from - - to ++.

A comparison of different configurations described in this section is given in table 2.2. The Model III has been chosen to construct PSG and PSA of the adaptive active polarimetric imager due to its speed, precision and lack of any mechanically moving parts.

2.2.3 Introduction of phase delay by liquid crystal variable retarder (LCVR)

We have discussed very briefly about the role of liquid crystal variable retarder in generation and analysis of polarization states in previous sections. Therefore, we present here a general information about LCVR and how it introduces phase delay into the incoming optical beam.

LCVR is a versatile component in polarization optics. It is used to generate different polarization states of light in combination with linear polarizer in polarimetric imaging application. Liquid crystals are matter in a state which exhibits properties between those of conventional liquid and solid crystal [36]. They show physical properties (optical, electrical, elastic, etc.) that are dependent on the orientation of molecules relative to a fixed axis in the material, making them unique in their properties. Elongated, moderate size organic molecules tend to form liquid crystals that orient on their long axis but we do observe disc-like and banana shaped molecules of liquid crystals also. Optical variable retarders made up of nematic liquid crystals are used in our laboratory (Meadowlark Optics) and thus we will focus on literature of this type of LCVR here. This type of retarders became popular in comparison to crystal retarders (made up of birefringent crystals like quartz) because it offers advantages like low price, true zero order capability for enhanced acceptance angle and possibility to produce large apertures [37].

The important components used in the construction of LCVR are fused silica, indium tin oxide (ITO), thin dielectric layer and nematic liquid crystals. Two optically flat fused silica windows are coated with indium tin oxide which are optically transparent and electrically conductive. A thin layer of dielectric material is applied over the ITO carefully, which acts as molecular alignment layer. Two windows are carefully aligned but keeping a space of few microns apart. This cavity is filled with nematic liquid crystal material. Electrical contacts are attached and device is sealed from environment fluctuations.

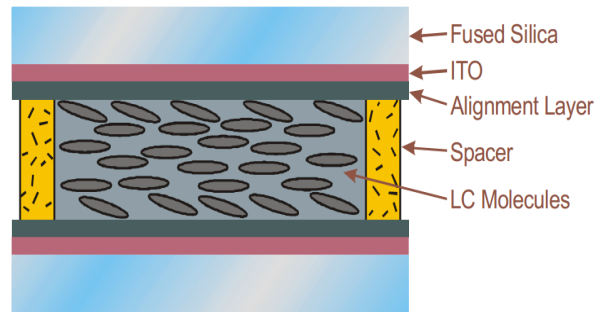


Figure 2.8: Liquid crystal variable retarder construction showing molecular alignment (courtesy : Meadowlark Optics). The schematic diagram shows the state of alignment when voltage applied is zero ($v = 0$, maximum retardance).

Anisotropic nematic liquid crystal molecules in the cell act as uniaxial birefringent layers. The molecules inside cell are aligned with their long axes parallel, but with their centres randomly distributed. In the absence of external voltage, the liquid crystal molecules lie parallel to the glass substrates and maximum retardation is achieved (see figure 2.8). When voltage is applied, liquid crystal molecules change their orientation in perpendicular to fused silica windows, which results in reduction in the effective birefringence and hence low retardance (see figure 2.9). But molecules at the surface have less degree of freedom to rotate because they are pinned at the alignment layer. This can create residual resistance up to 30 nm even at high voltage (20 volts). This problem can be solved by fixing a subtractive retarder polymer known as compensator attached to the liquid crystal. The phase shift introduced to the path of incoming

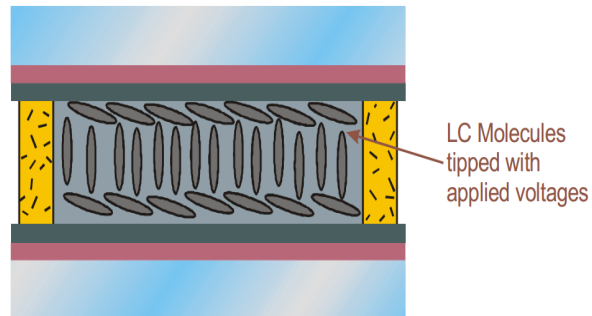


Figure 2.9: Liquid crystal variable retarder construction showing molecular alignment (courtesy : Meadowlark Optics). The schematic diagram shows the state of alignment when voltage applied is above zero ($v \gg 0$, minimum retardance).

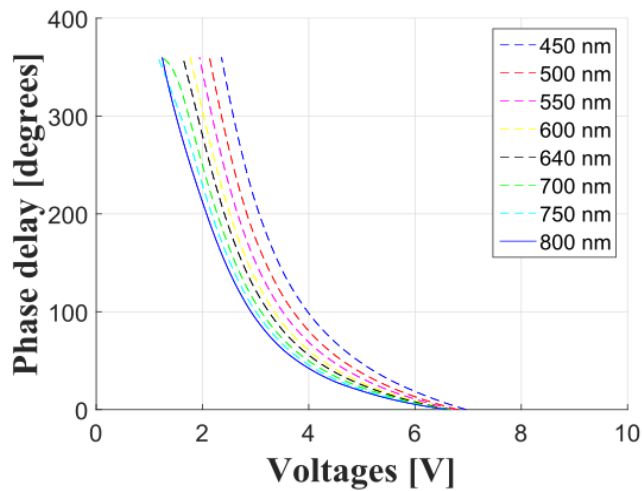


Figure 2.10: Liquid crystal variable retarder response curve: phase delay as function of voltages at 30°C for different wavelengths (measured using a spectro ellipsometer at LPICM, Ecole polytechnique, Palaiseau)

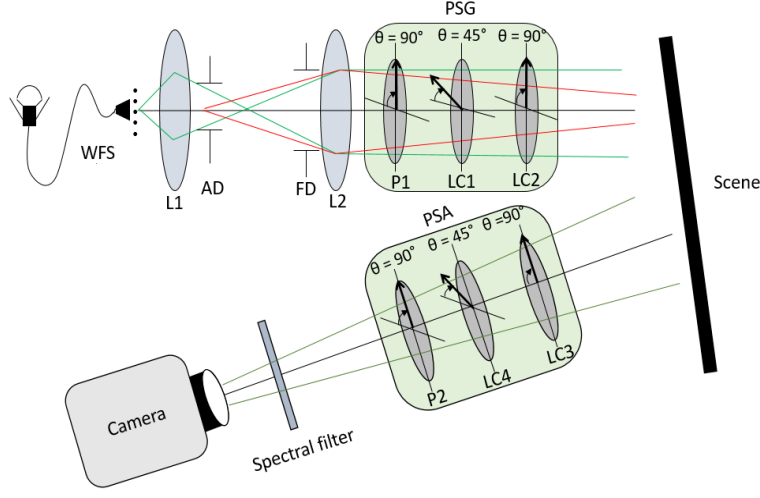


Figure 2.11: Design of optical set up for contrast optimization. WFS - white light fiber source, L1, L2 - lenses, AD, FD - aperture and field diaphragms, P1, P2 - linear polarizers, LC1, LC2, LC3, LC4 - liquid crystal variable retarders

light by LCVR is dependent on voltage, the ordinary and extra ordinary refractive indices of liquid crystal, the wavelength of incident light and the thickness of cell. This can be expressed in the equation below:

$$\phi(v) = \frac{2\pi}{\lambda} [n(V) - n_o]e \quad (2.10)$$

where λ is the wavelength of incident light, n_e and n_o are the extraordinary and ordinary refractive indices, n is the voltage dependent variable refractive index whose minimum value is n_o and maximum is n_e and e is the thickness of cell.

As voltage increases, $(n_e(v) - n_o) \rightarrow 0$, figure 2.10 shows the exact relation between retardance and voltage of LCVR (Meadowlark Optics) used in our lab. The LCVR in our laboratory is ideally intended for use in $\lambda = 640\text{nm}$. In order to use it for multispectral applications, we measured voltage-phase delay curves for different wavelengths using a spectro - ellipsometer. LCVRs are very sensitive to temperature fluctuations and therefore have to be kept inside controlled temperature environment.

2.2.4 Design of active adaptive polarimetric imager for contrast optimization in narrow spectral band

Figure 2.11 shows the design of the active adaptive polarimetric imager we used for contrast optimization. We have used a white - light fiber source, with Köhler illumination to homogenize the light, polarization state generator (PSG)/polarization state analyzer (PSA) which consists of a fixed linear polarizer followed by two nematic liquid crystal retarders, spectral filter and a CCD camera to build an active adaptive polarimetric imager.

The polarization properties of the scene as well as optical elements of PSG/PSA are wavelength dependent. Therefore Stokes vectors with unit intensity, generated/analyzed by PSG/PSA can be written as

$$\mathbf{S} = \begin{bmatrix} 1 \\ \mathbf{s}_{\theta_1}(\lambda) \end{bmatrix}, \mathbf{T} = \begin{bmatrix} 1 \\ \mathbf{t}_{\theta_2}(\lambda) \end{bmatrix} \quad (2.11)$$

where \mathbf{s}_{θ_1} and \mathbf{t}_{θ_2} represents the 3-dimensional, unit-norm reduced Stokes vectors of PSG and PSA respectively. In the expression \mathbf{s}_{θ_1} and \mathbf{t}_{θ_2} , $\{\theta_1, \theta_2\}$ represents the set of voltages which control liquid crystal variable retarders in the set-up. The chosen configuration of PSG/PSA is a classical model used in polarization state generation and analysis [35, 14]. It is described in section 2.2.2 (Model III). The PSG and PSA consist of a fixed linear polarizer oriented at 90° followed by two nematic liquid crystal retarders (Meadowlark Optics) oriented at 45° and 90° respectively with respect to reference axis. The advantage of using this configuration is that it can generate or analyze any polarization state defined on the Poincaré sphere. The polarized light generated/analyzed by such a configuration can be represented as

$$\mathbf{s}_{\theta_1}(\lambda) = \begin{bmatrix} -\cos(\phi_1^\lambda) \\ \sin(\phi_1^\lambda) \sin(\phi_2^\lambda) \\ -\sin(\phi_1^\lambda) \cos(\phi_2^\lambda) \end{bmatrix}, \mathbf{t}_{\theta_2}(\lambda) = \begin{bmatrix} -\cos(\phi_4^\lambda) \\ -\sin(\phi_4^\lambda) \sin(\phi_3^\lambda) \\ -\sin(\phi_4^\lambda) \cos(\phi_3^\lambda) \end{bmatrix}, \quad (2.12)$$

where ϕ_i^λ is the phase delay induced by the i^{th} LCVR of PSG-PSA configuration. The superscript λ indicates that the parameters depend on wavelength. The phase induced by i^{th} LCVR is represented as $\phi_i^\lambda(v) = \frac{2\pi}{\lambda}[n(V_i) - n_0]e$, where λ is the wavelength of light, V_i is the voltage applied to i^{th} LCVR, n_0 and n_e are the ordinary and extraordinary refractive indices, n is the voltage dependent variable refractive index whose minimum value is n_o and maximum value is n_e , and e is the thickness of cell. Then, we define $\theta_1 = (V_1, V_2)$ and $\theta_2 = (V_3, V_4)$ as the voltages applied to LCVRs in PSG and PSA respectively.

Similarly, we can parametrize the Mueller matrix as shown below :

$$\mathbf{M}_\bullet = \begin{bmatrix} \mathbf{M}_{0,\bullet}(\lambda) & \mathbf{m}_\bullet^T(\lambda) \\ \mathbf{n}_\bullet(\lambda) & \tilde{\mathbf{M}}_\bullet(\lambda) \end{bmatrix} \quad (2.13)$$

where $\mathbf{M}_{0,\bullet}(\lambda)$ denotes first element of Mueller matrix, $\mathbf{m}(\lambda)$ and $\mathbf{n}(\lambda)$ stands for 3 dimensional unit-norm vectors, $\tilde{\mathbf{M}}$ is 3×3 matrix and superscript T stands for matrix transposition.

The light which gets backscattered from the scene passes through PSA and spectral filter, and finally reaches the CCD camera. The intensity of light detected at each pixel of the detector can be represented as

$$i_\bullet = \frac{\tau\eta(\lambda)I_0(\lambda)}{2} \mathbf{T}^T \mathbf{M}_\bullet \mathbf{S} + \nu, \quad (2.14)$$

where τ is the exposure time of sensor, $\eta(\lambda)$ is the quantum efficiency of detector, $I_0(\lambda)$ is the light source intensity and ν is an additive Gaussian noise of zero mean and variance σ^2 . We assume that noise characteristics are the same in all regions in the scene, and are independent of the wavelength and exposure time. Now the statistical average of intensity of target and background can be expressed as

$$\begin{aligned} \langle i_t \rangle &= \frac{\tau\rho(\lambda)}{2} \mathbf{T}^T \mathbf{M}_t \mathbf{S} \\ \langle i_b \rangle &= \frac{\tau\rho(\lambda)}{2} \mathbf{T}^T \mathbf{M}_b \mathbf{S} \end{aligned} \quad (2.15)$$

where $\rho(\lambda) = \eta(\lambda)I_0(\lambda)$. As discussed in section 2.1.3, we choose Bhattacharya distance as a suitable criterion to define contrast between target and background, and for an additive Gaussian noise model, it is expressed as (see table 2.1)

$$C = \frac{1}{8\sigma^2} (\langle i_t \rangle - \langle i_b \rangle)^2. \quad (2.16)$$

The equation 2.16 can be rewritten using equations 2.15 and 2.13 as

$$C_\lambda(\theta_1, \theta_2) = \frac{\tau^2}{32\sigma^2} \rho^2(\lambda) \left[\Delta M_0(\lambda) + \Delta \mathbf{m}^T(\lambda) \mathbf{s}_{\theta_1}(\lambda) + \mathbf{t}_{\theta_2}^T(\lambda) (\Delta \mathbf{n}(\lambda) + \mathbf{D}(\lambda) \mathbf{s}_{\theta_1}(\lambda)) \right]^2, \quad (2.17)$$

where

$$\begin{aligned}\Delta M_0(\lambda) &= M_{0,t}(\lambda) - M_{0,b}(\lambda), \quad \Delta \mathbf{m}(\lambda) = \mathbf{m}_t(\lambda) - \mathbf{m}_b(\lambda) \\ \Delta \mathbf{n}(\lambda) &= \mathbf{n}_t(\lambda) - \mathbf{n}_b(\lambda), \quad \mathbf{D}(\lambda) = \tilde{\mathbf{M}}_t(\lambda) - \tilde{\mathbf{M}}_b(\lambda)\end{aligned}\tag{2.18}$$

In order to keep the above equation more readable, let us define

$$\begin{aligned}\chi_{\theta_1}(\lambda) &= \Delta M_0(\lambda) + \Delta \mathbf{m}^T(\lambda) \mathbf{s}_{\theta_1}(\lambda) \\ \mathbf{u}_{\theta_1}(\lambda) &= \Delta \mathbf{n}(\lambda) + \mathbf{D}(\lambda) \mathbf{s}_{\theta_1}(\lambda)\end{aligned}\tag{2.19}$$

then the equation for contrast is rewritten as

$$C_\lambda(\theta_1, \theta_2) = \frac{\tau^2}{32\sigma^2} \rho^2(\lambda) \left[\chi_{\theta_1}(\lambda) + \mathbf{t}_{\theta_2}^T(\lambda) \mathbf{u}_{\theta_1}(\lambda) \right]^2.\tag{2.20}$$

If we assume that there is a spectral filter centered at λ in our system, then it is possible to show that for a given set of parameters θ_1 , the maximum value of contrast as defined in equation 2.20 is achieved for $\theta_{2,opt}^\lambda$ chosen such that

$$\mathbf{t}_{\theta_{2,opt}^\lambda}(\lambda) = \text{sign} \left[\chi_{\theta_1}(\lambda) \right] \frac{\mathbf{u}_{\theta_1}(\lambda)}{\|\mathbf{u}_{\theta_1}(\lambda)\|}\tag{2.21}$$

where $\text{sign}(x) = -1$ if $x < 0$ and 1 otherwise, and the superscript $^\lambda$ tells us that the optimal configuration is only valid for this specific wavelength. The configuration that leads to the optimal contrast is then $(\theta_{1,opt}^\lambda, \theta_{2,opt}^\lambda)$ where

$$\theta_{1,opt}^\lambda = \underset{\theta_1}{\text{argmax}} [C_\lambda(\theta_1, \theta_{2,opt}^\lambda)]\tag{2.22}$$

We can observe here that the optimization has to be done only on the parameter θ_1 .

2.3 Conclusion

We have briefly discussed the theory of detection and the choice of the Bhattacharya distance to define the contrast between a target and the background. It is concluded that the optimal separation of probability distributions between target and background is necessary to keep error probability minimal. The definition of contrast expression changes with noise model we choose to work with. We have also explained the design and principle of active adaptive polarimetric imagers for contrast optimization in narrow spectral band, different methods to generate and analyze polarization states of light and the working principle of liquid crystal based variable retarders.

Chapter 3

Active adaptive polarimetric imager for contrast optimization in broadband polarimetric imaging

We have seen in the last chapter that the polarization properties of optical elements and Mueller matrix of objects are wavelength dependent. The optical elements in the polarimetric imaging system of our laboratory are not achromatic. Their characteristics and performance are optimal in the wavelength range determined by their manufacturer. For example, the LCVRs in PSG/PSA of our imaging system are ideally designed for use at $\lambda = 640$ nm. The voltage-phase delay relation provided by the manufacturer is valid only at $\lambda = 640$ nm. Therefore use of LCVR at any other wavelength without the knowledge of corresponding voltage-phase delay relation creates error in generation/detection of polarization states. In the experimental set up, we have used white light source to illuminate the sample. In order to have an accurate polarization generation and detection, it is thus necessary to insert a narrowband spectral filter centered around $\lambda = 640$ nm in the imaging set-up. Now, if we try to use the experimental set-up for high speed imaging applications, *i.e.* with low camera integration time, we observe that the images recorded have poor contrast. This is because the spectral filter blocks unwanted signals from entering the detector and thus large number of photons too.

Increasing the intensity of the light source can compensate the photon lost by filtering but this is not an optimal solution in photon starved imaging conditions. Placing achromatic optical components in the system is another option but this is often expensive thing to do. A good solution to this problem is to remove the spectral filter from the imaging set up and thus allow a larger number of photons to enter the detector. Removal of spectral filter allows us to record images with high signal to noise ratio at low integration time. We call this type of polarimetric imaging system a broadband polarimetric imaging system.

In this chapter, we derive an expression for the contrast in broadband polarimetric imaging. Then we illustrate the impact of spectral broadening on contrast enhancement, first by numerical study and then by experimental results conducted on a scene made in laboratory. We also discuss our perspectives about this work at the end of chapter.

3.1 Theoretical framework

We know from Section 2.2.4 that the contrast expression defined for an active adaptive polarimetric imaging in narrowband spectrum is

$$C_\lambda(\theta_1, \theta_2) = \frac{\tau^2}{32\sigma^2} \rho^2(\lambda) \left[\chi_{\theta_1}(\lambda) + \mathbf{t}_{\theta_2}^{\mathbf{T}}(\lambda) u_{\theta_1}(\lambda) \right]^2. \quad (3.1)$$

Let us extend the contrast expression for active adaptive broadband polarimetric imaging as shown below [38, 39] :

$$C_{\Delta\lambda}(\theta_1, \theta_2) = \frac{\tau^2}{32\sigma^2} \left(\int_{\Delta\lambda} \rho(\lambda) \left[\chi_{\theta_1}(\lambda) + \mathbf{t}_{\theta_2}^{\mathbf{T}}(\lambda) u_{\theta_1}(\lambda) \right] d\lambda \right)^2, \quad (3.2)$$

where $\Delta\lambda$ is the bandwidth of the system. Now we have images with better signal to noise ratio because there are more photons entering the detector. However the polarized light generated/detected are affected by "chromatic aberration" since chromatic optical elements are used with no spectral filter. This polarization mismatch decreases the contrast in the image but we show in following section that broadening the spectrum of light entering the system can increase the contrast between two regions of a scene. Furthermore, we demonstrate that this contrast can be further increased by taking into account the spectral dependence of the system and of the polarimetric properties of the scene in the optimization of the measurement procedure. That means that there exists configurations of PSG and PSA ($\theta_{1,opt}^{\Delta\lambda}, \theta_{2,opt}^{\Delta\lambda}$) for which the increase of light flux overcomes the polarimetric property mismatch of the system components caused by spectral broadening. They are defined as

$$(\theta_{1,opt}^{\Delta\lambda}, \theta_{2,opt}^{\Delta\lambda}) = \underset{\theta_1, \theta_2}{\operatorname{argmax}} [C_{\Delta\lambda}(\theta_1, \theta_2)]. \quad (3.3)$$

3.2 Numerical study

In this section, we illustrate the impact of spectral broadening on the value of the contrast between the target and the background through simulations involving ideal components for both the set-up and the scene of interest. Section 3.2.1 presents the model of the simulated scenarios, and Section 3.2.2 then presents the results obtained for different scenes.

3.2.1 Description of set-up used in the simulation

The simulation scenarios are based on an existing set-up described in [13]. The illumination part is made of a cold halogen white source of spectrum $I_0(\lambda)$ followed by a PSG composed of two liquid crystal variable retarders (LCVR) and one polarizer as described in the previous chapter. The light is then analyzed by a PSA fashioned in a similar way and the image is obtained using a quantum detector characterized by its quantum efficiency $\eta(\lambda)$.

The eigenstates of the PSG and PSA are given by equation (2.12). These eigenstates depend on the birefringence induced by the LCVR of the devices which is a function of the wavelength and of the control voltage V applied to the LCVR. Figure 3.1 gives the phase delay-voltage relation of LCVR used in our lab for eight different wavelengths. We also assume that the transmission of the LCVR does not change with the wavelength. For the study, we limit the working voltage range between 2.0 V and 8.0 V.

The spectral dependence of the camera $\eta(\lambda)$ and the source characteristics $I_0(\lambda)$ used in simulation are shown in figure 3.2. For simplicity, they are put together in to a single function $\rho(\lambda)$ as shown in equation (2.15). Figure 3.2 shows the evolution of the these three parameters with respect to the wavelength. $\eta(\lambda)$ (plain gray curve) is modeled from technical data of a Sony ICX414AL sensor, $I_0(\lambda)$ (dashed gray curve) is generated from an idealized spectrum of a xenon tungsten halogen lamp.

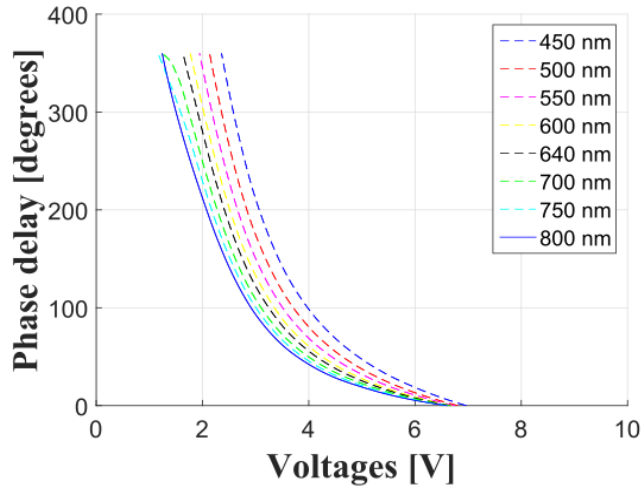


Figure 3.1: Liquid crystal variable retarder response curve : phase delay as function of voltages at 30°C for different wavelengths (measured using a spectro-ellipsometer at LPICM, Ecole polytechnique, Palaiseau)

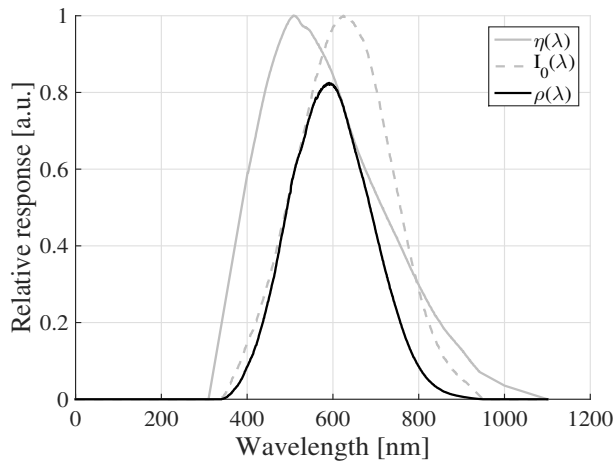


Figure 3.2: Spectral response of the camera ($\eta(\lambda)$ - gray plain curve) and spectrum of the source ($I_o(\lambda)$ - gray dashed curve), used in the simulations. The impact of both parameters is modeled by a single function $\rho(\lambda) = \eta(\lambda)I_0(\lambda)$ (black plain curve).

| Parameters | Scene 1 | Scene 2 |
|------------|------------------------|------------------------------|
| α_t | 135° | 135° |
| α_b | 150° | 150° |
| A_t | 90° × 550/360° | 90° × 550/360° |
| A_b | 300° × 550/360° | 300° × 550/360° |
| d_t | [0, 0, 0] ^T | [0, -0.75, 0] ^T |
| d_b | [0, 0, 0] ^T | [0.37, 0.65, 0] ^T |

Table 3.1: Parameters defining the two scenes considered in the simulations.

3.2.2 Contrast calculation

To study the impact of spectral broadening on the contrast, we consider two scenes where the target and background are composed of ideal retarders and diattenuators. Therefore their Mueller matrices can be represented as $\mathbf{M}_\bullet = \mathbf{R}(\phi_\bullet^\lambda, \alpha_\bullet)\mathbf{P}(\mathbf{d}_\bullet)$ where $\mathbf{R}(\phi_\bullet^\lambda, \alpha_\bullet)$ denotes the Mueller matrix of a retarder with an orientation α_\bullet and phase delay $\phi_\bullet^\lambda = 2\pi A_\bullet/\lambda$ with A_\bullet being a constant, and where $\mathbf{P}(\mathbf{d}_\bullet)$ is the Mueller matrix of a pure diattenuator with \mathbf{d}_\bullet being three-dimensional diattenuation vector of the considered region of the scene [20]. The diattenuation vector describes both the magnitude and the axis of diattenuation.

In case of *scene 1*, d_\bullet is a null vector and it is the same for both regions (target and background). For the *scene 2*, d_\bullet is not a null vector and it is different for both regions. More details of parameters used to construct Mueller matrix of the scenes for the contrast calculation are shown in table 3.1.

Contrast calculation of the scene with pure retarders

We consider in this section a scene composed of two pure retarders as target and background (*Scene 1*). First, let us consider a situation where a narrowband filter centered at 550 nm is used in the imaging system. In this case, using equations (2.21) and (2.22), one can find the configuration that optimizes the contrast. We see that the optimal contrast depends on (θ_1, θ_2) but for a given value of θ_1 , the optimal θ_2 can be calculated in closed form. Since for a given wavelength, there is a bijective relationship between the phase delay and the voltage in our working range, we represent the contrast as a 2-dimensional map of θ_1 *i.e.* (V_1, V_2) for $\lambda = 550$ nm. Figure 3.3 (b) shows the values of the contrast $C_\lambda(\theta_1, \theta_{2,\text{opt}}^\lambda)$ at $\lambda = 550$ nm. One can see that an infinite number of configurations lead to optimal contrast (bright yellow regions), as these configurations form a continuum on the contrast map. This phenomenon is due to the particular nature of the target and background and is explained in appendix A. We repeated contrast calculations for other wavelengths and results are displayed in figure 3.3. There was no single candidate $(\theta_{1,\text{opt}}^\lambda, \theta_{2,\text{opt}}^\lambda)$ which gave a distinct maximum in contrast calculation. However we picked one configuration which showed maximum contrast value, C_λ^{max} and it is shown in table 3.2. Figure 3.4 shows that the Stokes vectors of illumination and detection represented by red and blue dots on Poincaré sphere are different for different wavelengths.

Now, if we implement one of these configurations on the system and broaden the spectrum of the illumination, two antagonist effects will impact the value of the contrast. On the one hand, the increase of light flux on the detector will tend to improve the signal to noise ratio and thus contrast. Indeed, if the scene and the polarimetric response of the set-up components were independent of the wavelength, the contrast in equation (3.2) would be of the following form

$$C_{\Delta\lambda} = C_0 \times (\Delta\lambda)^2 \quad (3.4)$$

where $C_0 = \tau^2 \rho(\lambda_0) C_\lambda(\theta_{1,\text{opt}}^\lambda, \theta_{2,\text{opt}}^\lambda) / 4\sigma^2$ and λ_0 is the central wavelength of the narrowband filter. The contrast would thus vary as the square of the bandwidth, as represented in figure 3.5 (green line). On the

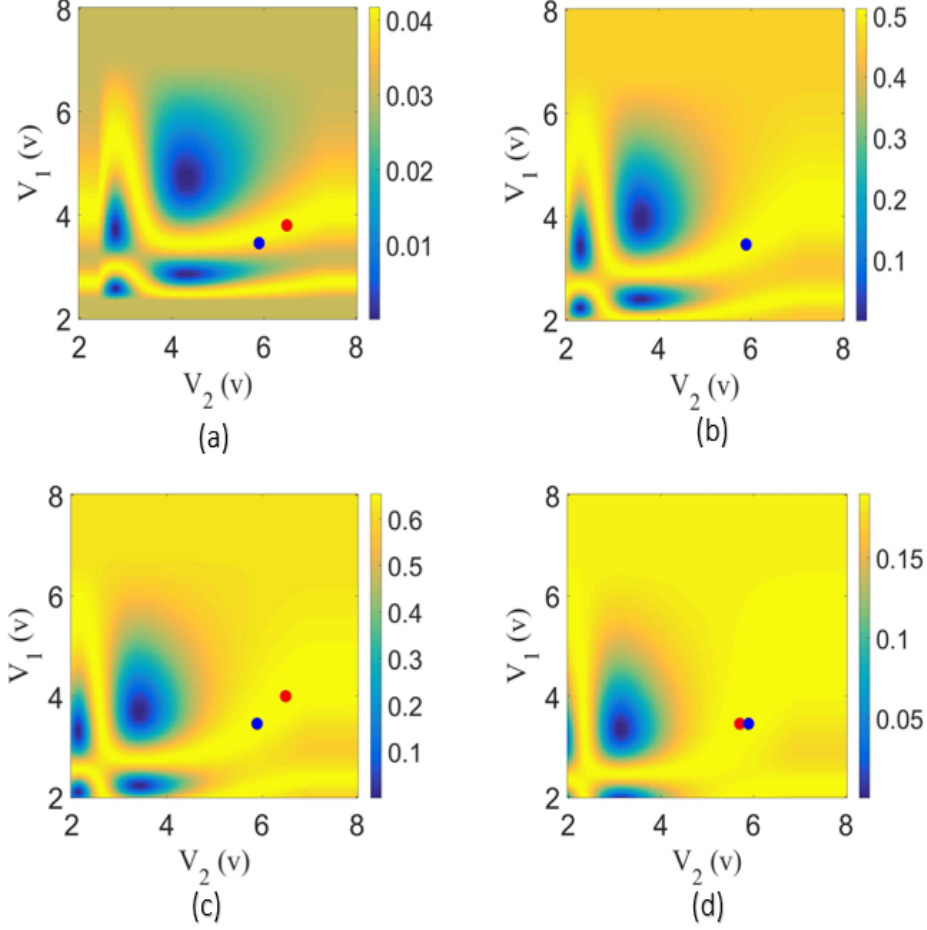


Figure 3.3: *Scene I - Pure retarders*: Contrast maps as a function of voltages (V_1, V_2) (a) 450 nm (b) 550 nm (c) 600 nm (d) 700 nm. The blue dot on all the contrast maps shows the coordinates $(\theta_{1,opt}^\lambda)$ of maximum contrast at $\lambda = 550$ nm. The red dot on the contrast maps in (a), (c) and (d) shows the coordinates $(\theta_{1,opt}^\lambda)$ of maximum contrast at their respective wavelengths.

| λ (nm) | C_λ^{max} | $(\theta_{1,opt}^\lambda, \theta_{2,opt}^\lambda)$ (V) | $\mathbf{s}_{\theta 1}$ | $\mathbf{t}_{\theta 2}$ |
|-------------------|-------------------|---|-------------------------|--------------------------|
| 450 | 0.04 | (3.80, 6.50, 2.55, 3.70) | $[0.4 \ 0.2 \ -0.9]^T$ | $[0.7 \ 0.4 \ -0.5]^T$ |
| 550 | 0.51 | (3.45, 5.90, 3.95, 6.00) | $[0.2 \ 0.2 \ -0.9]^T$ | $[-0.9 \ -0.3 \ -0.5]^T$ |
| 600 | 0.65 | (4.00, 6.50, 2.80, 5.45) | $[-0.4 \ 0.0 \ -0.9]^T$ | $[-0.9 \ -0.1 \ 0.4]^T$ |
| 700 | 0.18 | (3.45, 5.70, 4.65, 5.50) | $[-0.2 \ 0.2 \ -0.9]^T$ | $[-0.9 \ -0.2 \ -0.3]^T$ |

Table 3.2: *Scene I*: The Optimal voltages and reduced Stokes vectors associated with contrast optimization of scene 1 (pure retarders) at chosen wavelengths.

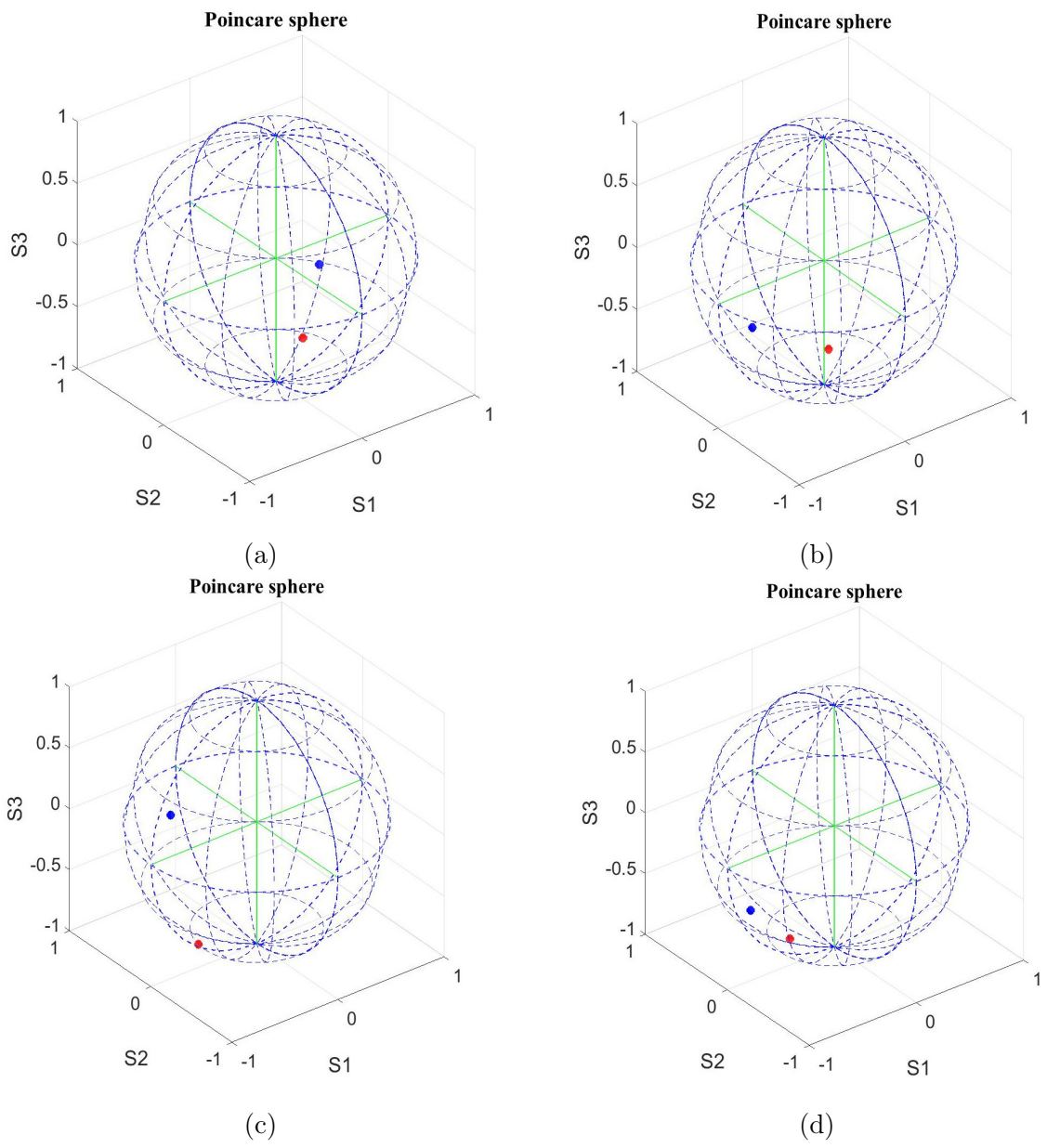


Figure 3.4: **Scene 1** :The optimal polarization states of illumination and detection for maximum contrast are marked on Poincaré sphere by red and blue dots respectively. They correspond to optimization at (a) 450 nm (b) 550 nm (c) 600 nm (d) 700 nm.

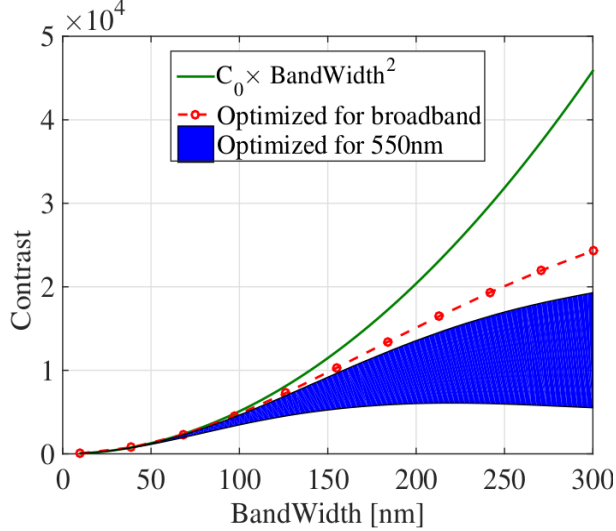


Figure 3.5: Contrast as a function of bandwidth of the system with $\tau^2/\sigma^2 = 1$ for scene 1.

other hand, due to the spectral dependence of the scene and of the components of the imaging system, the chosen configuration $(\theta_{1,\text{opt}}^\lambda, \theta_{2,\text{opt}}^\lambda)$ optimal for 550 nm is no longer optimal for the other wavelengths. For example, let us assume that we chose the configuration corresponding to the blue dot in figure 3.3(b). We can see that this configuration does not correspond to an optimum anymore for other three wavelengths. The red dot shows the optimal configuration we chose for those three wavelengths. This mismatch will lead to a contrast loss when the system integrates the signal over the complete bandwidth. This decrease can be more or less important depending on the configuration initially chosen inside the continuum. This phenomenon is shown in figure 3.5 where the blue area represents the values of the contrast defined by equation (3.2) as a function of the bandwidth, for all the possible configurations which are optimal at 550 nm. We can see that globally in this case, the increase of intensity overcomes the loss in polarimetric accuracy since the contrast increases with the bandwidth. However, for the worst case configurations, one can observe a loss of contrast as the bandwidth increases. This is due to the important mismatch between the properties of the set-up at the wavelength chosen for the initial optimization and the other wavelengths of the bandwidth.

Let us now optimize the configuration (θ_1, θ_2) in order to maximize the contrast of equation (3.2). To do so we perform an exhaustive search by calculating the contrast $C_{\Delta\lambda}$ for all values of the retardances induced by the LCVR. These values are generated using the voltage-retardance relationship illustrated in figure 3.1 by scanning the voltages applied to the LCVR that compose the PSG and the PSA with a resolution of 65 mV. For each value of the bandwidth we are then able to find a specific optimal set of voltages. The results appear in the red dashed curve of figure 3.5. We now observe a monotonous increase of the contrast, meaning that we are always able to find a configuration for which the loss of polarimetric accuracy is more than compensated by the increase of light flux.

Contrast calculation in the presence of diattenuation

We now consider a scene with diattenuation (*Scene 2*), and as before, we first consider the situation where a narrowband filter centered on 550 nm is used in the imaging system. Figure 3.6(b) shows the values of the contrast $C_\lambda(\theta_1, \theta_{2,\text{opt}}^\lambda)$ as a 2-dimensional function of (V_1, V_2) for $\lambda = 550$ nm. The impact of the presence of diattenuation on the scene can clearly be seen as the continuum observed in previous case

has now disappeared and only one global maximum remains (blue dot). Again we notice that the optimal configuration at $\lambda = 550$ nm is not optimal at other three wavelengths to achieve maximum contrast. The configuration corresponding to maxima at other three wavelengths are represented by red dot in the figure 3.6. Table 3.3 helps us to see this information clearly.

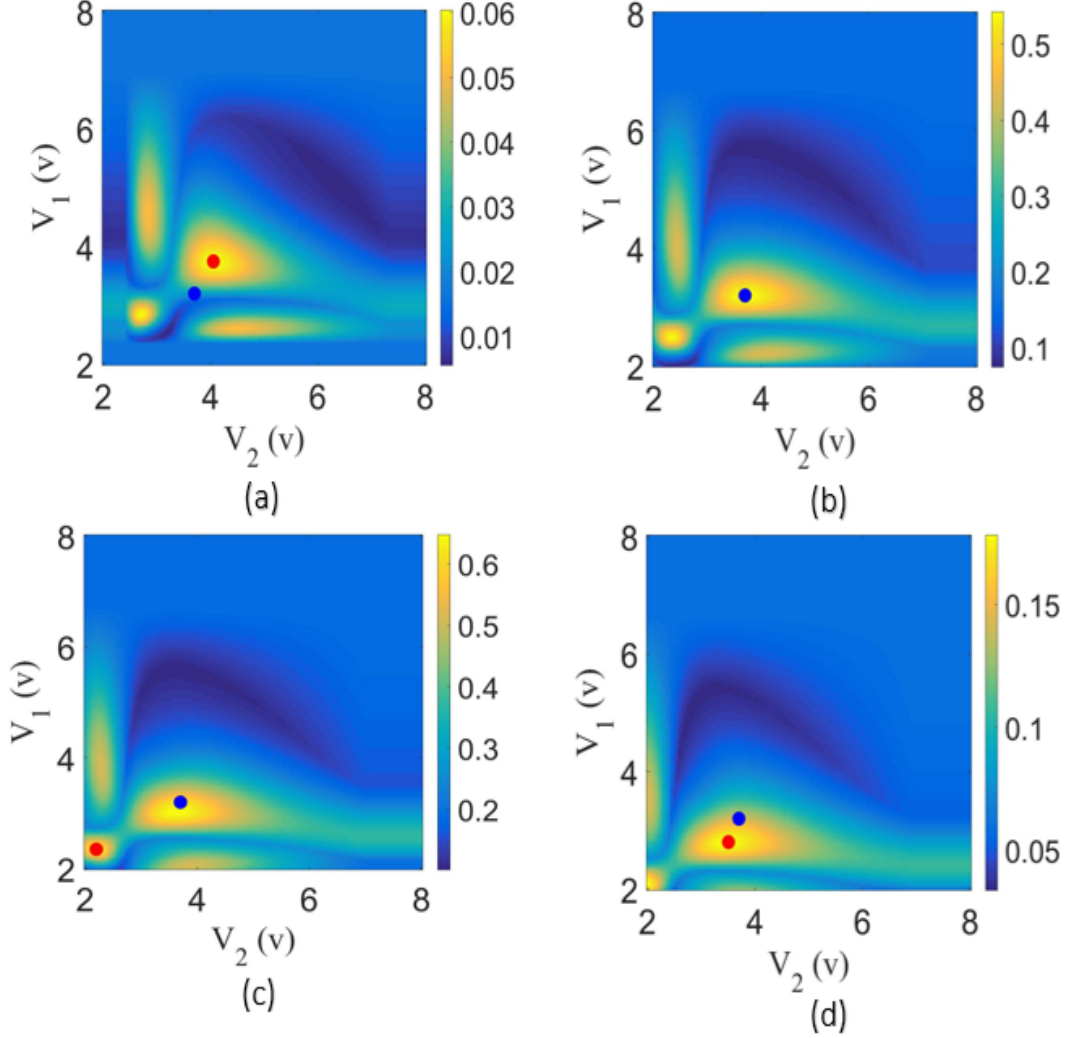


Figure 3.6: **Scene 2 - in presence of diattenuation** : Contrast maps as a function of voltages (V_1, V_2) (a) 450 nm (b) 550 nm (c) 600 nm (d) 700 nm. The blue dot on all the contrast maps shows the coordinates $(\theta_{1,opt}^\lambda)$ of maximum contrast at $\lambda = 550$ nm. The red dot on the contrast maps in (a), (c) and (d) shows the coordinates $(\theta_{1,opt}^\lambda)$ of maximum contrast at their respective wavelengths.

Figure 3.7 shows that the Stokes vectors of illumination and detection represented by red and blue dots on Poincaré sphere are different for different wavelengths in this case too.

Now if we implement on the set-up the configuration leading to this maximum and increase the spectral bandwidth, the two antagonist effects mentioned previously should still impact the value of the contrast. The evolution of the contrast as a function of the system bandwidth is displayed in figure 3.8. The green line represents the evolution of the contrast in the case where the scene and the system characteristics are independent of the wavelength and the blue curve represents the evolution of the contrast defined in

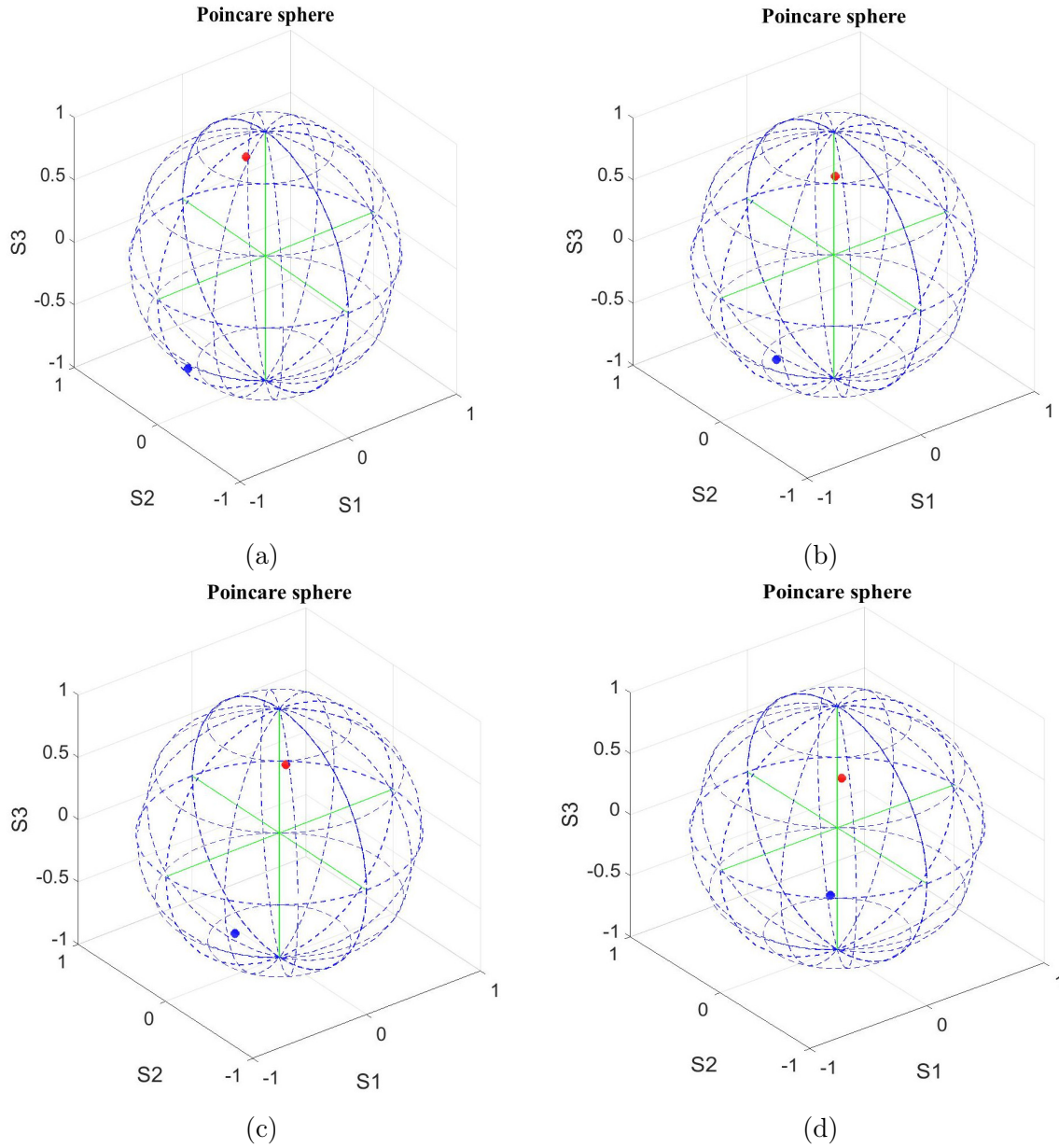


Figure 3.7: *Scene 2* : The optimal polarization states of illumination and detection for maximum contrast are marked on Poincaré sphere by red and blue dots respectively. They correspond to optimization at (a) 450 nm (b) 550 nm (c) 600 nm (d) 700 nm.

| λ (nm) | C_{λ}^{max} | $(\theta_{1,opt}^{\lambda}, \theta_{2,opt}^{\lambda})$ (V) | $\mathbf{s}_{\theta 1}$ | $\mathbf{t}_{\theta 2}$ |
|-------------------|---------------------|---|-------------------------|-------------------------|
| 450 | 0.06 | (3.75, 4.05, 2.45, 5.10) | $[0.5 \ 0.8 \ 0.2]^T$ | $[-0.5 \ 0.2 \ -0.8]^T$ |
| 550 | 0.54 | (3.20, 3.70, 2.05, 4.05) | $[0.6 \ 0.8 \ 0.0]^T$ | $[-0.2 \ 0.3 \ -0.9]^T$ |
| 600 | 0.64 | (2.35, 2.20, 2.85, 2.15) | $[0.6 \ 0.7 \ -0.0]^T$ | $[-0.1 \ 0.3 \ -0.9]^T$ |
| 700 | 0.17 | (2.80, 3.50, 2.65, 2.00) | $[0.6 \ 0.7 \ -0.1]^T$ | $[0.3 \ 0.4 \ -0.8]^T$ |

Table 3.3: **Scene 2** : The optimal voltages and reduced Stokes vectors associated with contrast optimization of scene 2 (retarders with attenuation) at wavelengths such as 450 nm, 550 nm, 600 nm and 700 nm.

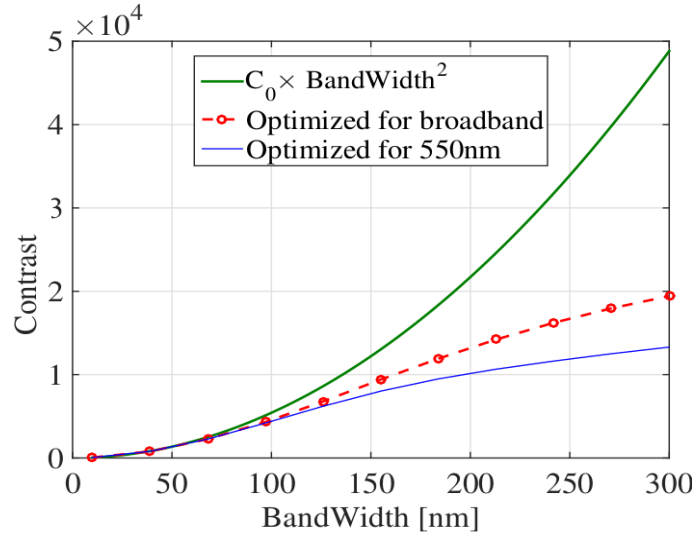


Figure 3.8: **Scene 2** : Contrast as a function of bandwidth of the system with $\tau^2/\sigma^2 = 1$ for Scene 2.

Equation (3.2). It is worth noticing that in this case the increase of light flux always overcomes the loss of polarimetric accuracy since the contrast monotonously increases as the spectral width broadens. The loss of contrast compared to the $C_0\Delta\lambda^2$ case remains important, nevertheless.

However, if we search for the configuration (θ_1, θ_2) that maximizes the contrast of equation (3.2) for each value of the bandwidth, one can see that the contrast can be further increased (red dashed curve in figure 3.8).

3.2.3 Discussion

In this numerical study, we have analyzed the impact of spectral broadening on the contrast value for two different kinds of scenes composed of ideal components. Similar behaviors were highlighted.

On the one hand, for both scenes, the contrast is globally enhanced when we increase the bandwidth of the light entering the system, even if the set-up is optimized for a specific wavelength. This shows that the increase of intensity overcomes the loss of polarimetric accuracy in the contrast calculation. However, for situations where several configurations of the PSG and PSA lead to the same optimal contrast for a given wavelength, some configurations may result in a decrease of contrast for a particular bandwidth as the mismatch of the properties of the set-up between all the wavelengths becomes too high.

On the other hand, it is shown that optimizing the contrast by taking specifically into account the broadband characteristic of the set-up leads to a significant contrast enhancement. In this case, the bandwidth simply appears as a supplementary parameter that has to be taken into account to optimize the system.

3.3 Experimental study

3.3.1 Description of the experimental set-up

In order to verify the results of the numerical simulation, we performed a laboratory experiment with a division of time polarimeter (DOTP) in standard reflection configuration described in [13]. The system is an adaptive imager which can generate and analyze any polarization state defined on the Poincaré sphere. The light source is a cold halogen white light fiber source (Qioptiq, LQ 1100) which produces unpolarized light. The PSG as well as PSA consists of two nematic liquid crystal variable retarders (LCVR) (Meadowlark Optics) and a linear polarizer which are positioned as described in Section 2.2.4. The image is acquired using a CCD camera (AVT Stingray - F033). Figure 3.9 presents a scheme of the complete set-up.

The scene of interest is composed of two different objects as shown in figure 3.10(a). The background of the scene is made up of an uniform metallic plate and the target to detect is a piece of birefringent material (translucent adhesive tape) placed over the plate. The standard intensity image of the scene is shown in figure 3.10.b and, as one can see, the target cannot be distinguished on this image.

A picture of the experimental set-up of an active adaptive polarimetric imager built in laboratory is shown in figure 3.11.

3.3.2 Results and discussion

As in the numerical study, we first place a narrowband filter in front of the camera. The filter is centered on 640 nm with a bandwidth of 10 nm. We then measure the Mueller matrix of the scene, and using Eq. (2.21) and (2.22), we determine the optimal configuration for the central wavelength $(\theta_1^{\text{opt}}, \theta_2^{\text{opt}}) = (2.96, 4.13, 2.58, 3.63)$ V and implement it on the system. We obtain the image of Fig. 3.12(a) for an exposure time of 100 ms. One can see that the contrast has been improved in comparison to standard intensity image (see Fig. 3.10.b). However, if we strongly reduce the acquisition time to 2 ms, for example

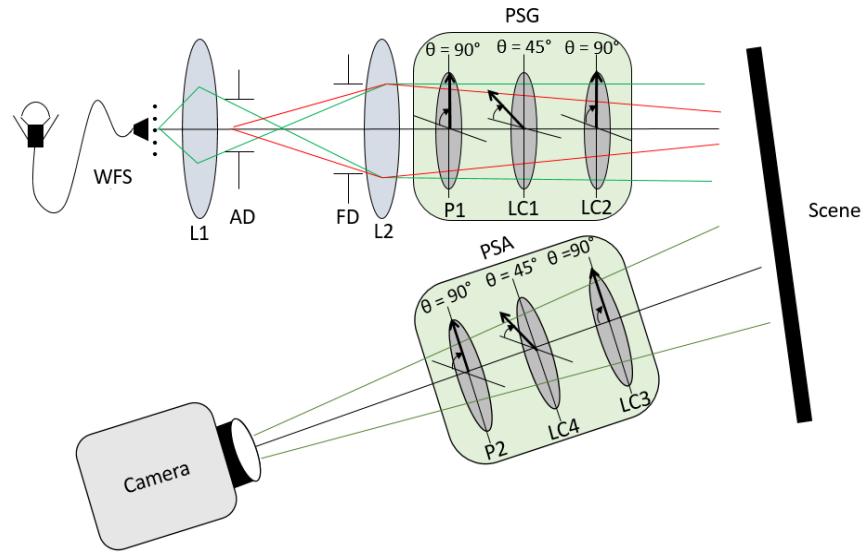


Figure 3.9: Experimental design of active adaptive broadband polarimetric imaging for contrast optimization. The major difference between the standard active adaptive polarimetric imager (see figure 2.11) and broadband active adaptive polarimetric imager is the absence of spectral filter.

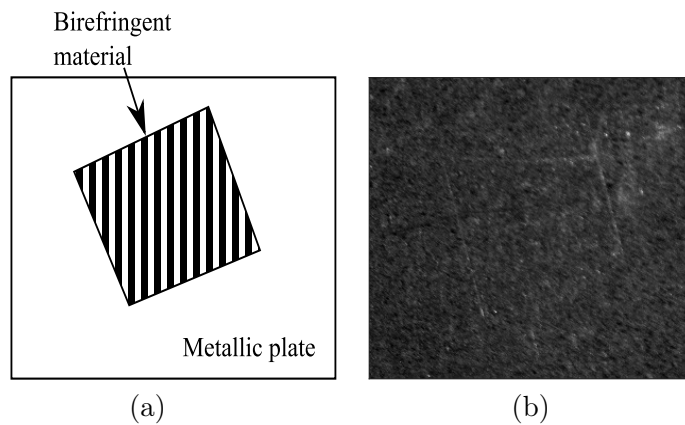


Figure 3.10: (a) Scheme of observed scene (b) standard intensity image, with an exposure time $\tau = 100$ ms.

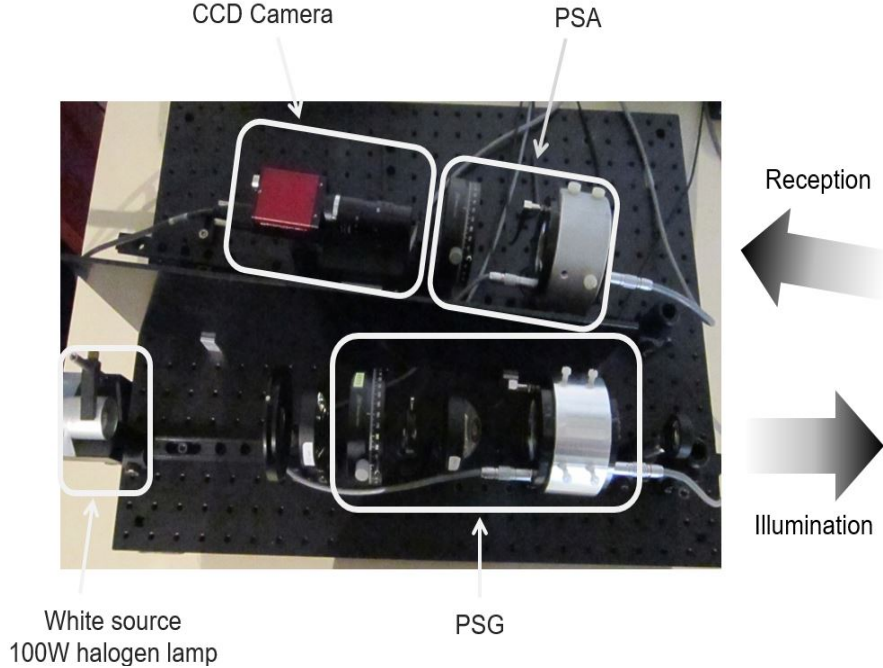


Figure 3.11: Experimental set up of active adaptive broadband polarimetric imager.

| <i>Configuration</i> | ΔI (gray levels) | $C_{\text{exp}} (\times \frac{10^3}{\sigma^2})$ |
|---|-----------------------------|---|
| Optimized for 640 nm, with the filter | 9 | 0.09 |
| Optimized for 640 nm, without the filter | 690 | 476 |
| Optimized for broadband, without the filter | 843 | 711 |

Table 3.4: Summary of the different experimental configurations and results (exposure time = 2ms).

to increase the acquisition speed, we obtain Fig. 3.12(b). One can now see that the contrast has strongly decreased, due to the presence of high sensor noise. This can be quantified by computing the intensity distribution of the regions of interest. Figure 3.13(a) and Figure 3.13(b) show the distributions for the target (in blue) and the background (in red). The dashed blue line represents the value of the average intensity $\langle i_t \rangle$ over the target region and the dashed red one the average value $\langle i_b \rangle$ over the background region. The histograms were shifted in order to have $\min\{\langle i_t \rangle, \langle i_b \rangle\} = 0$. The experimental contrast C_{exp} can then be calculated using $\Delta I = |\langle i_t \rangle - \langle i_b \rangle|$ and equation (2.16). We obtain $C_{\text{exp}} = 4.57 \times 10^5 / \sigma^2$ and $C_{\text{exp}} = 90 / \sigma^2$, for $\tau = 100$ ms and $\tau = 2$ ms respectively.

If we now remove the filter without changing the configuration of the PSG and PSA, we obtain the image of Figure 3.12(c). We can see that the visual contrast has improved even if the configuration we use is not optimal for the other wavelengths of the bandwidth. This is due to the increase of light flux in the system. It can be quantitatively confirmed using the histograms of Fig. 3.13(c) and by calculating the new contrast $C_{\text{exp}} = 4.76 \times 10^5 / \sigma^2$. Now, if we perform an exhaustive search by varying the voltages of the LCVR to find the configuration that optimizes the contrast without the filter, we find that the optimal configuration is $(\theta_1^{\text{opt}}, \theta_2^{\text{opt}}) = (6.17, 2.77, 5.44, 3.87)$ V and we obtain the image of Figure 3.12(d) with the histograms of Figure 3.13(d). We can see that the optimal configuration is different from the previous monoband case, and we have further enhanced the contrast to reach a value of $C_{\text{exp}} = 7.11 \times 10^5 / \sigma^2$.

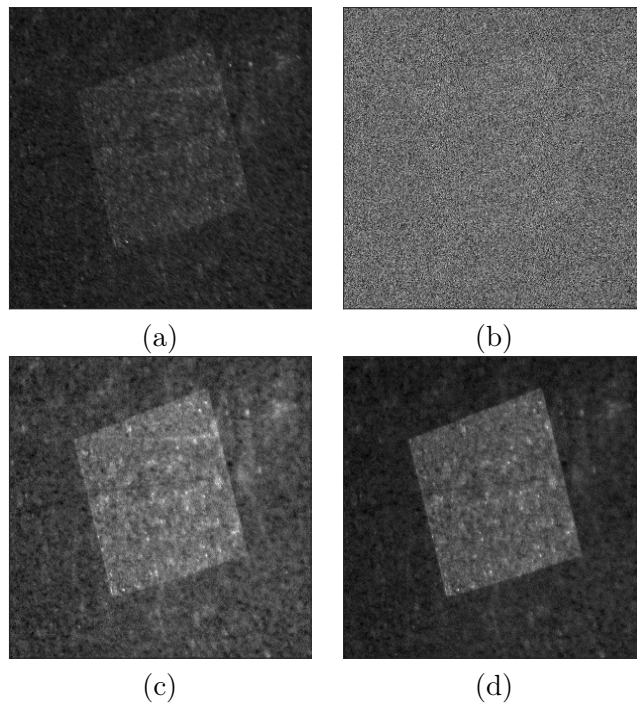
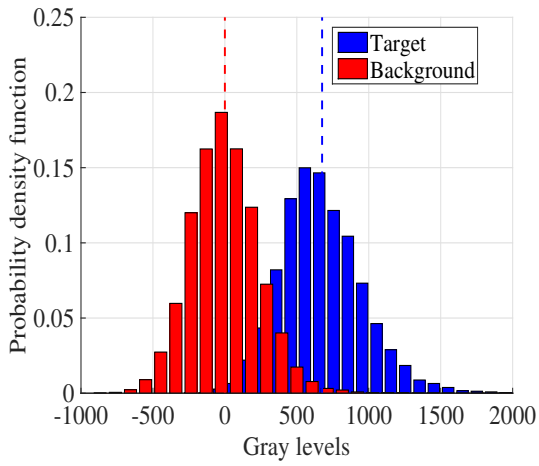
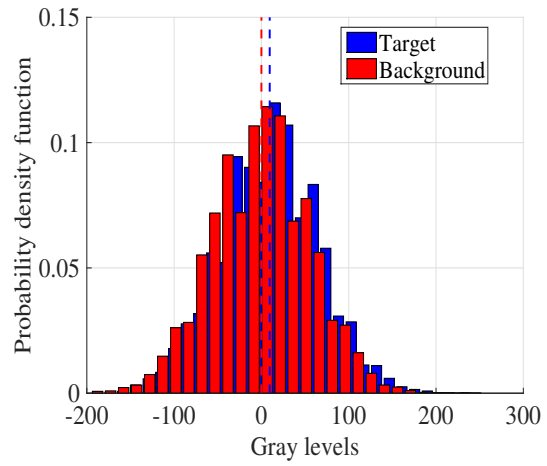


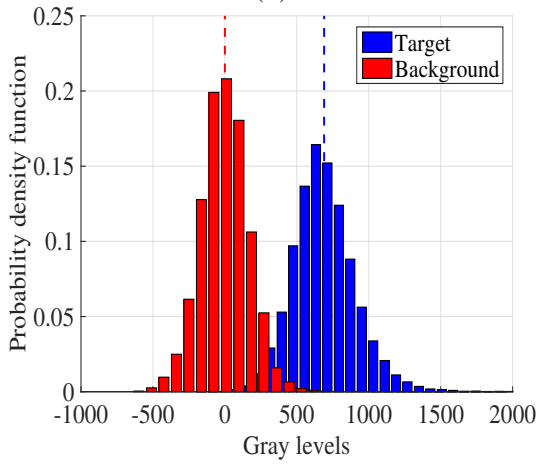
Figure 3.12: (a) Intensity image taken using the 10 nm-wide narrowband filter centered at $\lambda = 640$ nm and the PSG/PSA configuration optimal for 640 nm, with an exposure time of 100 ms (b) Same image for an exposure time of 2ms (c) Intensity image taken without the filter using the PSG/PSA configuration optimal for 640 nm and an exposure time of 2 ms (d) Intensity image taken without the filter after optimizing the PSG/PSA configuration optimal for the bandwidth and with an exposure time of 2ms.



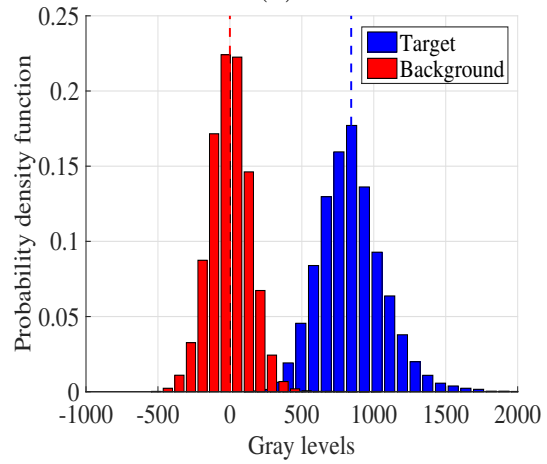
(a)



(b)



(c)



(d)

Figure 3.13: (a) Histogram of figure 3.12(a). (b) histogram of figure 3.12(b). (c) histogram of figure 3.12(c) (d) histogram of figure 3.12(d).

Table 3.4 summarizes the results obtained for the different configurations for an acquisition time of 2 ms. We can see that increasing the bandwidth of the system allows to enhance the contrast and that by taking into account the broadening of the bandwidth we are able to find an optimal configuration that further increases the contrast and thus compensates the loss of polarimetric accuracy of the system.

3.4 Conclusion

In this chapter, we have shown that in active polarimetric imaging, contrast can be increased by broadening the spectral width of the light entering the system. Indeed, the increase of light flux overcomes the contrast decrease due to the mismatch of the system component properties caused by the broadening. In addition, contrast can be further improved by optimizing the PSG and PSA configuration with respect to the bandwidth. In this case, the optimal configuration is in general different from that obtained in the narrowband case.

These results illustrate that for target detection applications, an active polarimetric imaging system should no longer be seen only as a tool to estimate polarimetric properties but also as a tunable device allowing to acquire relevant information for optimal target detection. In this case, spectral width is simply a new parameter to optimize the polarimetric imaging architecture. These findings open new perspectives for high-speed polarimetric imaging in applications where contrast optimization is required.

This work has many perspectives. In the present system, the optimal configurations of the PSA and PSG in the broadband case have been found by exhaustive search. In order to decrease the computation time of the optimization, one needs to quickly estimate the Mueller matrix of the scene. Moreover, a polarimetric imager with high acquisition speed and high signal-to-noise ratio images can be interestingly applied to such fields as microscopy or industrial visual inspection. Finally, studying the impact of bandwidth increase on the precision of Mueller matrix estimation is also a very interesting perspective since it would allow one to quantify to what extent a polarization imager has to be achromatized for a given application.

Chapter 4

Spectral bandwidth optimization using measurements of multi-spectral Mueller matrices

We saw in the chapter 3 that it is possible to improve contrast in a polarization image by increasing spectral bandwidth alone. We also found that a further optimization of voltages in PSG/PSA taking into account the spectral dependence of the scene and the optical elements could enhance the contrast further. However, the contrast optimization process consumes a lot of time since we try all possible combinations of polarization states corresponding to illumination and detection on optical bench by manipulating voltages of the LCVRs in PSG/PSA. The speed of this exhaustive search is determined by factors such as the response time of liquid crystal retarders, the integration time of camera and the speed of computer processor.

A good solution to accelerate the optimization process is to measure the Mueller matrix of the scene at discrete wavelengths within the spectral range of interest. This provides multispectral polarization information of the scene, only limited by the spectral discretization steps we choose. This solution can be made possible only if we calibrate the voltage-phase delay response of LCVRs at different wavelengths. Then, we can measure multispectral Mueller matrices by standard Mueller imaging procedure and thus we have access to the data necessary to conduct numerical study of contrast optimization in broadband spectrum. The main objective of this chapter is to study how the prior determination of multispectral Mueller matrices help us to conduct the contrast optimization of polarimetric imaging in broadband spectrum efficiently.

In this chapter, we first discuss about the LCVR calibration for multispectral applications. Then, we introduce an another scene made up of two different kinds of materials. We determine the Mueller matrices of these two materials at different wavelengths. Subsequently, we discuss a numerical and experimental study of contrast optimization of polarization image of this scene in narrowband as well as broadband spectrum with calibrated LCVRs in PSG/PSA.

4.1 Calibration of LCVRs for multispectral applications

In this section, we discuss the requirement and benefits of LCVR calibration for multispectral applications. We saw in Chapter 3 that the Mueller matrix determination of a scene/object is a required step in the contrast optimization process. For the determination of the Mueller matrix with minimum estimation variance, a given set of polarization states are required for illumination and detection [23, 40]. Implementation of these polarization states requires the information about the voltage phase-delay response at the

working wavelength.

The LCVRs in the PSG/PSA of our laboratory are ideally designed for use at $\lambda = 640$ nm. Therefore, the voltage-phase delay response of the LCVRs at $\lambda = 640$ nm was known to us. But we did not have access to the voltage-phase delay response at other wavelengths. As a result, we were not able to conduct Mueller imaging at other wavelengths.

We used a spectroscopic ellipsometer (manufactured by Horiba scientific) with spectral resolution of 3 nm to calibrate the voltage-phase delay response of the LCVRs in the following wavelengths : 450 nm, 500 nm, 550 nm, 600 nm, 650 nm, 700 nm, 750 nm and 800 nm. We measured phase delay for different voltages at different wavelengths and then applied standard interpolation techniques to fill the missing information between experimentally determined points. The response curve obtained after the calibration is displayed in the figure 4.1. Now that we have access to voltage-phase delay response of the LCVRs at these wavelengths, we can measure the multispectral Mueller matrices with minimum estimation variance. We will discuss about the measured multispectral Mueller matrices of the scene in the next section.

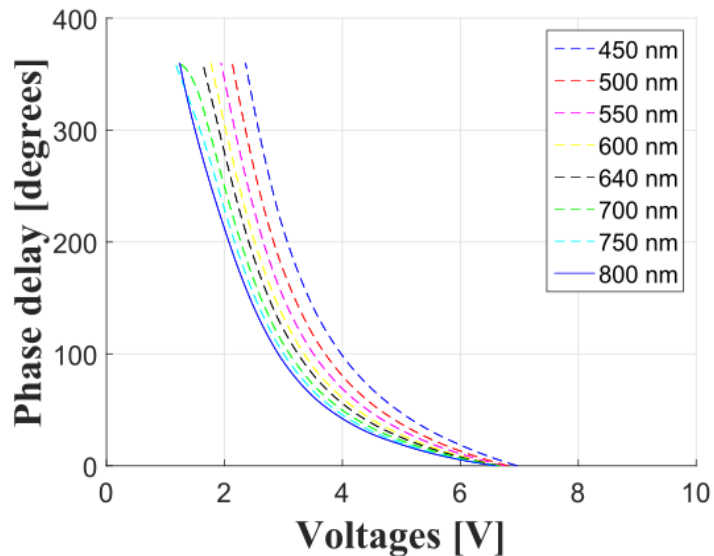


Figure 4.1: Liquid crystal variable retarder response curve : phase delay as function of voltages at 30°C for different wavelengths (measured using a spectroscopic ellipsometer manufactured by Horiba scientific and operated with the help of LPICM, Ecole polytechnique, Palaiseau).

4.2 Contrast optimization in multispectral polarimetric imaging

In this section, we study contrast optimization of the polarization image of a new artificial scene at different wavelengths by numerical computation and experimental verification. The scene is made up of sandpaper on which different layers of adhesive scotch tape are pasted in different orientations as shown in figure 4.2(a). The section in the middle of scene is selected as target and the rest of the scene is selected as background. Both regions are painted using gold spray paint, therefore not distinguishable from each other for naked eye/standard intensity imaging. We choose region A as target and region B as background. Figure 4.2(b) shows the standard intensity image of the scene in gray scale. We can see that the target is indistinguishable from the background.

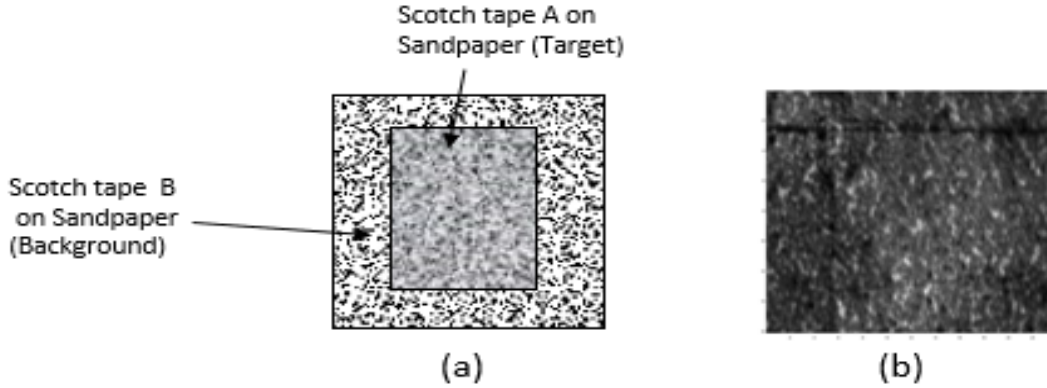


Figure 4.2: (a) Schematic diagram of the scene. The target consists of two layers of scotch tape pasted on sandpaper with a given orientation and the background consists of sandpaper covered by another scotch tape with a different orientation. (b) Intensity image of the scene for an integration time of $\tau = 300$ ms.

4.2.1 Multispectral Mueller matrix of the scene

The Multispectral Mueller matrices of the scene provide information about how polarization properties such as diattenuation, retardance and depolarization of target/background vary with wavelength. We measured the Mueller matrix by the standard Mueller imaging procedure explained in Section 1.2.1 at several wavelengths ranging from 450 nm to 700 nm. Though Mueller matrix determination in full spectral continuum is desirable, it is impractical to do so in our case due to lack of spectral filters available in all wavelengths. In our lab, we have spectral filters with central wavelength at 450 nm, 500 nm, 550 nm, 600 nm, 650 nm and 700 nm with 10 nm full width half maximum (FWHM).

From the regions classified as target and background in Mueller images, we derived the average Mueller matrices at the different wavelengths. The components of Mueller matrices, plotted as functions of the wavelength, are shown in figure 4.3. The Mueller matrices are normalized with respect to their first element, m_{00} , which represents pure intensity reflectivity information. Figure 4.3 shows that the polarization properties of the target and background are very similar to that of birefringent materials. Indeed, the Mueller matrix of a waveplate made up of birefringent material at rotation angle $\theta = 0^\circ$ is represented as [19]

$$\mathbf{M}_{wp}(\theta = 0^\circ, \varphi) = \begin{pmatrix} 1 & 0 & 0 & 0 \\ 0 & 1 & 0 & 0 \\ 0 & 0 & \cos \varphi & \sin \varphi \\ 0 & 0 & -\sin \varphi & \cos \varphi \end{pmatrix}, \quad (4.1)$$

where $\varphi = \frac{2\pi}{\lambda}(\Delta n l)$ is the phase delay between the eigen polarization states with Δn , l and λ being respectively the birefringence of the material, its thickness and the wavelength of the light. The difference observed in the lower right 3×3 block of equation 4.1 and figure 4.3 can be explained by measurement uncertainties and the fact that the orientation of the materials used in the scene is $\theta \neq 0^\circ$. However, the right lower 2×2 block of figure 4.3 is consistent with the form of distorted cosine and sine waves.

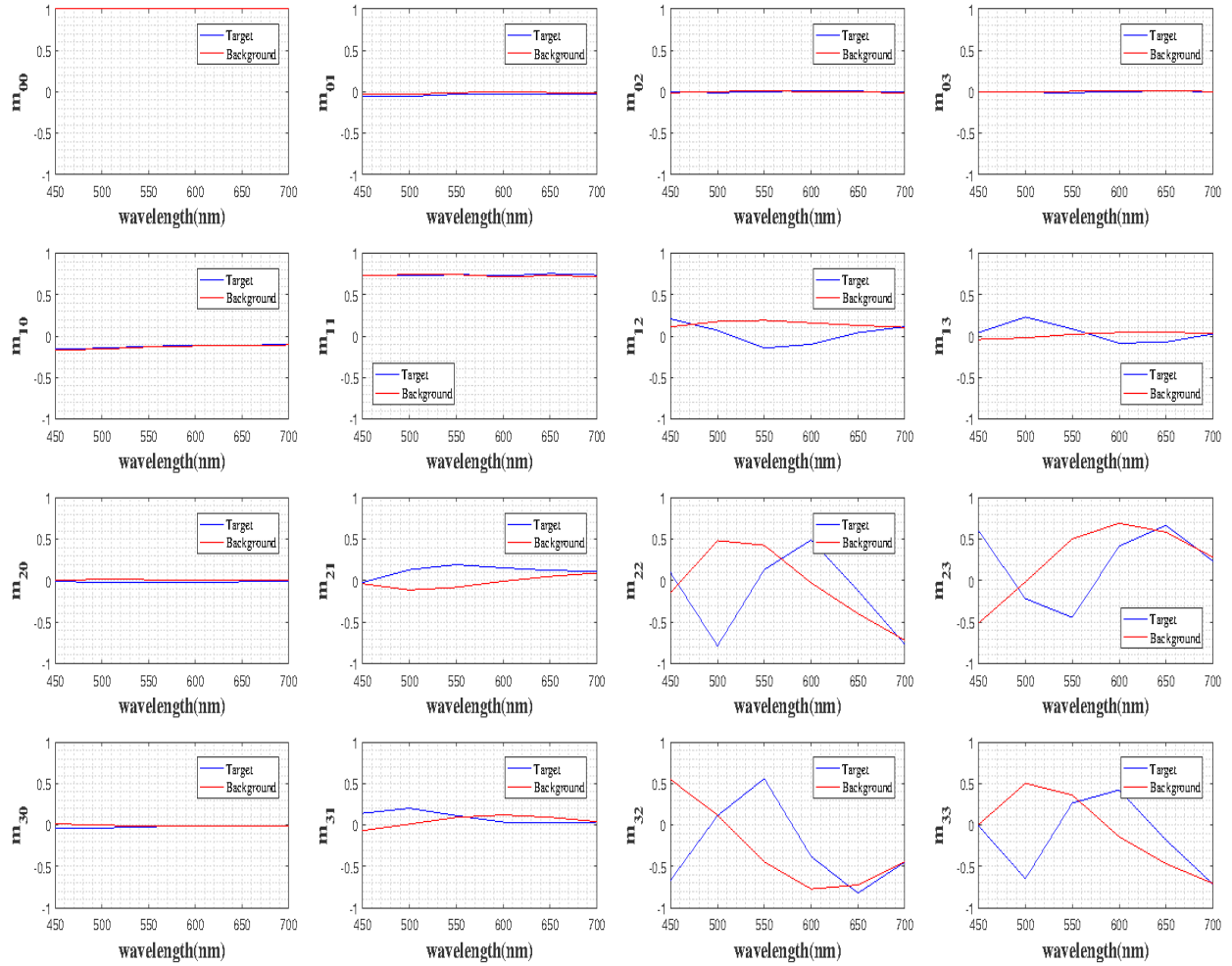


Figure 4.3: Normalized multispectral Mueller matrix of the regions chosen as target and background. Mueller matrix elements are normalized with respect to m_{00} which represents pure intensity information. All 16 elements of matrix are plotted as function of wavelength starting from 450 nm to 700 nm with 50 nm step.

Therefore, we can conclude that target and background are essentially birefringent which is consistent with the materials used on the scene (adhesive tapes). This prior knowledge of the scene characteristics can be useful to interpret the results of contrast optimization as well as to improve the optimization procedure as we will see later in this chapter.

4.2.2 Numerical study

In Chapter 3, we presented the numerical study of broadband contrast optimization using multispectral Mueller matrices of a hypothetical scene since we could not determine multispectral Mueller matrices of a real world scene with polarimetric imaging system. Now that we have calibrated PSG/PSA for multispectral use, the multispectral Mueller matrix measurements are possible. This enabled us to conduct numerical study of contrast optimization at several wavelengths. Using equations 2.20, 2.21, 2.22 and experimentally measured Mueller matrices at several wavelengths, we generated contrast optimized polarization images by simulation and they are shown in figure 4.4 along with their histograms displayed in figure 4.5. Table 4.1 presents statistical analysis of the polarization images in figure 4.4. We calculated contrast in the polarization images by using following equation (see Section 2.2.4 for the derivation):

$$C = \frac{1}{8\sigma^2}(\langle i_t \rangle - \langle i_b \rangle)^2. \quad (4.2)$$

where $\langle i_t \rangle$ and $\langle i_b \rangle$ represent statistical average intensity of the target and the background, and σ^2 denotes variance of additive Gaussian noise with zero mean. For the statistical analysis of images, let us introduce σ_t^2 and σ_b^2 which represent statistical intensity variance of the target and the background respectively.

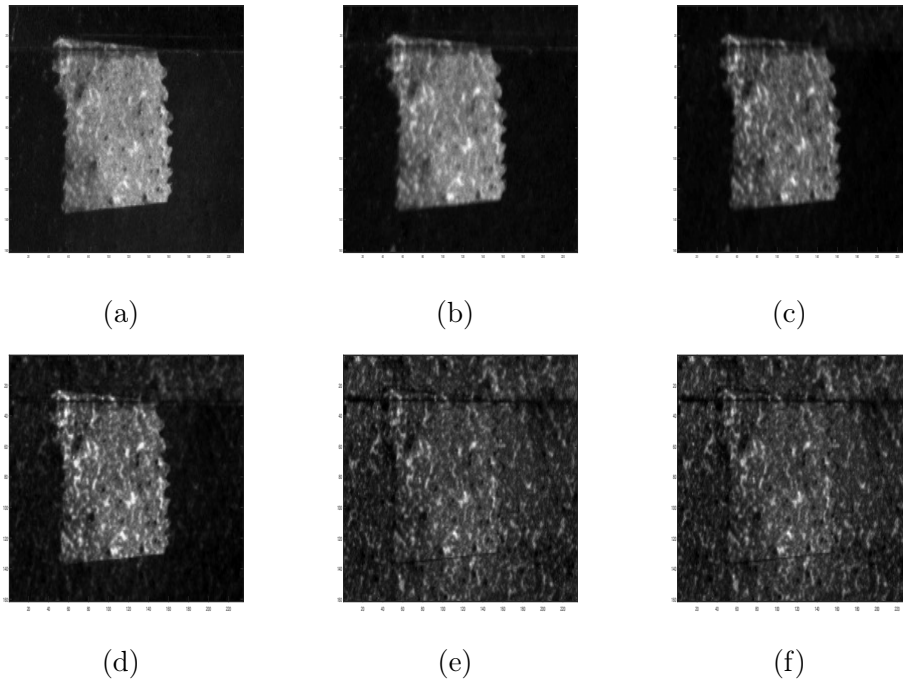


Figure 4.4: Simulated polarization images with optimal contrast for (a) 450 nm (b) 500 nm (c) 550 nm (d) 600 nm (e) 650 nm (f) 700 nm. The integration time of camera, $\tau = 300$ ms. The dynamic range of the image is set automatically between the minimal and maximal intensity value of the image.

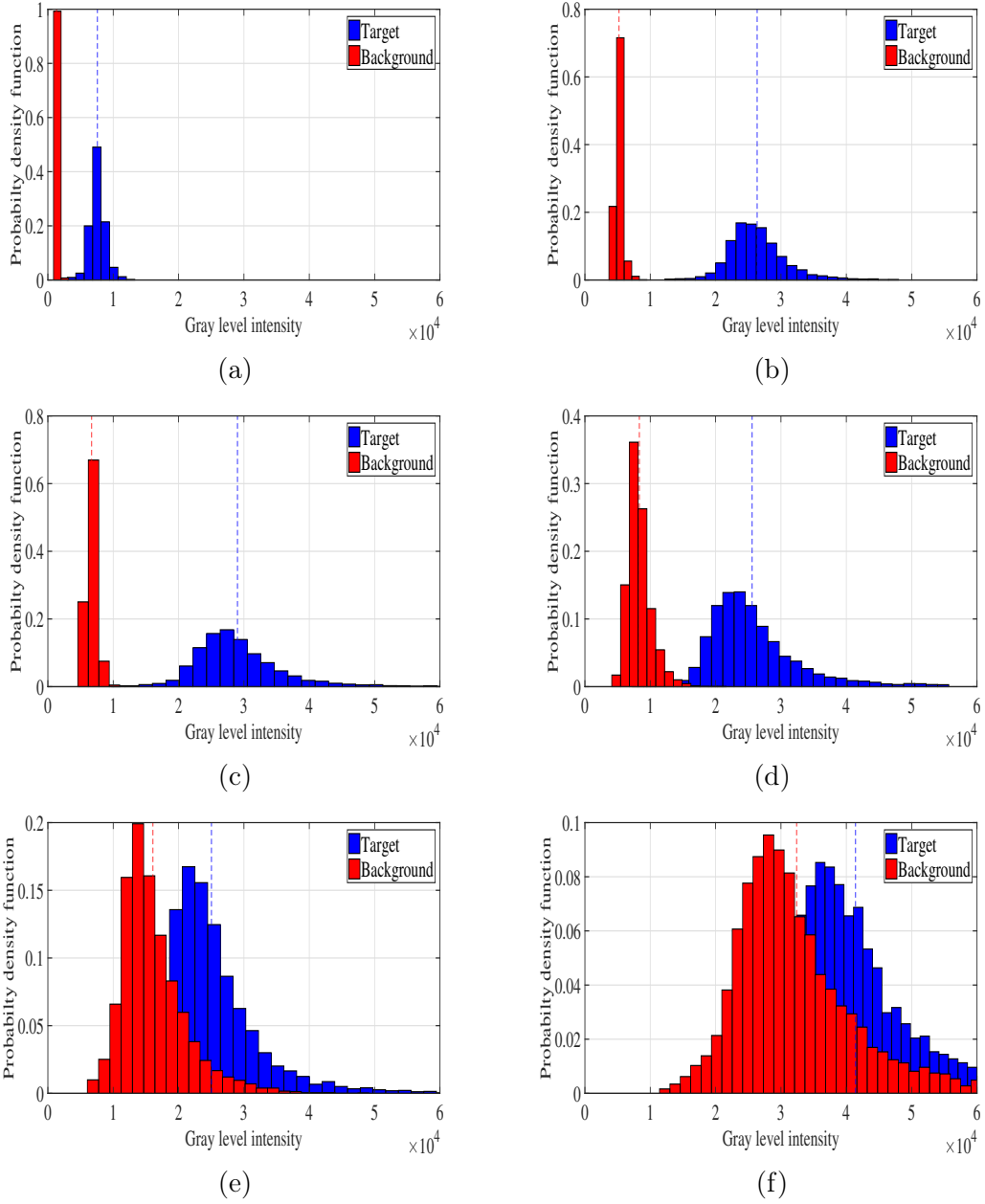


Figure 4.5: Histograms of images of figure 4.4 at (a) 450 nm (b) 500 nm (c) 550 nm (d) 600 nm (e) 650 nm (f) 700 nm. The blue and red colour bars represent target and background respectively.

| λ (nm) | $(\theta_{1,opt}^\lambda, \theta_{2,opt}^\lambda)$ (V) | $\langle i_t \rangle$ $\times 10^3$ | $\langle i_b \rangle$ $\times 10^3$ | σ_t^2 $\times 10^3$ | σ_b^2 $\times 10^3$ | C ($\times \frac{1}{\sigma^2}$) $\times 10^5$ |
|-------------------|---|--|--|-------------------------------|-------------------------------|--|
| 450 | 4.20, 4.00, 3.60, 2.80 | 8 | 1 | 1370 | 32 | 392 |
| 500 | 2.40, 2.40, 4.60, 4.00 | 26 | 5 | 19600 | 294 | 4460 |
| 550 | 3.80, 3.40, 3.20, 4.00 | 29 | 7 | 44500 | 560 | 4970 |
| 600 | 3.60, 3.20, 2.60, 4.20 | 26 | 8 | 47652 | 3291 | 2980 |
| 650 | 3.80, 2.20, 2.80, 3.80 | 25 | 16 | 46000 | 24200 | 802 |
| 700 | 3.80, 3.00, 4.20, 3.60 | 41 | 32 | 91900 | 93900 | 815 |

Table 4.1: Statistical parameters of simulated polarization images for maximum contrast in narrowband spectrum (shown in figure 4.4). The contrast values in the images are calculated using equation 4.2. Camera integration time, $\tau = 300$ ms.

Discussion

We have optimized contrast between target and background in the scene at different wavelengths. The optimal voltages corresponding to maximum contrast are different at different wavelengths. In the contrast expression, only the magnitude of the intensity difference between the two regions is taken into account for the calculation of contrast. Intensity variance across target and background is assumed to be constant and negligible.

The best visual contrasts are obtained for 450 nm, 500 nm, 550 nm and 600 nm (see figure 4.4). As we can see on figure 4.3, it corresponds to the wavelengths where the background and target display the most distinct polarimetric properties. For 500 nm, 550 nm and 600 nm, this is confirmed by the contrast values on table 4.1, the best contrast being obtained for 550 nm.

For 450 nm, the good visual contrast is explained by the fact that the dynamic range of the image is set automatically between the minimal and maximal intensity value of the image, whereas the low contrast value on table 4.1 can be explained by the relative low response of the light source and the camera as it can be seen on figure 3.2.

For 650 nm and 700 nm, we can see on figures 4.4(e) and 4.4(f) that the optimization leads to very poor visual contrast. First, we can see on figure 4.3, it corresponds to the wavelengths where the background and target display similar polarimetric properties. Moreover, for these wavelengths the spatial intensity variance over the target and the background becomes large, as shown on the histograms 4.5(e) and 4.5(f), and should not be neglected in the optimization procedure. Therefore, for these wavelengths another noise model should then be considered [41].

4.2.3 Experimental study

We have implemented the optimal voltages found out by numerical contrast optimization process on optical bench to verify the conclusion from numerical studies for all wavelengths considered. The results are displayed in figure 4.6, 4.7 and table 4.2.

From the figures 4.6, 4.7 and the table 4.2, we can see that the experimental results display the same behaviors as in the numerical study. First, the best visual contrasts are obtained for 450 nm, 500 nm, 550 nm and 600 nm. For the latter three wavelengths, it is confirmed by the contrast values on table 4.2. Once again, for 450 nm, we obtain low contrast value which is explained by the low response of the set-up at this wavelength. Then, the poor contrast for the two last wavelengths 650 nm and 700 nm is also due to the influence of the intensity variance over the target and background regions as shown on histograms 4.7(e) and 4.7(f).

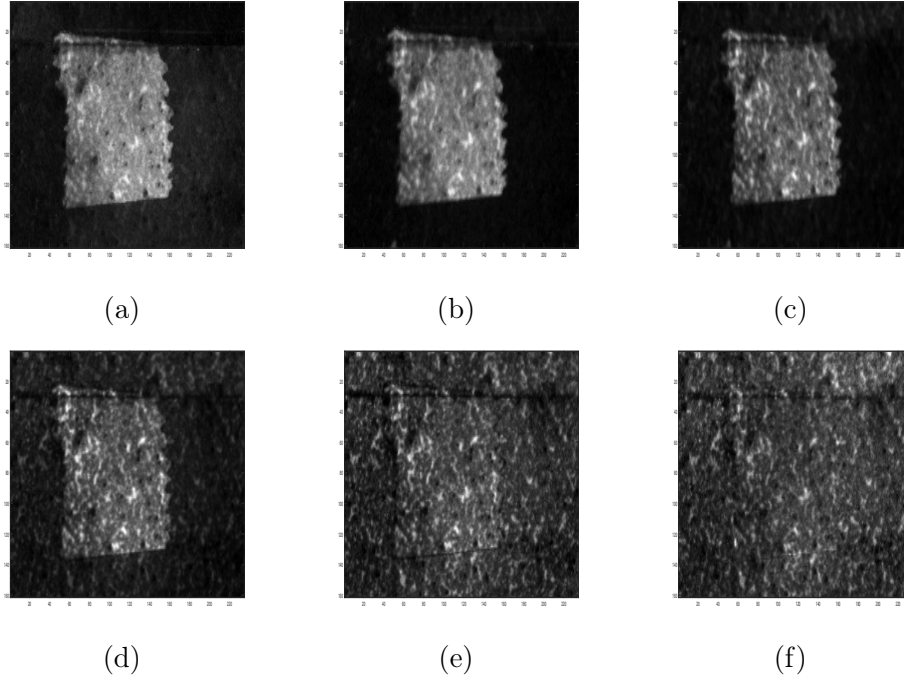


Figure 4.6: Experimental polarization images with maximum contrast at (a) 450 nm (b) 500 nm (c) 550 nm (d) 600 nm (e) 650 nm (f) 700 nm. The integration time of camera, $\tau = 300$ ms. The dynamic range of the image is set automatically between the minimal and maximal intensity value of the image.

| λ (nm) | $(\theta_{1,opt}^\lambda, \theta_{2,opt}^\lambda)$ (V) | $\langle i_t \rangle$ $\times 10^3$ | $\langle i_b \rangle$ $\times 10^3$ | σ_t^2 $\times 10^3$ | σ_b^2 $\times 10^3$ | $C (\times \frac{1}{\sigma^2})$ $\times 10^5$ |
|-------------------|---|--|--|-------------------------------|-------------------------------|--|
| 450 | 4.20, 4.00, 3.60, 2.80 | 8 | 2 | 1350 | 47 | 318 |
| 500 | 2.40, 2.40, 4.60, 4.00 | 26 | 6 | 18600 | 303 | 3790 |
| 550 | 3.80, 3.40, 3.20, 4.00 | 32 | 10 | 45100 | 1030 | 4750 |
| 600 | 3.60, 3.20, 5.19, 2.00 | 28 | 12 | 54900 | 8910 | 2500 |
| 650 | 3.80, 2.20, 2.80, 3.80 | 26 | 16 | 47400 | 2400 | 945 |
| 700 | 3.80, 3.00, 4.20, 3.60 | 41 | 32 | 83500 | 90900 | 837 |

Table 4.2: Statistical parameters of experimental polarization images with maximum contrast in narrow-band spectrum at different wavelengths. The contrast values in the images are calculated using equation 4.2. The spectral filters used in imaging system have FWHM of 10 nm. Camera integration time, $\tau = 300$ ms.

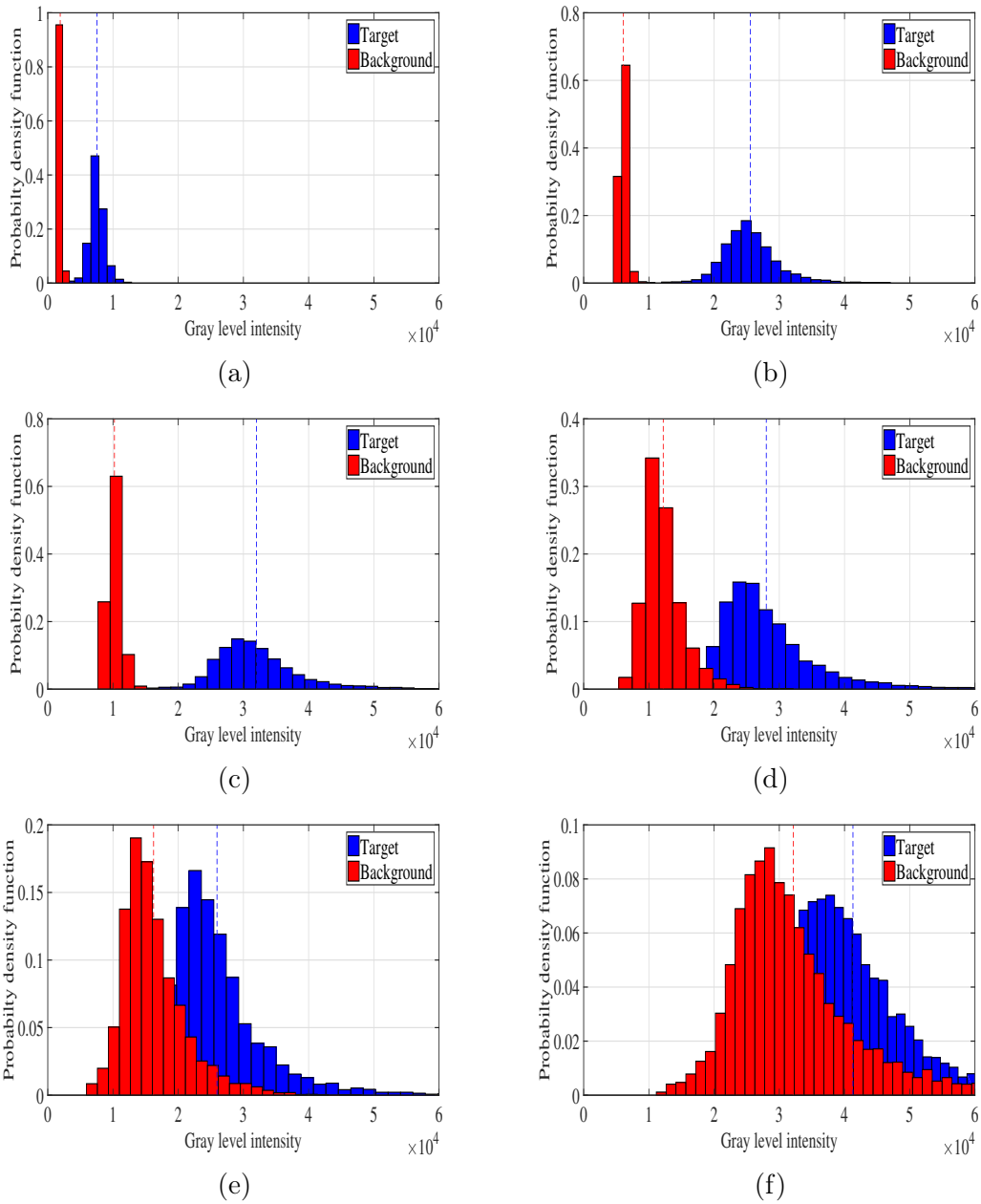


Figure 4.7: Histogram of polarization images shown in figure 4.6 for wavelength (a) 450 nm (b) 500 nm (c) 550 nm (d) 600 nm (e) 650 nm (f) 700 nm. The blue and red colour bars represent target and background respectively.

4.3 Contrast optimization in broadband polarimetric imaging

Now that we have access to the Mueller matrices of the scene from 450 nm to 700 nm with 50 nm step and voltage - phase delay response data of LCVRs, we could simulate numerically the contrast optimization process of polarization image in broadband spectrum.

4.3.1 Numerical study

As defined in the last chapter, we calculate the contrast in broadband polarization images using the following relation :

$$C_{\Delta\lambda}(\theta_1, \theta_2) = \frac{\tau^2}{32\sigma^2} \left(\int_{\Delta\lambda} \rho(\lambda) [\chi_{\theta_1}(\lambda) + \mathbf{t}_{\theta_2}^{\mathbf{T}}(\lambda)u_{\theta_1}(\lambda)] d\lambda \right)^2, \quad (4.3)$$

where $d\lambda$ is the bandwidth of the system. However, we use a discretized form of this expression to carry out numerical study, as shown below :

$$C_{\Delta\lambda}(\theta_1, \theta_2) = \frac{\tau^2}{32\sigma^2} \left(\sum_{\lambda=\lambda_i}^{\lambda=\lambda_f} \rho(\lambda) [\chi_{\theta_1}(\lambda) + \mathbf{t}_{\theta_2}^{\mathbf{T}}(\lambda)u_{\theta_1}(\lambda)] \delta\lambda \right)^2, \quad (4.4)$$

where $\delta\lambda = \frac{\lambda_f - \lambda_i}{n}$. The λ_i, λ_f represents initial and final wavelength of the spectrum we consider, n and $\delta\lambda$ represent number of divisions in the spectrum and wavelength step respectively. An illustration of integration by summation is shown in figure 4.8. We measure Muller matrices at different wavelengths ranging from $\lambda = 450$ nm to $\lambda = 700$ nm with a step $\delta\lambda = 50$ nm and number of wavelengths $n = 6$. In our case, we assume that the polarization properties of the scene varies smoothly between any two measured spectral Mueller matrices. The total integration time for measuring the Mueller matrices are kept to constant $\tau_0 = 300$ ms meaning that if n measurements are done, each are performed using an integration time of $\tau = \frac{\tau_0}{n}$. Now we optimize the polarimetric imaging system with measured Mueller matrices for maximum contrast using the following relation :

$$(\theta_{1,opt}^{\Delta\lambda}, \theta_{2,opt}^{\Delta\lambda}) = \underset{\theta_1, \theta_2}{\operatorname{argmax}} [C_{\Delta\lambda}(\theta_1, \theta_2)]. \quad (4.5)$$

In the Section 4.2, we saw that the optimized polarization image at $\lambda = 550$ nm has maximum contrast over the other wavelengths. Now, we want to study what happens to the contrast of polarization image of this scene if we broaden the width of spectral filter. We simulated spectral broadening ranging from $\Delta\lambda = 10$ nm to $\Delta\lambda = 300$ nm using measured multispectral Mueller matrices and observed the change in contrast of polarization image. The results are displayed in figure 4.9 along with their histograms in figure 4.10. Table 4.3 summarizes the statistical parameters of simulated polarization images for different spectral bandwidth.

Discussion

From the statistical analysis of images in figure 4.9, we observe that contrast enhancement of polarization images depends upon the spectral range we choose. Higher the Mueller matrix difference between target and background in the chosen spectral range, larger the contrast we observe in the polarization images. From the table 4.3, we observe that for the polarization image whose spectral range is 475 nm - 575 nm, $C_{\Delta\lambda} = 58586 \times 10^5 / \sigma^2$. This is the image with maximum contrast in the table. The polarization image

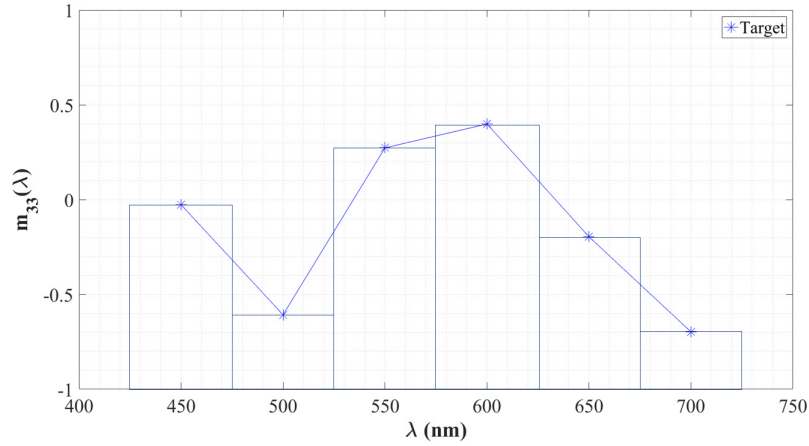


Figure 4.8: Illustration of integration as summation. The figure shows an area bounded by x-axis at $\lambda = 450$ nm and $\lambda = 700$ nm and the curve $m_{33}(\lambda)$ in y-axis. Here λ is the variable and m_{33} represents an element of Mueller matrix taken from figure 4.3. We divide the total area into thin strips with $\delta\lambda = 50$ nm width centered at λ . The area of a thin strip is approximately equal to $\delta A_\lambda \approx m_{33}(\lambda)\delta\lambda$. The total area under the curve = $\sum_{\lambda=450nm}^{\lambda=700nm} \delta A_\lambda$.

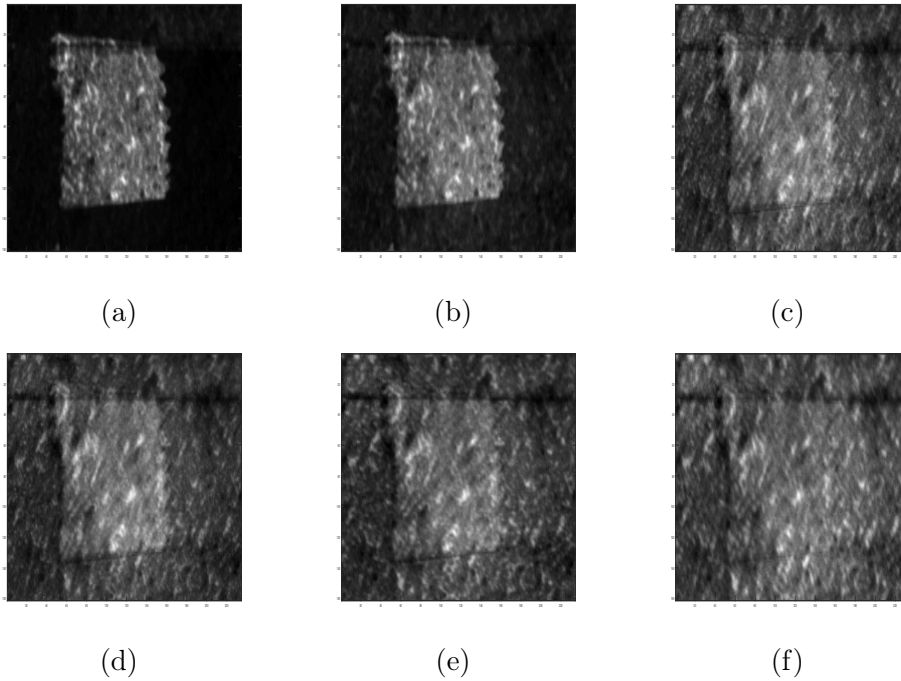


Figure 4.9: Polarization images simulated for maximum contrast at different spectral range, $\Delta\lambda_R$ (and spectral bandwidth, $\Delta\lambda$) (a) 550 nm (10 nm) (b) 475 nm - 575 nm (100 nm) (c) 475 nm - 625 nm (150 nm) (d) 425 nm - 625 nm (200 nm) (e) 425 nm - 675 nm (250 nm) (f) 425 nm - 725 nm (300 nm). Total integration time of camera, $\tau = 300$ ms.

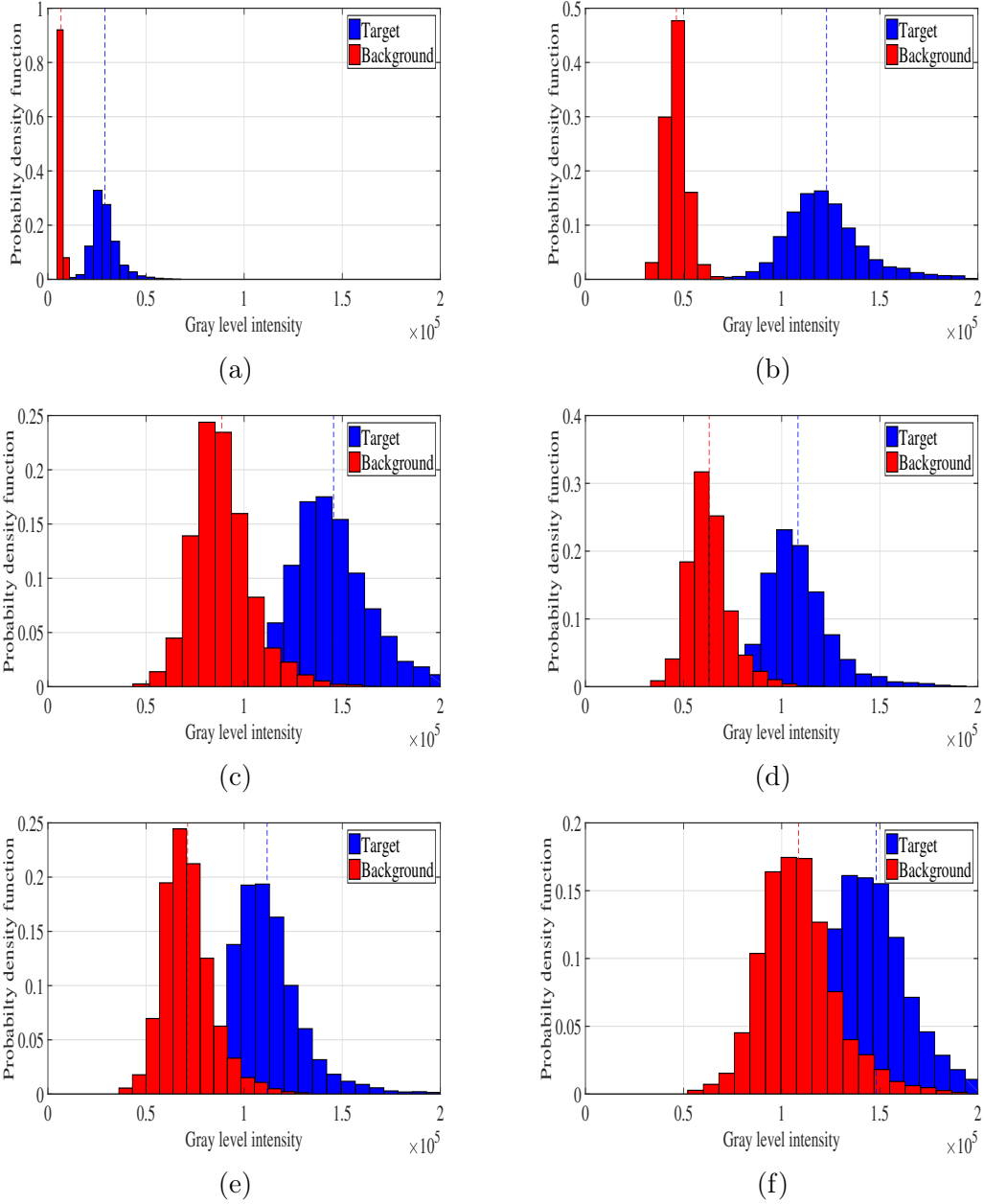


Figure 4.10: Histograms of images shown in figure 4.9 with different spectral range, $\Delta\lambda_R$ (and spectral bandwidth, $\Delta\lambda$) (a) 550 nm (10 nm) (b) 475 nm - 575 nm (100 nm) (c) 475 nm - 625 nm (150 nm) (d) 425 nm - 625 nm (200 nm) (e) 425 nm - 675 nm (250 nm) (f) 425 nm - 725 nm (300 nm).

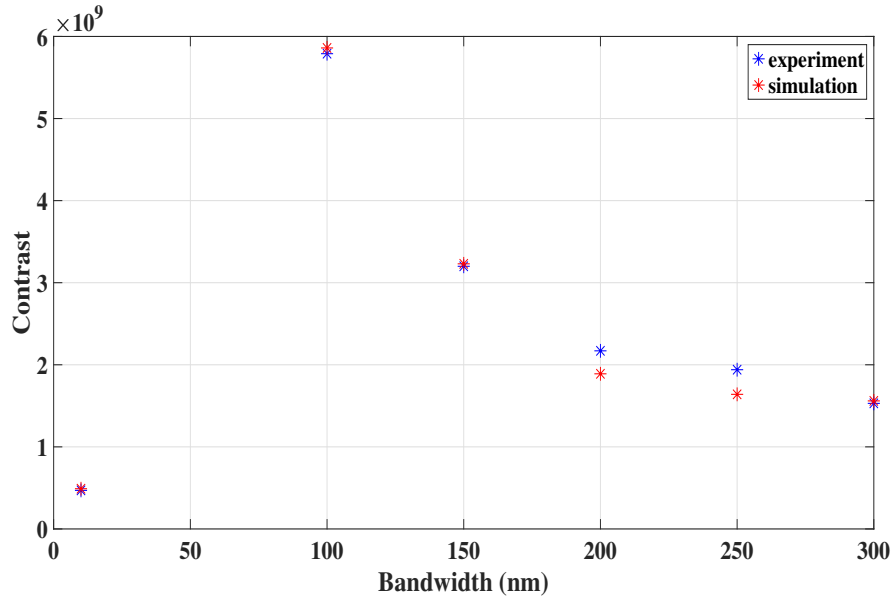


Figure 4.11: The figure shows contrast evolution with increase in spectral bandwidth. The red dots shows numerical results whereas blue dot shows experimental results.

| $\Delta\lambda_R$ (nm) | $\Delta\lambda$ (nm) | $(\theta_{1,opt}^{\Delta\lambda}, \theta_{2,opt}^{\Delta\lambda})$ (V) | $\langle i_t \rangle$ $\times 10^3$ | $\langle i_b \rangle$ $\times 10^3$ | σ_t^2 $\times 10^3$ | σ_b^2 $\times 10^3$ | $C_{\Delta\lambda}(\times \frac{1}{\sigma^2})$ $\times 10^5$ |
|---------------------------|-------------------------|---|--|--|-------------------------------|-------------------------------|---|
| 550 | 10 | 3.80, 3.40, 3.20, 4.00 | 29 | 6 | 44500 | 560 | 4970 |
| 475 - 575 | 100 | 4.20, 3.60, 3.80, 4.20 | 122 | 46 | 461000 | 27600 | 58586 |
| 475 - 625 | 150 | 4.60, 3.60, 3.80, 4.60 | 145 | 88 | 503000 | 230000 | 32349 |
| 425 - 625 | 200 | 2.40, 3.80, 3.60, 2.60 | 108 | 63 | 283000 | 115000 | 20500 |
| 425 - 675 | 250 | 2.40, 3.80, 3.60, 2.60 | 111 | 71 | 296000 | 162000 | 16423 |
| 425 - 725 | 300 | 5.00, 3.60, 4.00, 4.80 | 148 | 108 | 490000 | 379000 | 15585 |

Table 4.3: Statistical analysis of polarization images simulated for different spectral bandwidth, $\Delta\lambda$. The $\Delta\lambda_R$, $\langle i_t \rangle$, $\langle i_b \rangle$ represents spectral range, average intensity of target and background, σ_t^2 , σ_b^2 represents intensity variance of target and background respectively.

with largest spectral range (425 nm - 725 nm) has $C_{\Delta\lambda} = 15585 \times 10^5 / \sigma^2$, which is almost four times lower than the maximum contrast. The evolution of contrast values as function of spectral bandwidth for this scene is shown in figure 4.11 (red dots). The results of numerical study can be explained by two factors. First, in chapter 3, we observed that an increase in signal to noise ratio enabled by spectral broadening overcame the loss in contrast due to polarization mismatch. In the scene used in this chapter, we can expect the same behavior for the initial broadening of the spectral bandwidth from $\delta\lambda = 10$ nm to $\delta\lambda = 100$ nm : the increase in signal to noise ratio overcomes the loss of contrast due to polarization mismatch. However, this mismatch becomes dominant as we broaden the bandwidth further leading to a global loss of contrast. Secondly, we saw that for this scene the noise model becomes less relevant as the wavelength increases, which can also results in a loss of contrast if we broaden the spectrum and thus integrate higher wavelengths.

4.3.2 Experimental study

We implemented the optimal voltages obtained from numerical study of contrast optimization on the optical bench. Since we did not have tunable bandpass filter in the laboratory to verify the results, we took another approach to solve the problem. For a given spectral range we choose to work at, we implemented on the optical bench the optimal voltages obtained from numerical simulation but changed the spectral filter one after the other, performing experimentally the discretization of equation 4.4 with a step $\delta\lambda = 50$ nm. We were careful to keep total integration time of the experiment to $\tau_0 = 300$ ms. Once we have recorded the polarization images using different spectral filters individually at an optimal voltage configuration, we summed all images in the chosen spectral bandwidth to get a single broadband contrast optimized polarization image. The results of experiment are displayed in figure 4.12 and histograms of images are shown in figure 4.13. The summary of statistical analysis of contrast optimized polarization images recorded is given in table 4.4.

| $\Delta\lambda_R$ (nm) | $\Delta\lambda$ (nm) | $(\theta_{1,opt}^{\Delta\lambda}, \theta_{2,opt}^{\Delta\lambda})$ (V) | $\langle i_t \rangle$ $\times 10^3$ | $\langle i_b \rangle$ $\times 10^3$ | σ_t^2 $\times 10^3$ | σ_b^2 $\times 10^3$ | $C_{\Delta\lambda} (\times \frac{1}{\sigma^2})$ $\times 10^5$ |
|---------------------------|-------------------------|---|--|--|-------------------------------|-------------------------------|--|
| 550 | 10 | 3.80, 3.40, 3.20, 4.00 | 32 | 10 | 45140 | 100 | 4749 |
| 475 - 575 | 100 | 4.20, 3.60, 3.80, 4.20 | 119 | 44 | 412200 | 32230 | 57856 |
| 475 - 625 | 150 | 4.60, 3.60, 3.80, 4.60 | 151 | 95 | 544400 | 265500 | 31969 |
| 425 - 625 | 200 | 2.40, 3.80, 3.60, 2.60 | 125 | 80 | 389710 | 200510 | 21668 |
| 425 - 675 | 250 | 2.40, 3.80, 3.60, 2.60 | 134 | 90 | 433520 | 274850 | 19353 |
| 425 - 725 | 300 | 5.00, 3.60, 4.00, 4.80 | 149 | 110 | 485130 | 383280 | 15264 |

Table 4.4: Statistical analysis of experimental polarization images with increasing spectral bandwidth, $\Delta\lambda$. The $\Delta\lambda_R$, $\langle i_t \rangle$, $\langle i_b \rangle$ represents spectral range, average intensity of target and background, σ_t^2 , σ_b^2 represents intensity variance of target and background respectively.

Discussion

From figure 4.12 and table 4.4, we can see that the maximum contrast for the polarization image is obtained for a spectral bandwidth of $\delta\lambda = 100$ nm centered around 525 nm. This is consistent with the results of the numerical study and the observations of Section 4.2 where the best contrasts for monoband (narrowband) images were obtained between 450 nm and 600 nm.

Then, we can see that the contrast of polarization images decreases as we broaden the spectral bandwidth beyond 100 nm (see figure 4.12(c)-(f), table 4.4 and the blue dots on figure 4.11). As with the

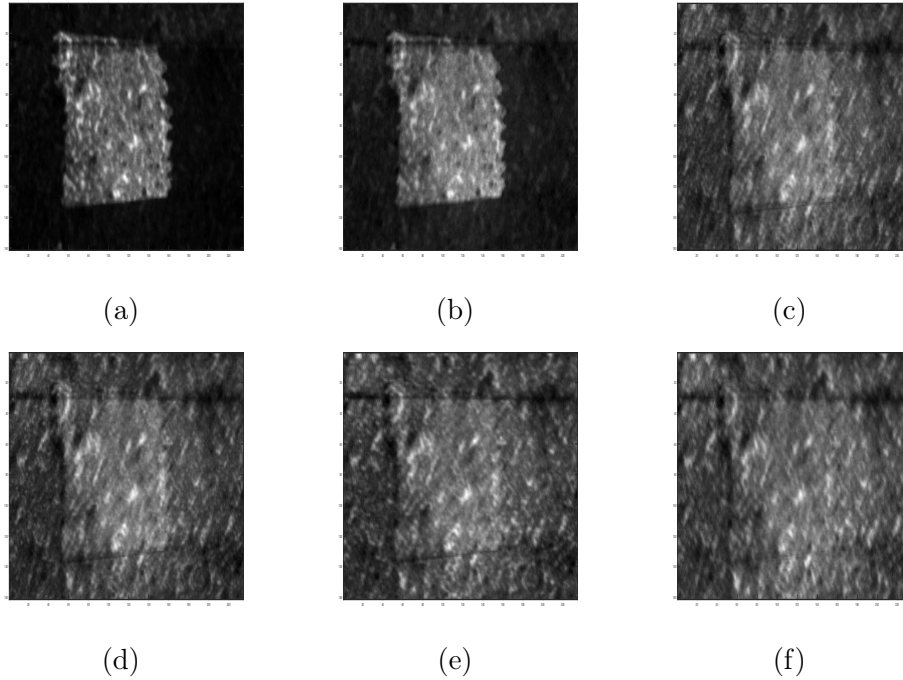


Figure 4.12: Experimental polarization images optimized for maximum contrast at different spectral range, $\Delta\lambda_R$ (and spectral bandwidth, $\Delta\lambda$) (a) 550 nm (10 nm) (b) 475 nm - 575 nm (100 nm) (c) 475 nm - 625 nm (150 nm) (d) 425 nm - 625 nm (200 nm) (e) 425 nm - 675 nm (250 nm) (f) 425 nm - 725 nm (300 nm). Total integration time of camera, $\tau = 300$ ms.

numerical study, it is explained by the fact that the polarization mismatch overcomes the intensity increase due to the spectral broadening and leads to a loss of contrast. We also observe that σ_t^2 and σ_b^2 of polarization image for spectral bandwidths beyond 100 nm increase and have a negative impact in the contrast of polarization image, as shown on the histograms 4.13(c)-(f).

Moreover, we can see on figure 4.11 that the experimental data follow closely the numerical predictions, showing that the physical modeling of contrast optimization problem is correct.

Finally, we have to highlight that the contrast optimization process by numerical simulation takes ~ 18 minutes on a classical desktop computer. The excess time on optical bench is due to camera integration time (~ 5 ms), LCVR response time (~ 150 ms) and finally the speed of computer processor which controls the optical bench. On the other hand, the exhaustive search used in Chapter 3 and performed using the same equipment takes ~ 180 minutes, ten times longer. Therefore, using the prior knowledge of the multispectral Mueller matrices allows to improve the efficiency of our optimization procedure.

4.4 Conclusion

Contrast optimization of polarization images in narrow band as well as broadband spectrum can be conducted efficiently even with chromatic optical components. This is achieved by the calibration of LCVRs in PSG/PSA for multispectral use. Using this method, the time to execute the optimization process is only $(1/10)^{th}$ of the time for exhaustive search thanks to prior determination of the multispectral Mueller matrices. We proved once again that spectral bandwidth can be used as a contrast optimization parameter in polarimetric imaging. The prior determination of multispectral Mueller matrices gives us a new insight to the contrast optimization problem and knowledge of it can be used to determine the right

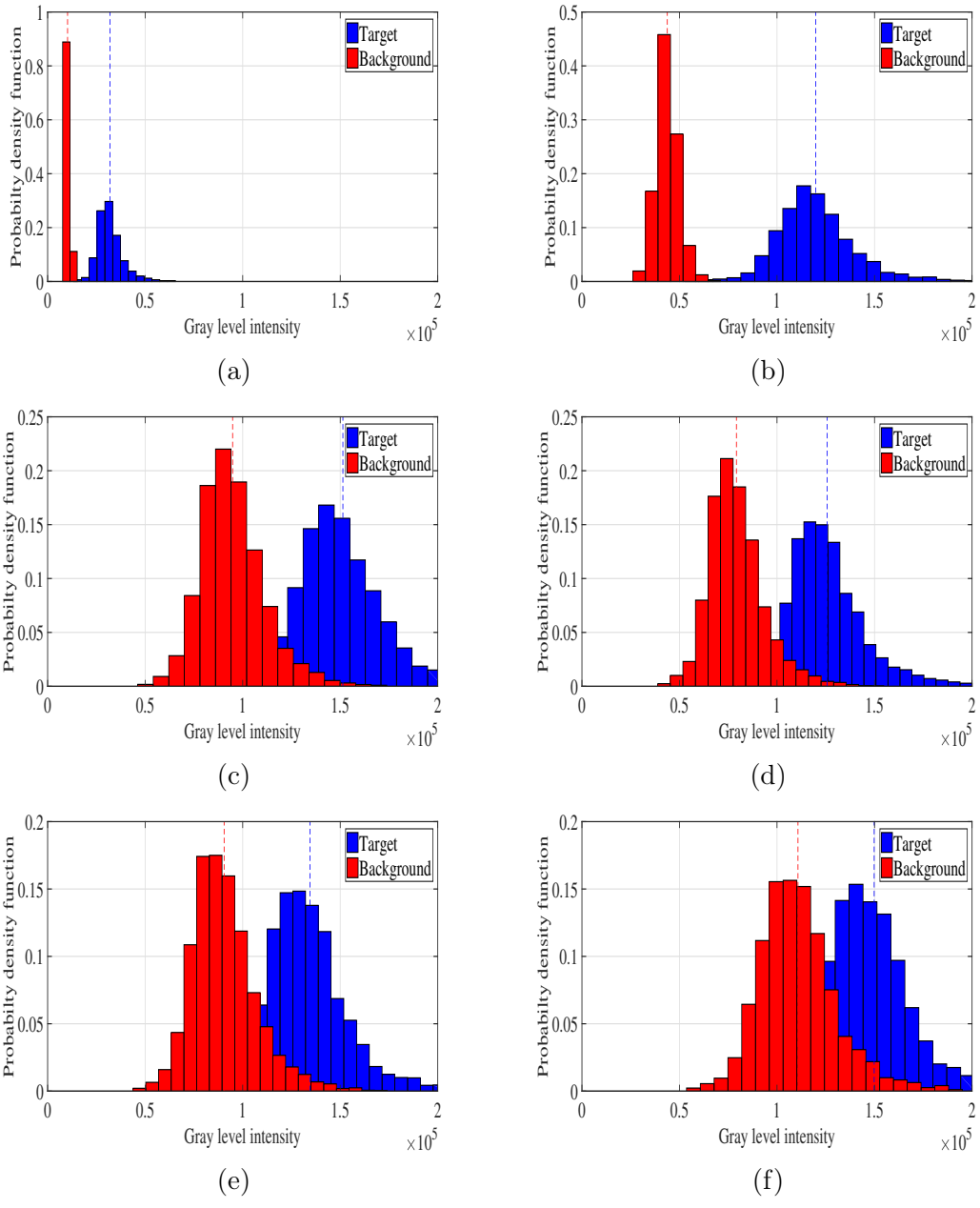


Figure 4.13: Histograms of images shown in figure 4.12(a) 550 nm (10 nm) (b) 475 nm - 575 nm (100 nm) (c) 475 nm - 625 nm (150 nm) (d) 425 nm - 625 nm (200 nm) (e) 425 nm - 675 nm (250 nm) (f) 425 nm - 725 nm (300 nm).

spectral range one should work to get the polarization image with maximum contrast.

It is observed that the intensity variance of target/background regions are not negligible and it often diminishes visual contrast. This phenomenon of high intensity variance is due to the spatially varying properties of Mueller matrix in the target/background regions in the scene. The contrast expression defined for present use is not optimal to tackle this phenomenon. The contrast can be further enhanced if we model a contrast expression which takes into account the spatially varying Mueller matrix problem [41]. This is an interesting perspective for future work.

Chapter 5

Polarization based differential phase contrast imaging

5.1 Introduction

We saw in the previous chapters, the efficiency of active polarization imagers in detecting objects otherwise hidden from standard intensity imaging devices. The objective of work done in this chapter is to apply the techniques of polarimetric imaging to another domain and to an industrial environment, namely, to improve the performance of a LED-based differential phase contrast microscopy (DPC) setup. This work done was done in collaboration with a corporate research team of Carl Zeiss, Jena (Germany) for a period of three months to build a fully automatized prototype. The standard microscopy setup was provided by the corporate research team to incorporate the polarization optics needed to accomplish the task. I explain the motivation behind the development of this novel imaging scheme in following paragraphs.

Phase contrast microscopy is an optical microscopy technique to image transparent biological sample. Imaging a biological sample requires converting its varying optical thickness into varying intensity in the image plane. In case of bright-field microscopy, the amplitude variations of transmitted light induced by a sample as a result of differential absorption is translated into image intensity. Therefore, in the absence of any differential absorption as in the case of a transparent sample, bright-field imaging provides an image with almost zero contrast. In such cases, researchers stain their sample in order to introduce varying absorptions and thus to improve the contrast in the image plane. However, this procedure kills biological sample quickly and adds spurious details, it is therefore not suitable for live imaging.

In 1942, F.Zernike invented a method to increase phase contrast of such sample by introducing a phase delay on zeroth order diffraction at the pupil plane [42]. This was the first successful microscopic method which could enhance the image contrast of transparent sample by introducing a linear relation between phase gradient and intensity in image plane but these images were affected by diffraction halo and phase artifact.

In 1952, Georges Nomarski introduced differential interference contrast (DIC) microscopy which works on the principle of interferometry to gain information about phase of the sample [43]. This technique was useful to emphasize lines and edges of sample without producing any bright diffraction halo (phase artifact) as in the case of phase contrast microscopy. However, in DIC method, the image is a complex mixture of amplitude and phase gradient which makes it necessary to have phase shift to separate phase information from amplitude. Linear measurement of phase gradient along two orthogonal directions enables retrieval of 2D phase distribution.

In 1984, Hammilton *et al.* published a new method to measure pure differential phase contrast (DPC) of a sample in scanning optical microscopy using split detector [44]. This method uses a laser beam to

scan through the sample and the phase gradient in the object deflects the transmitted beam so that half of the detector has larger output than the other. For weak phase gradient, the intensity difference of half detectors is proportional to the phase gradient.

In 1985, for the first time, Kachar *et al.* demonstrated the power of oblique illumination in the improvement of phase contrast of transparent sample [45]. In oblique illumination, direct light from the condenser light cone is restricted to a single azimuth, interacting with the sample from single direction rather than illuminating it with an even distribution of light through a well defined numerical aperture. The major consequence of oblique illumination is to shift the zeroth order of light (undiffracted light) passing through the sample from the center to one peripheral side of the objective front lens element. This shift of the zeroth order of light to one side allows one or more higher orders of the diffracted light to be included at the rear focal plane of the objective and thus contribute to the image formation.

In 2009, S.B.Mehta and Colin J.R. Sheppard demonstrated asymmetric illumination based differential phase contrast imaging [46]. This method does not require any phase shifting for quantitative imaging of phase gradient and provides artifact-free images of birefringent samples. Inspired by this work, Zheng *et al.* in 2011 published a seminal work which introduced the idea of programmable LED array as a replacement to condenser in transmitted light compound microscopes [47]. This was followed by the development of asymmetric illumination based phase contrast microscopic setups which could generate multi axis DPC images [48, 49].

However, DPC imaging by asymmetric illumination requires a minimum of two images recorded and illuminated at opposite angles. This process requires more time and intermittent flashes of light make observation inconvenient. We study in this chapter, the possibility of removing these undesirable characteristics of DPC imaging by using polarimetric imaging technique. Our objective is to create single shot polarization based DPC imaging technique. This study is inspired by a recent work of Lei Tian and Laura Waller in which quantitative differential phase contrast is achieved using LED array microscope [49].

5.2 Polarization based differential phase contrast imaging using LED illumination

In this section, we first discuss about the concept of LED array illumination as a replacement to condenser lens in microscope, then about differential phase contrast imaging by asymmetric illumination and finally polarization based differential phase contrast imaging.

5.2.1 LED array illumination

Appropriate illumination of sample is necessary for high image resolution and quality image formation. Standard Köhler illumination is the widely used illumination scheme to provide uniform illumination and glare free images. With the advent of modern LED technology, a new scheme of illumination with LED array has been put forward by Zheng *et al.*, which can replace condenser in microscopes. This type of illumination is cost effective, able to create different illumination patterns and thus useful for different type of imaging modalities [47].

To understand the principle of LED illumination scheme, consider the figure 5.1(a) in which one LED belonging to a (16×16) LED array is lit. Let us denote its location by coordinates (x_i, y_i) . The location of the LED array centre is denoted by (x_c, y_c) . Assuming that the sample is located at distance 'Q' (at the z direction) from the LED array, the local numerical aperture (NA) of this LED is defined as

$$\text{NA}(x_i, y_i) = \frac{r}{\sqrt{r^2 + Q^2}} \quad (5.1)$$

where $r = \sqrt{(x_i - x_c)^2 + (y_i - y_c)^2}$.

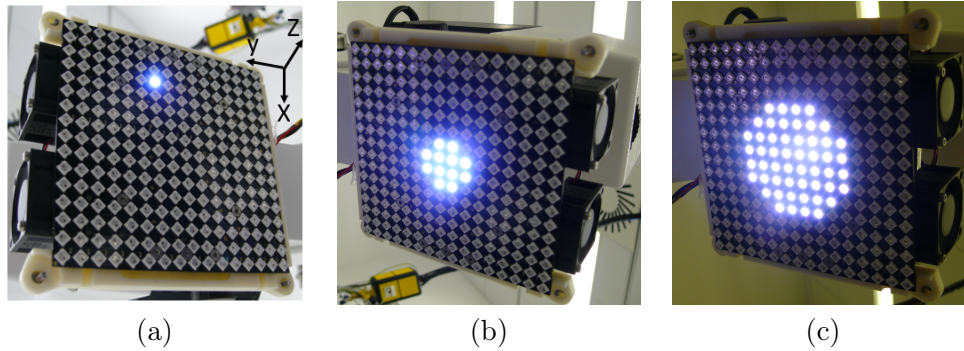


Figure 5.1: LED array (16x16) is a cost effective, programmable illumination source used in optical microscopy. It is controlled by Arduino, a micro controller based kit for building up digital devices and interactive objects. (a) single LED is lit for illumination (b) LEDs illuminated to have NA = 0.16 (c) LEDs illuminated to have NA = 0.30.

In microscopic bright-field imaging, we match the illumination NA to the collection NA of the objective lens. Such a matching procedure is classically performed by adjusting the size of the condenser diaphragm in the Köhler illumination setup. Equation 5.1 provides the NA of each individual LEDs in the illumination. Let us separate LEDs in to two groups:

- Group A : local NA > collection NA
- Group B : local NA < collection NA.

In order to achieve bright-field imaging with LED illumination, we simply turn off Group A LEDs and turn on Group B LEDs.

5.2.2 Differential phase contrast imaging using LEDs

Differential phase contrast imaging works on the principle that phase gradient of a sample can be extracted from two images, illuminated and recorded at opposite illumination angles. For illustration, let us consider an illumination scheme composed of programmable LED array as explained in [47] and shown in figure 5.2. We first illuminate the sample with only left half of circular pattern (left angular illumination), record the image of sample represented as I_L , followed by illumination of only right half of circular pattern (right angular illumination) and record the second image, I_R . The DPC image is then defined as the normalized difference between these two images [48] :

$$I_{DPC} = \frac{I_L - I_R}{I_L + I_R}. \quad (5.2)$$

A schematic diagram of differential phase contrast imaging setup using LED illumination is shown in figure 5.3 and the principle of DPC imaging is given in figure 5.4. Figure 5.4(a) and 5.4(b) represent images recorded using left and right angular illumination respectively. The images recorded by angular illumination exhibit better contrast in comparison to bright-field image. In angular illumination, direct light from the LED array light cone is restricted to a single azimuth, interacting with the sample from a particular direction rather than illuminating it with an even distribution of light through a well defined numerical aperture. The major effect of angular illumination is to shift the zeroth order of light (undiffracted light) passing through the sample from the center to one peripheral side of the objective front



Figure 5.2: LED array illumination scheme. The optical condenser is replaced by a programmable LED array. The figure shows a circular illumination pattern.

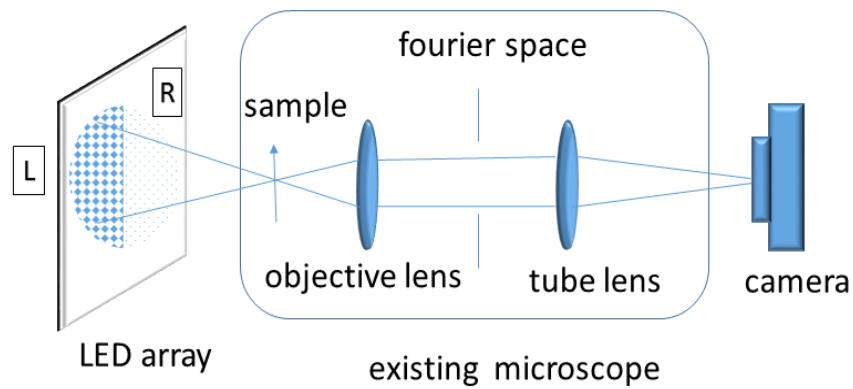


Figure 5.3: Schematic representation of differential phase contrast imaging. LED array microscope places a programmable source sufficiently far from the sample such that source is in Fourier space. In the figure, left half of semicircular array L is switched on and the right array R is switched off.

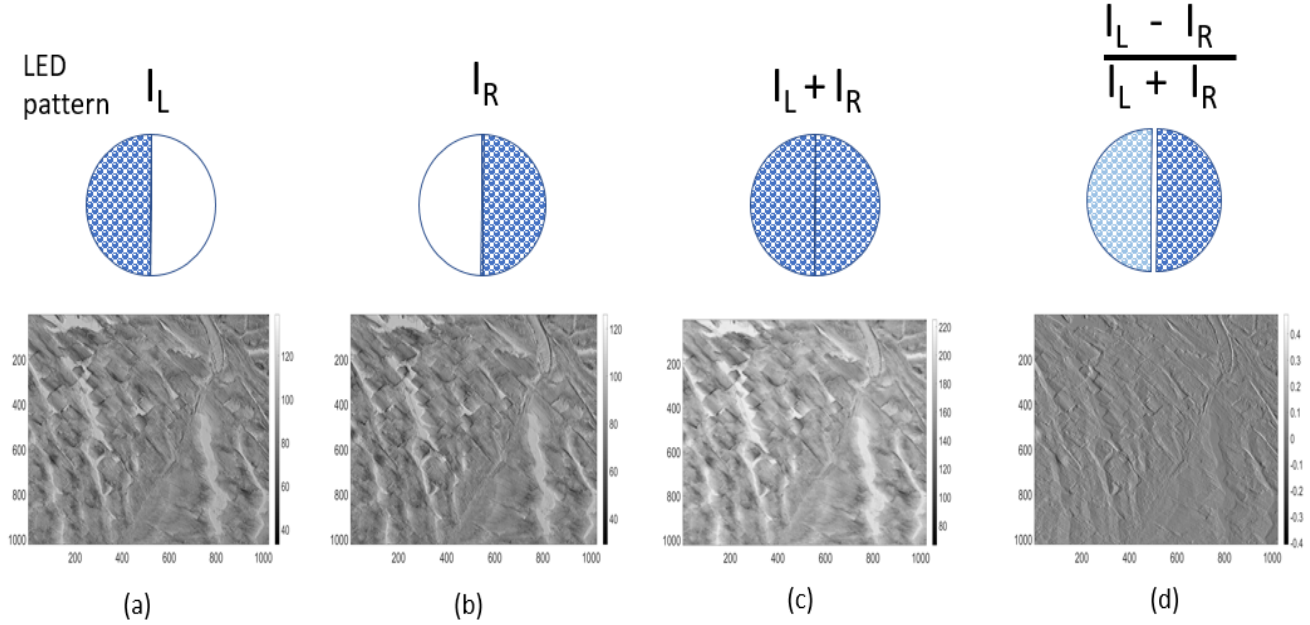


Figure 5.4: Principle of DPC imaging. (a) image formed by left angular illumination (b) image formed by right angular illumination (c) bright-field image (d) DPC image.

lens element of microscope. This shift of zeroth order of light to one side allows one or more higher orders of the diffracted light to be included at the rear focal plane of the objective and thus contributes to the image formation.

Figure 5.4(c) shows bright-field image of the sample which displays poor contrast compared to figure 5.4(a) and figure 5.4(b). The reason can be explained as follows. Bright-field imaging measures the intensity variations induced by the sample as light passes through it and it is insensitive to phase gradient induced by the sample. In case of transparent sample, there is hardly any absorption and therefore the intensity scattered by such samples have constant amplitude. Figure 5.4(d) shows differential phase contrast image of the sample. It shows fine features of the sample. The edges of fine elements in the sample are distinct from each other. This result can be explained as follows. Assume that a thin amplitude object (purely real object) is at the focus of a microscope and is illuminated from opposite illumination angles one after the other, the intensity of the recorded images (I_L and I_R) will be equal since a purely real object has a symmetric Fourier transform. Therefore, as per equation 5.2, DPC image of the amplitude object will have null contrast. In case of a phase object, the local phase gradient changes the propagation direction of illuminating light, thus the normalized difference between I_L and I_R is directly dependent on phase gradient of the sample along the axis of asymmetry. Subtraction of I_R from I_L ensure removal of background light.

However, DPC imaging procedure consumes more time than standard bright-field imaging because it involves intermittent oblique lighting and the recording of two images one after the other, and this feature is not desirable for live imaging. One potential solution is to increase the speed of data transfer rate in the camera. At present, this is limited by the availability of cameras with required data transfer rate. Moreover, the continuous intermittent flashes of light during observation may also cause inconvenience for user.

5.2.3 LED based polarization differential phase contrast imaging

We propose a solution to the aforementioned problems. The solution is to use polarization optics in the illumination as well as in the detection path of an existing LED array microscopy setup. Two polarization foils with polarization axes in orthogonal directions are placed side by side just below the LED illumination as shown in figure 5.5. I switch on full circle of illumination (bright-field illumination), the orthogonal eigen polarization states of light created by the two polarization foils still encode left and right angular illumination with them. The light from left and right angular illumination will not interfere with each other because they have orthogonal eigen polarization states. Thus, we are able to create angular illumination without switching on/off LEDs.



Figure 5.5: Polarization foil used for creating polarized illumination. It is attached with LED array in the experimental set up. Left rectangular portion of foil generates vertical polarized light while the right rectangular foil generates horizontal polarized light

On the detector side, we place a polarization sensitive camera. The pixels of the camera are sensitive to orthogonal states of polarization. The figure 5.6 shows the proposed scheme of imaging. The polarization sensitive pixels corresponding to vertical/horizontal polarization are distributed like checkerboard pattern. The light beams from left and right angular illumination interact with the sample and reach the polarization camera. We record the image of the sample and in a single shot, we get access to sample information carried by left and right angular beams. The information which belongs to vertical and horizontal polarized pixels are separated out into two sets and missing data is generated by interpolation technique in respective images. This is similar to debayering process in colour camera.

Let us denote the image created by left angular illumination encoded with vertical polarization as after interpolation as (I_{LV}) and the image formed by right angular illumination encoded with horizontal polarization after interpolation as (I_{RH}) . Then polarization based differential phase contrast (PDPC) is computed as

$$I_{PDPC} = \frac{I_{LV} - I_{RH}}{I_{LV} + I_{RH}}. \quad (5.3)$$

The principle of PDPC imaging is shown in figure 5.7. Figure 5.7(a) and figure 5.7(b) shows the images recorded using left angular illumination encoded with vertically polarized light and right angular illumination with horizontally polarized light respectively. Figure 5.7(c) displays the bright-field image of the sample. Figure 5.7(d) shows PDPC image of the sample. In the following section, we will compare performance between the DPC and the PDPC imaging.

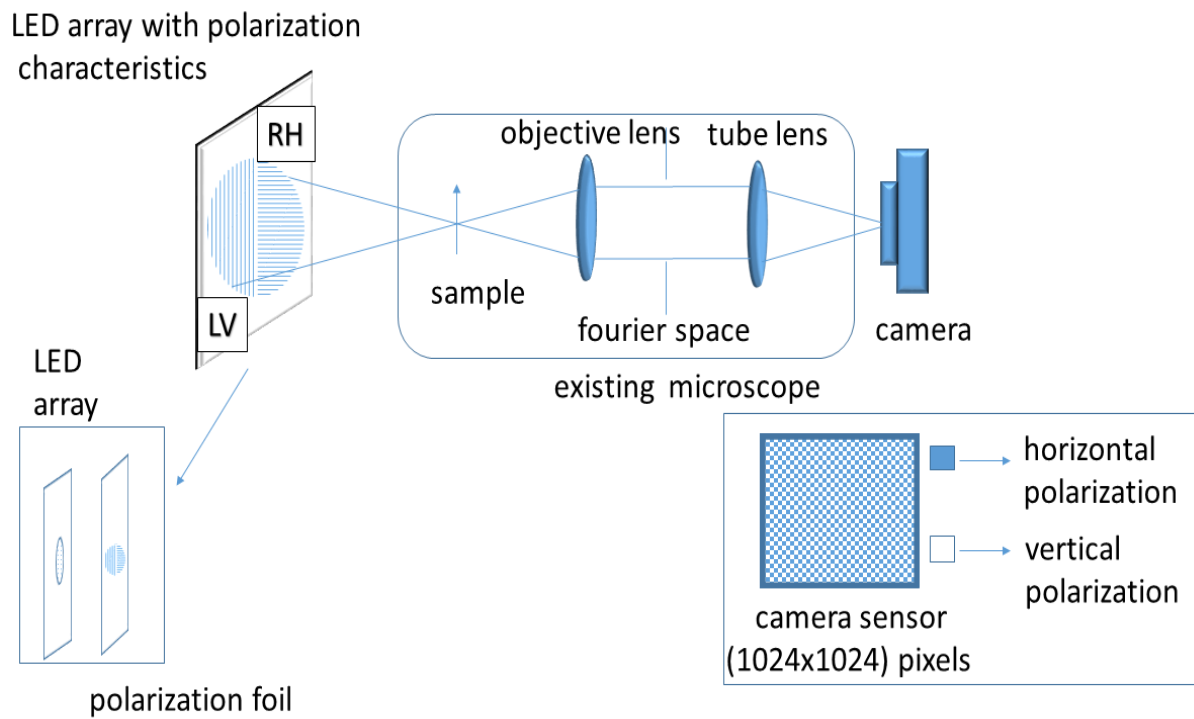


Figure 5.6: Proposed scheme to record polarization based differential phase contrast of a sample. LV and RH denotes left illumination encoded with vertical polarization and right illumination encoded with horizontal polarization respectively. Both LV and RH illuminate sample simultaneously such that we have bright-field illumination. Camera (CCD) is polarization sensitive. Pixels which are sensitive to horizontal/vertical polarization are placed like checkerboard pattern in the camera.

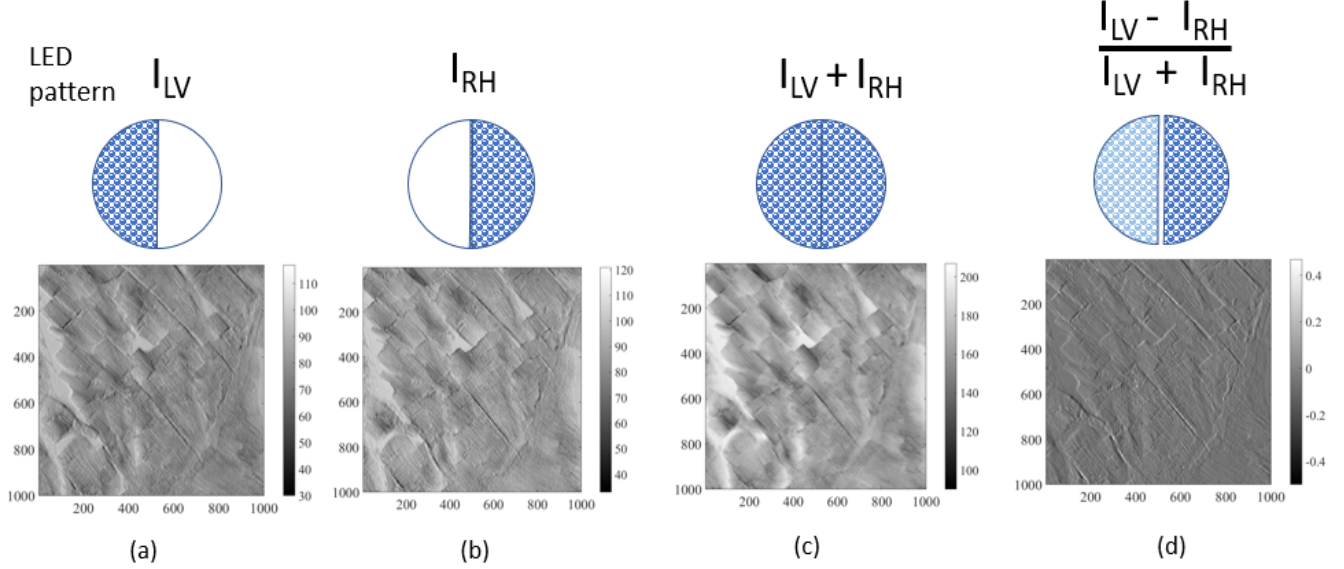


Figure 5.7: Principle of PDPC imaging. (a) image formed by left angular illumination coded with vertical polarization (b) image formed by right angular illumination coded with horizontal polarization (c) bright-field image (d) PDPC image.

5.3 Experimental study of PDPC imaging

The proposed PDPC imaging scheme shown in figure 5.6 requires a polarization sensitive camera for detecting polarized light. But this was not available and therefore we devised a new experimental scheme to simulate proposed PDPC imaging setup. In this section, we present the experimental scheme implemented to simulate proposed PDPC imaging. Then we conduct a comparative study of performance between DPC and PDPC imaging using the results.

5.3.1 Experimental scheme to simulate proposed PDPC imaging scheme

The LED array is covered by two separate polarization foils placed side by side with their polarization axes orthogonal to each other. In order to have bright-field imaging, the numerical aperture of illumination is matched with that of the microscope objective. The light produced by the LED array is focused on to sample plane which interacts with transparent sample. The diffracted and undiffracted light waves from sample plane are collected by the microscope objective and focused on to camera sensor by tube lens (see figure 5.8).

In order to generate PDPC images, we require a polarization sensitive camera in the experimental scheme as shown in figure 5.6. Since the polarization sensitive camera was not available, we devised a new experimental scheme (see figure 5.8). It is as follows. We introduce a turret in the infinity space of existing microscope and it has two analyzers with their polarization axes in orthogonal direction (see figure 5.9). By rotating the turret, we record I_{LV} and I_{RH} sequentially. Switching from one analyzer position to other takes less than a second and movement is motorized.

In order to simulate the generation and extraction of PDPC images as in the proposed polarization sensitive camera, we removed the information from odd number pixels in I_{LV} (1024x1024) and from even number pixels in I_{RH} (1024x1024). Then, we retrieved the lost information by standard interpolation

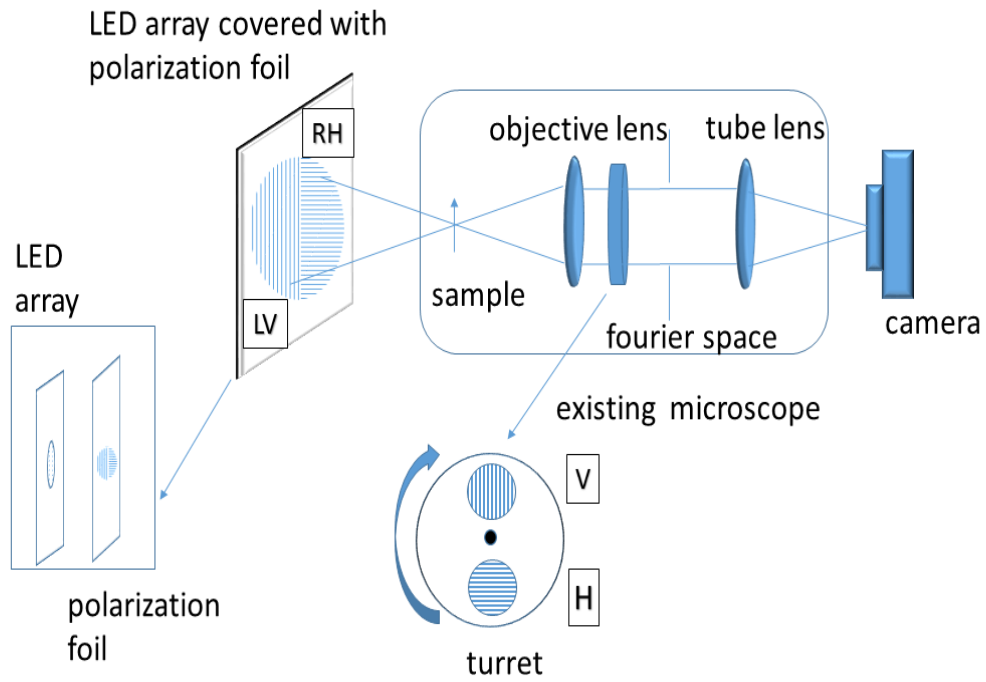


Figure 5.8: Experimental setup to simulate the proposed scheme (see figure 5.6) due to non availability of polarization sensitive camera. The difference in the set up is a motorized filter turret, which allows one to switch between two orthogonal oriented analyzers and a standard camera (Camera model: Ximea XiQ MQ042MG-CM, pixel size of sensor is $5.50\mu m$).

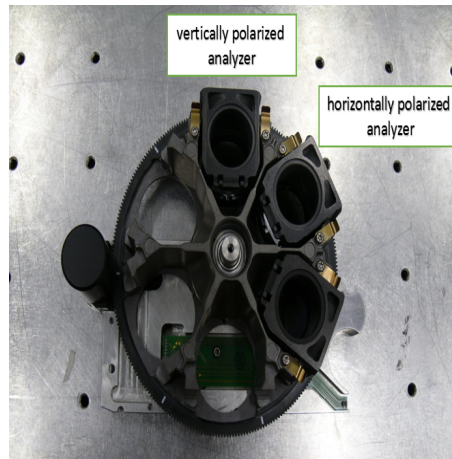


Figure 5.9: Turret used in the new scheme of experimental setup. Switching slot between analyzers take less than a second and the process is automated.

techniques and thus PDPC image is computed. The above procedure is known as debayering. In our project, we call these images as debayered PDPC images. The whole procedure of recording and generation of PDPC image is automatized.

5.3.2 Determination of polarizer extinction ratio

LED array can produce green, red, blue and white (mixture of above three) illumination. Our microscopic imaging set up contains two polarizer sheets to generate orthogonally polarized illumination and two analyzers to detect polarized light transmitted through the sample. In order to check the quality of polarizer and analyzer, we define polarizer extinction ratio (PER). The polarization extinction ratio is defined as the ratio of power transmitted by the device when the polarization axes are aligned compared with the condition when the axes are crossed. Mathematically it can be expressed as,

$$\text{PER} = 10 \log_{10}(I_{\parallel}/I_{\perp}), \quad (5.4)$$

where I_{\parallel} and I_{\perp} are the average intensity of image when polarizer- analyzer axes are parallel and perpendicular respectively. The PER is measured in the unit of decibels (dB). For a perfect system with no cross talk the PER value is infinite.

| Color | I_{\parallel} | I_{\perp} | PER (dB) |
|-------|-----------------|-------------|----------|
| Green | 67.86 | 10.13 | 8.23 |
| Red | 89.69 | 12.42 | 8.58 |
| Blue | 51.48 | 8.92 | 7.61 |
| White | 124.18 | 16.86 | 8.67 |

Table 5.1: The above measurements are carried out on same imaging conditions(NA of illumination = NA of objective). Calculated intensity values are average values over a region in image.

I conducted an experiment to check PER for different color illumination. The results are given below in table 5.1. From the table it is found that no particular advantage is offered by any particular color illumination. Therefore, I have decided to use white illumination throughout my experiment.

5.3.3 Results, analysis and discussion

In this section, we are going to analyze and compare the performance of three type of images : (a) DPC image (b) PDPC image (image we obtain by the implementation of experimental scheme as explained in Section 5.3) (c) debayered PDPC image (image we obtain after the application of debayering on PDPC image). The debayered DPC image is how an original PDPC image would look like. In order to do this study, I selected two semi-transparent biological samples for inspection : (a) a thin section ($15\mu m$ thick) of a small fish which is fixed and embedded on a glass plate (b) an unknown birefringent histological sample ($2\mu m$ thick). We have recorded DPC, PDPC and debayered PDPC images of first sample for three different configurations of microscope objectives ($5 \times/0.16$, $10 \times/0.30$, $20 \times/0.50$). Then we recorded three types of images of second sample for one type of objective configuration ($10 \times/0.30$). We have maintained the NA condition (as explained in Section 5.2.1) required to attain bright-field imaging in all cases.

I recorded DPC image first, then proceeded to record PDPC image and finally debayered PDPC image is generated from PDPC image. For the analysis of three types of images, I plotted line profiles and histograms of them and made a comparative study. I noticed that there is a pixel shift [$(\delta \text{ row}, \delta \text{ column} =$

(-2,-9)] between the images (I_{LV} , I_{RH}) when we switch between the analyzers (shown in figure 5.9). This was due to imperfect plane parallel surfaces of the analyzers used inside turret. We digitally corrected this offset by standard image processing tools.

The DPC, PDPC and debayered PDPC images of first sample are shown in figure 5.10. A small area of the sample is magnified and shown in the figure 5.10(d), figure 5.10(e) and figure 5.10(f). Their histograms and line profiles are shown in figure 5.11. The three types of images have similar line profiles and histograms. A close observation of line profiles of DPC image and PDPC image (see figure 5.11(a)), and DPC image and debayered PDPC image will show that there is a small fluctuations in intensity distribution between them. They are due to the limited polarization extinction ratio of polarizers used in the setup, which gives rise to cross talk. The debayered PDPC image (figure 5.10(c)) has loss of resolution compared PDPC image (figure 5.10(b)) because debayered PDPC image is formed from PDPC image after debayering process.

I repeated same experiments for the same sample with other microscope objectives ($10 \times/0.30$, $20 \times/0.50$). It is to be noted that we are not looking at the same part of sample anymore in these images. Their results are shown in figure 5.12, figure 5.13, figure 5.14 and figure 5.15. We conclude with similar observations in these two cases also. This shows that DPC imaging can be successfully replaced by PDPC imaging for the similar samples.

Now, we are going to see how PDPC imaging performs in comparison to DPC imaging with respect to the second sample (birefringent histological sample). The microscope objective used for the observation was $10 \times/0.30$. The images are shown in figure 5.16 and their analysis is shown in figure 5.17. As we compare DPC image (figure 5.16(a)) with PDPC image (figure 5.16(b)) and debayered PDPC image (figure 5.16(c)), we observe that they are not similar. We notice some white patches in case of PDPC and debayered PDPC images but absent in the DPC image. For the close observation of this white patch, see figures 5.16(d), 5.16(e) and 5.16(f). The histograms and line profiles of DPC image, PDPC image and debayered PDPC image shows the difference in intensity distribution between DPC and PDPC images. The reason is as follows. Here the sample is a birefringent histological sample ($2\mu m$ thick). It interacts and modifies incoming optical beam's polarization state. The analyzer in PDPC setup is sensitive to change in polarization state of light. Therefore, PDPC imaging is sensitive to birefringent sample whereas DPC imaging scheme is not. Therefore, we conclude that PDPC imaging with present architecture is not suitable for the observation of birefringent samples.

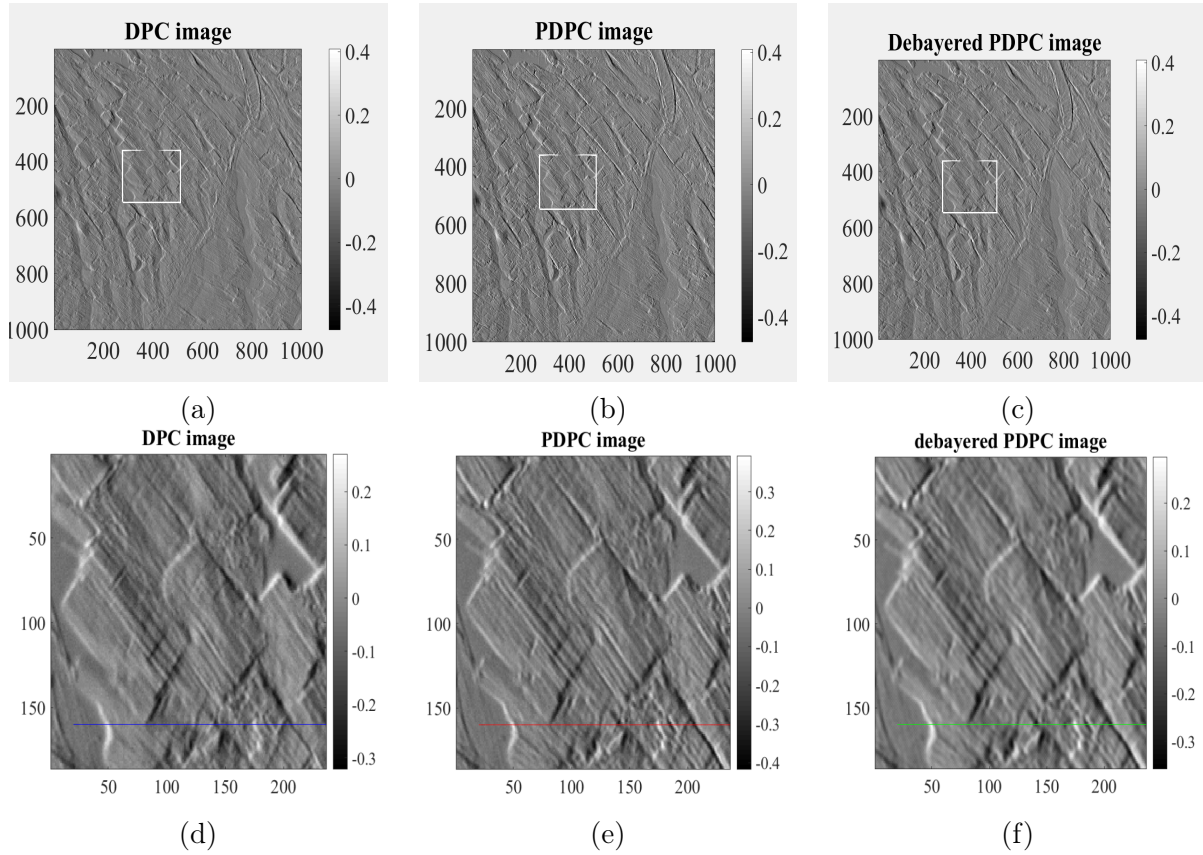


Figure 5.10: Comparison of DPC, PDPC and debayered PDPC images of a thin section (15μ thick) of small fish which is fixed and embedded on a glass plate (NA of microscope = $5 \times / 0.16$) (a) DPC image (b) PDPC image (c) debayered PDPC image (d) zoomed image of region bounded by white square in figure 5.10(a) (e) zoomed image of figure 5.10(b) (f) zoomed image of figure 5.10(c).

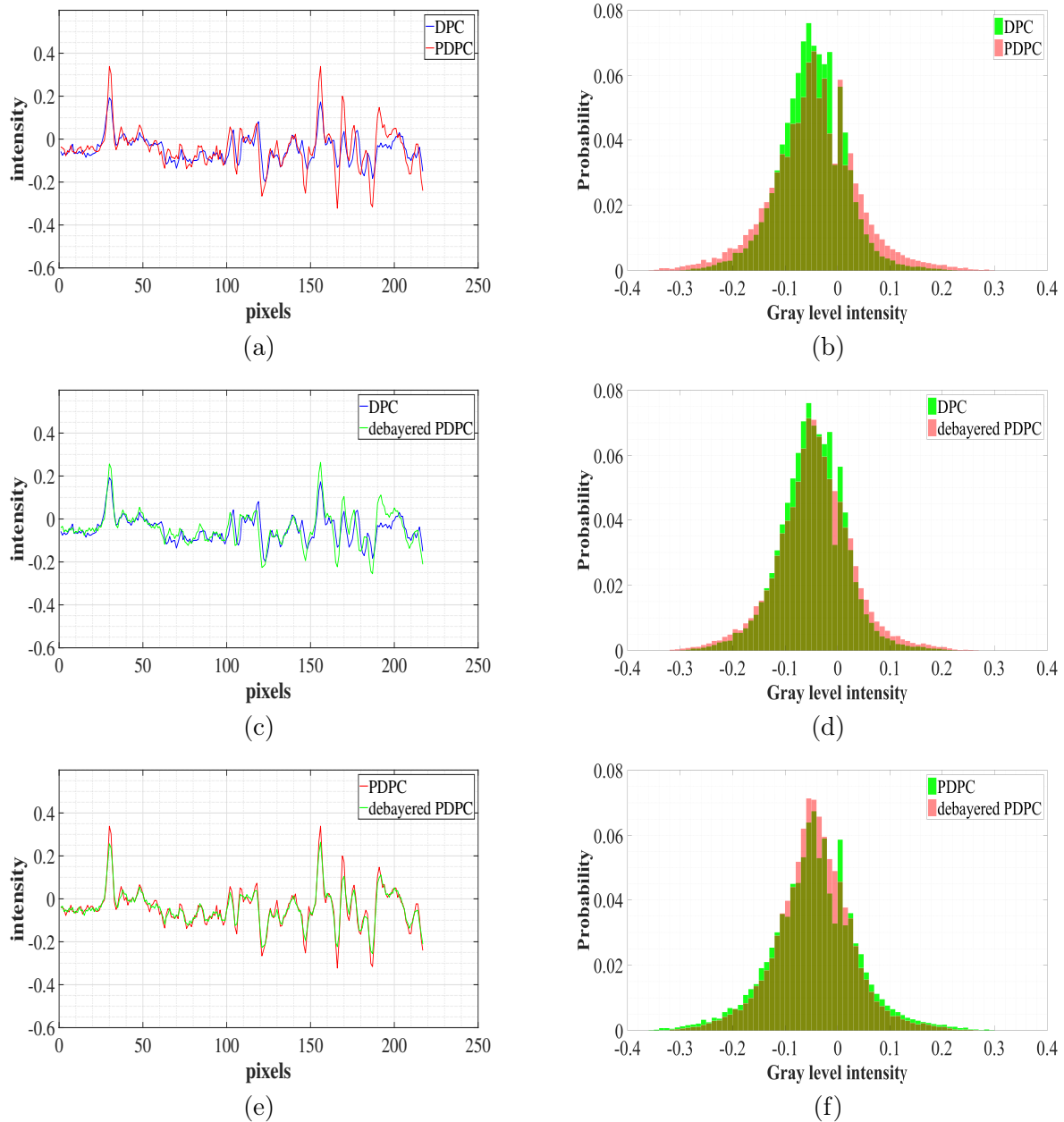


Figure 5.11: Analysis of images shown in figure 5.10: (a) line profiles of DPC and PDPC images shown in figure 5.10(d). (b) histograms of DPC and PDPC images shown in figure 5.10(d). (c) line profiles of DPC and debayered PDPC images shown in figure 5.10(e). (d) histograms of DPC and debayered PDPC images shown in figure 5.10(e). (e) line profiles of PDPC and debayered PDPC images shown in figure 5.10(f). (f) histograms of PDPC and debayered PDPC images shown in figure 5.10(f).

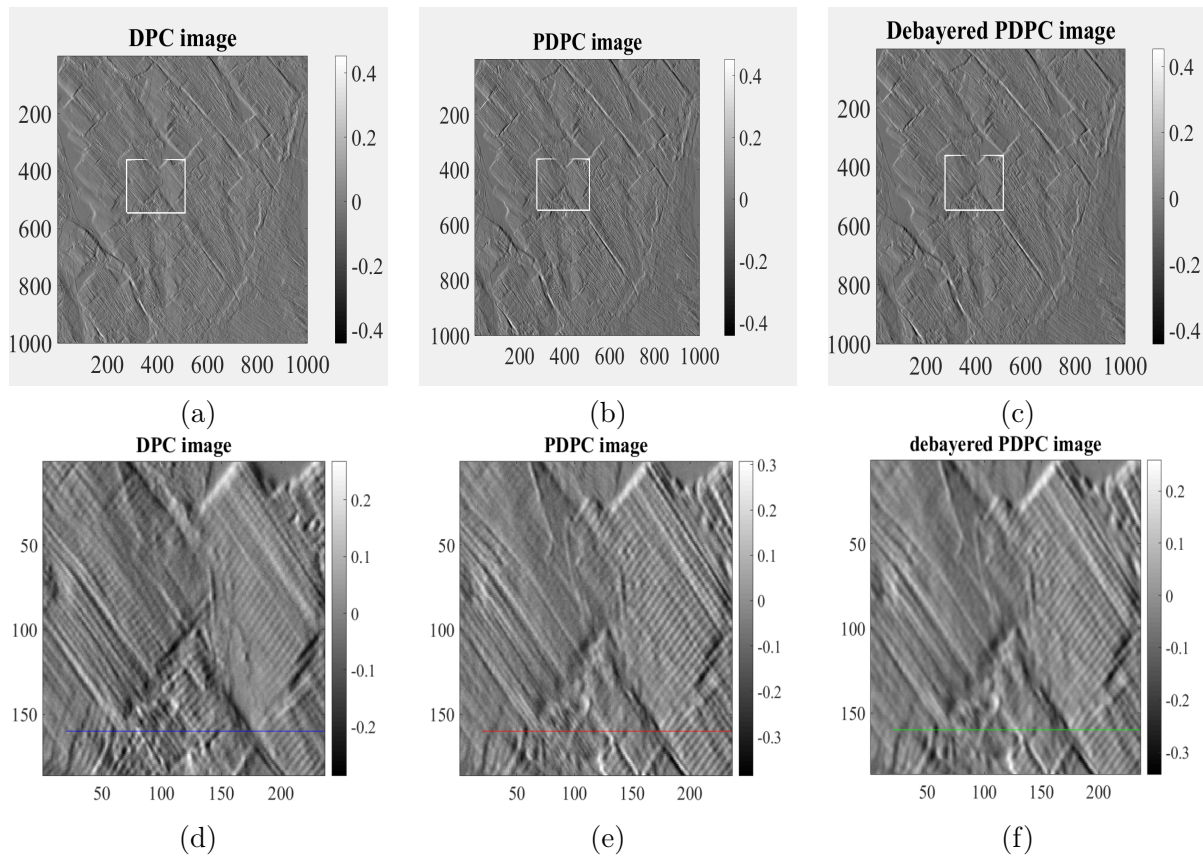


Figure 5.12: Comparison of DPC, PDPC and debayered PDPC images of a thin section (15μ thick) of small fish which is fixed and embedded on a glass plate (NA of microscope objective = $10\times/0.30$) (a) DPC image (b) PDPC image (c) debayered PDPC image (d) zoomed image of region bounded by white square in figure 5.12(a) (e) zoomed image of figure 5.12(b) (f) zoomed image of figure 5.12(c).

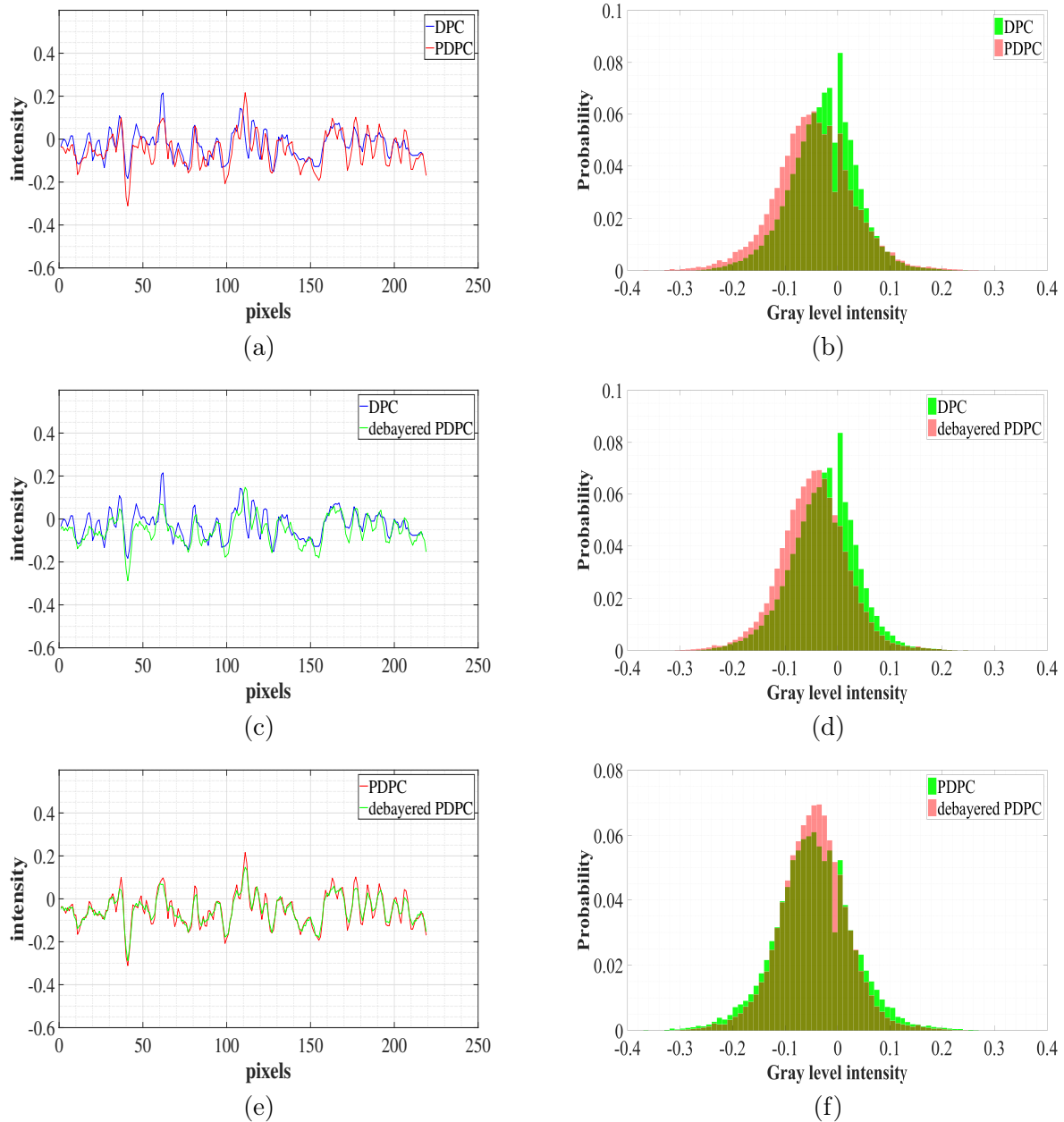


Figure 5.13: Analysis of images shown in figure 5.12: (a) line profiles of DPC and PDPC images shown in figure 5.12(d). (b) histograms of DPC and PDPC images shown in figure 5.12(d). (c) line profiles of DPC and debayered PDPC images shown in figure 5.12(e). (d) histograms of DPC and debayered PDPC images shown in figure 5.12(e). (e) line profiles of PDPC and debayered PDPC images shown in figure 5.12(f). (f) histograms of PDPC and debayered PDPC images shown in figure 5.12(f).

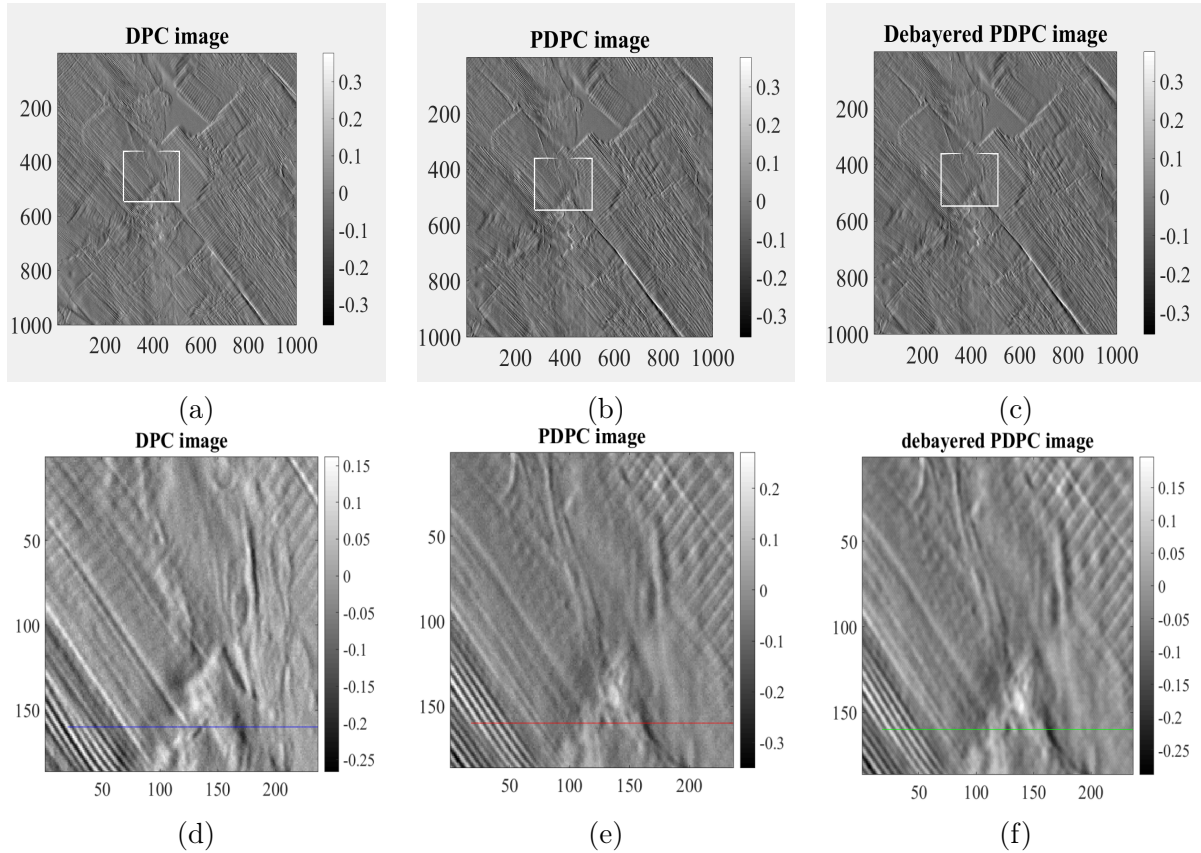


Figure 5.14: Comparison of DPC, PDPC and debayered PDPC images of a thin section (15μ thick) of small fish which is fixed and embedded on a glass plate (NA of microscope objective = $20\times/0.50$) (a) DPC image (b) PDPC image (c) debayered PDPC image (d) zoomed image of region bounded by white square in figure 5.14(a) (e) zoomed image of figure 5.14(b) (f) zoomed image of figure 5.14(c).

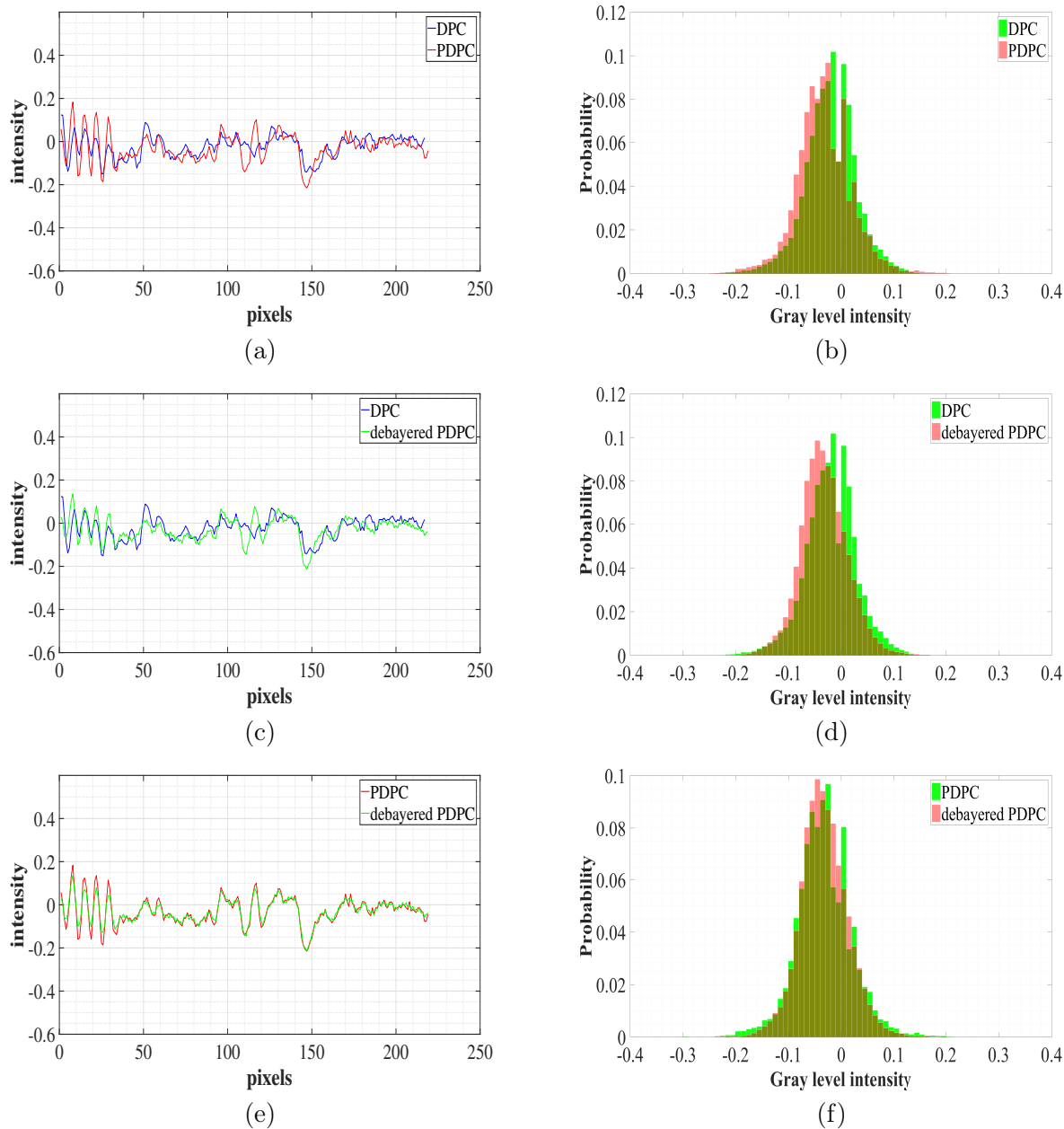


Figure 5.15: Analysis of images shown in figure 5.14: (a) line profiles of DPC and PDPC images shown in figure 5.14(d). (b) histograms of DPC and PDPC images shown in figure 5.14(d). (c) line profiles of DPC and debayered PDPC images shown in figure 5.14(e). (d) histograms of DPC and debayered PDPC images shown in figure 5.14(e). (e) line profiles of PDPC and debayered PDPC images shown in figure 5.14(f). (f) histograms of PDPC and debayered PDPC images shown in figure 5.14(f).

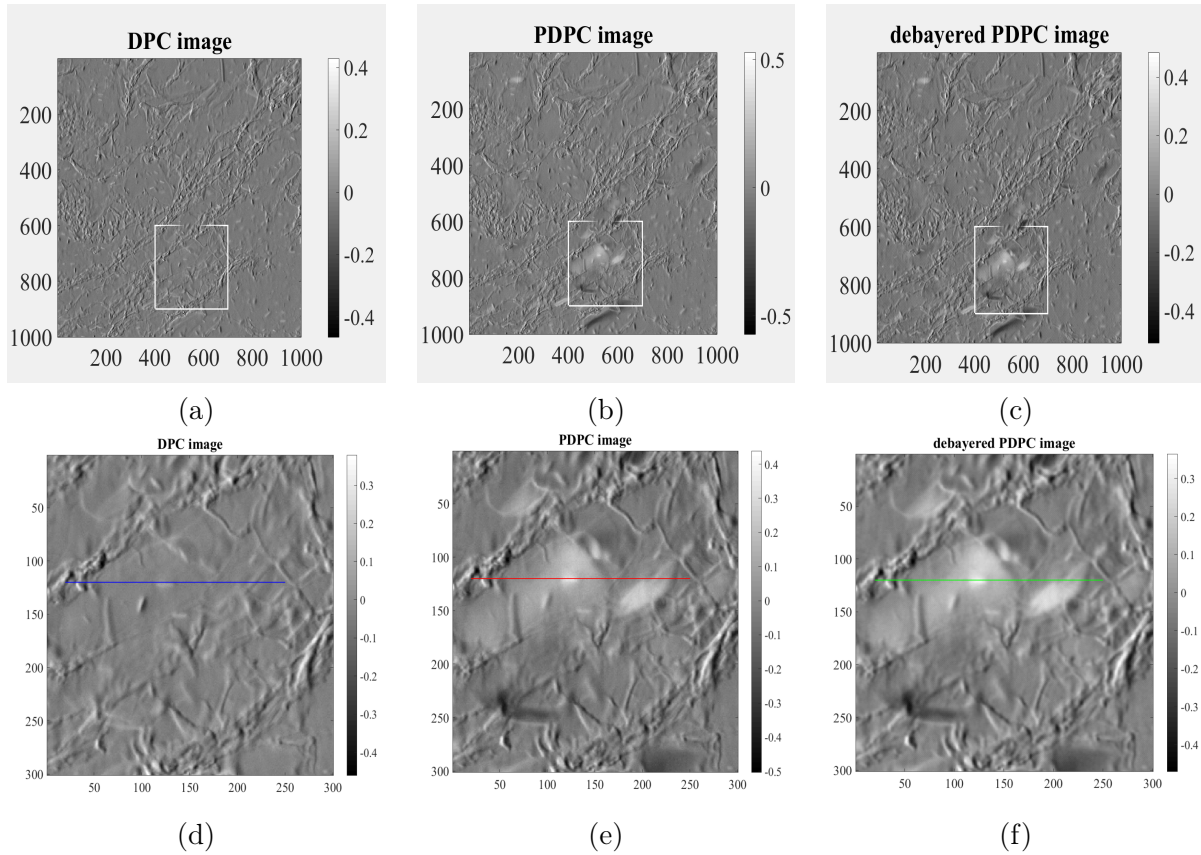


Figure 5.16: Comparison of DPC, PDPC and debayered PDPC images of a birefringent histological sample, $2\mu\text{m}$ thick (NA of microscope objective = $10\times/0.30$) (a) DPC image (b) PDPC image (c) debayered PDPC image (d) zoomed image of region bounded by white square of figure 5.16(a) (e) zoomed image of figure 5.16(b) (f) zoomed image of figure 5.16(c).

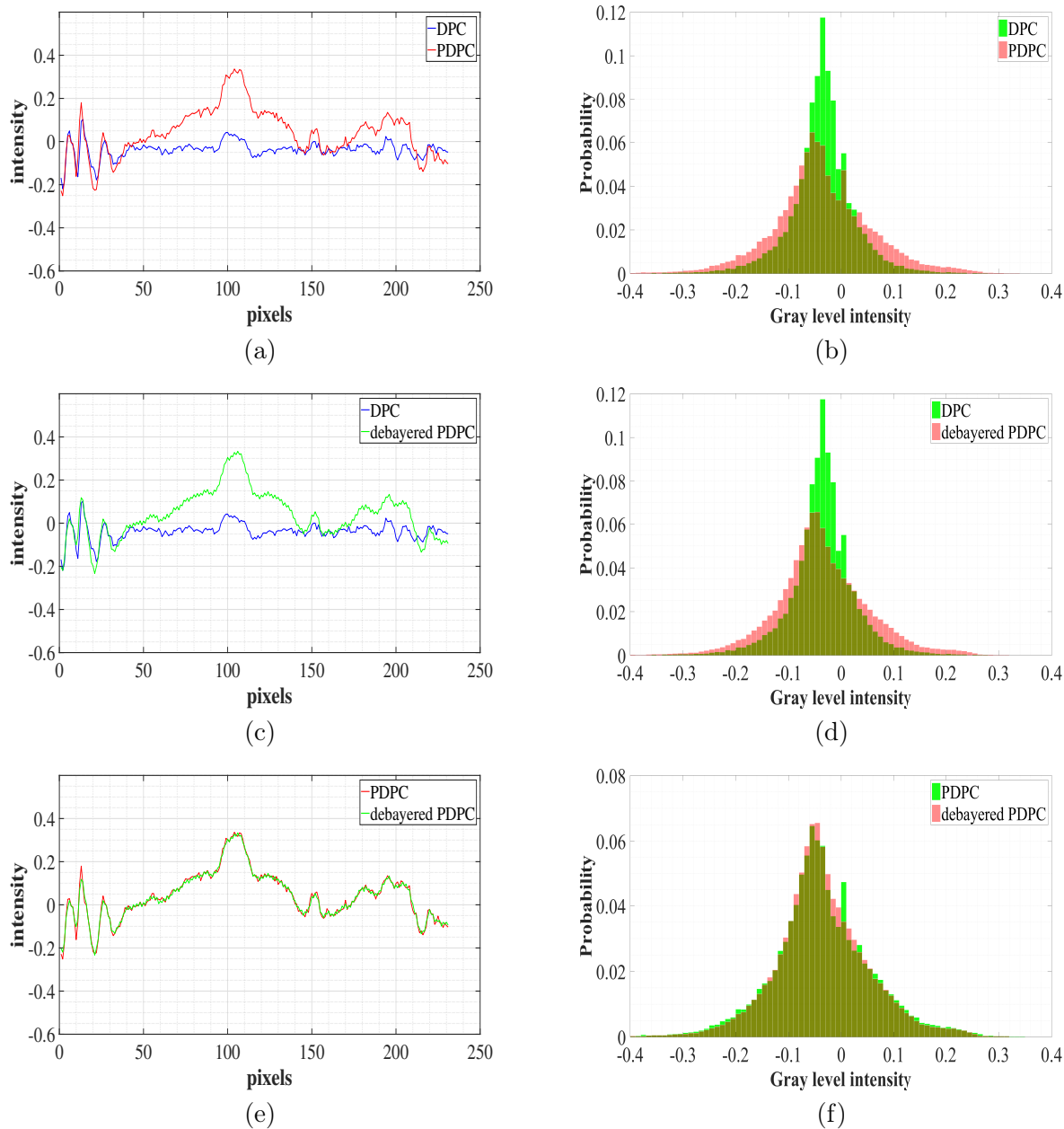


Figure 5.17: Analysis of images shown in figure 5.16: (a) line profiles of DPC and PDPC images shown in figure 5.16(d). (b) histograms of DPC and PDPC images shown in figure 5.16(d). (c) line profiles of DPC and debayered PDPC images shown in figure 5.16(e). (d) histograms of DPC and debayered PDPC images shown in figure 5.16(e). (e) line profiles of PDPC and debayered PDPC images shown in figure 5.16(f). (f) histograms of PDPC and debayered PDPC images shown in figure 5.16(f).

5.4 Conclusion

Our goal has been to replace intermittent oblique lighting with dual-polarization illumination in a phase contrast microscopy setup. We have shown that this new technique, called PDPC, gives results very similar to classical DPC technique while potentially requiring only one image acquisition and removing the need of inconvenient intermittent illumination. Only small fluctuations of intensity distribution between DPC and PDPC images were observed. They are due to the limited polarization extinction ratio of polarizers used in the setup, which gives rise to cross talk. This can be solved by using higher quality polarization foils.

In the actual PDPC setup, a pixellated polarimetric camera will be used to separate the two illumination polarization, and will thus require interpolation of the missing pixels for each polarization. We simulated this interpolation process and showed that it has only limited impact on the quality of PDPC images.

Since the PDPC imaging modality requires only one snapshot to determine differential phase contrast, it is faster and allows bright-field imaging, avoiding inconvenience due to intermittent flash of light. The main limit of the proposed PDPC imaging setup is that in its present form, it is not suitable for observing birefringent samples, since the polarimetric properties of the sample interact with those of the polarized illumination. Consequently, the main perspective of the present work is to build a PDPC imaging setup which can measure both the global dephasing of the sample and its birefringence properties. It would also be interesting to study how the loss of resolution in PDPC imaging as a result of the interpolation process can be reduced.

General conclusions

Summary

The primary objective of this thesis was to answer this simple question "What happens if one removes the spectral filter in front of an active polarimetric imager?" We addressed this issue in the context of target detection, where the criterion to optimize is not the precision of polarization measurements, but the contrast between a target of interest and the background. It is clear that that if the optical components are chromatic, the polarimetric precision will be reduced by removing the spectral filter, but the increase of photon flux will contribute to increase the signal to noise ratio. My purpose was to study whether the resultant of these two antagonist effects leads to an increase or a decrease of the contrast.

Using numerical simulations, I first showed that in target detection scenarios featuring ideal birefringent and diattenuating components, the global balance of these two effects is positive: the increase of photon flux largely overcomes the loss of polarimetric precision. Moreover, I demonstrated that because of their chromatic properties, the optimum settings of the polarization state generator (PSG) and of the polarization state analyzer (PSA) are wavelength dependent. Thus, by taking into account the illumination bandwidth and in the optimization of the settings of PSG and PSA, it is possible to further increase the contrast compared to an optimization at a given wavelength. I have checked these theoretical results on a real experiment performed with an active polarimetric imager available in the laboratory. Removing the spectral filter lead to a significant increase of the contrast, or, which is equivalent, to a significant reduction of the integration time necessary to obtain a good image. Moreover, I checked that the contrast could be further enhanced by taking into account the scene polarization properties' spectral dependence and the optical system in the contrast optimization process.

This optimization was done with an exhaustive search procedure on optical bench, which gives accurate result but is very time consuming. In order to accelerate this process, it is preferable to perform it numerically. For that purpose, the spectral response of the PSA and PSG have to be known as well as the spectral variations of the Mueller matrix of the scene. I thus calibrated the PSA and the PSG spectral characteristics using a reference instrument, and measured the spectral Mueller matrix of a real scene featuring different types of birefringent materials. This enabled me to perform numerical optimization of the contrast in this scene. I compared the outcome of this numerical optimization with the results of the exhaustive search on the bench and found them very similar. The notable achievement of this work is the reduction of time $(1/10)^{th}$ to compute optimal configuration of PSG/PSA for maximum contrast for a given scene and a given spectral bandwidth. Moreover, knowing a spectral numerical model of the scene made it possible to interpret more deeply the optimization results.

Indeed, I considered different spectral bandwidth, and I discovered that on this scene, the increase in bandwidth did not necessarily improve the contrast of the polarization image: there exists an optimal value of the spectral bandwidth that realizes the optimal trade-off between increase of the photon flux and loss of polarimetric precision. The position and the width of the optimal spectral band can be easily interpreted from the measured multispectral Mueller matrices of the scene. As a conclusion, the bandwidth of illumination can be considered as a new parameter to optimize the contrast in active polarimetric

imagers.

The second objective of this thesis work was to apply the techniques of polarimetric imagers to another domain and to an industrial environment, namely, to improve the performance of a LED-based differential phase contrast microscopy (DPC) setup. Standard DPC set up requires the acquisition of two images, and the intermittent flashes of LED light while imaging causes inconvenience to the user. The polarization optics installed in the illumination and detection path of microscopic setup could remove the intermittent flash and reduced the time needed for imaging to half, since a single acquisition is now needed. I experimentally demonstrated that this new type of imaging called "polarization based differential phase contrast" (PDPC) microscopy provides images of quality similar to standard DPC imaging for most biological samples other than birefringent ones.

Perspectives

This thesis work has many perspectives. First, it has to be understood that the contrast criterion used in this manuscript is based on the hypothesis that the dominant noise that perturbs the acquisitions is additive and Gaussian. This hypothesis may not be fulfilled in some types of images. Optimization criteria adapted to Poisson noise [50], speckle noise [50] or correlated and spatially varying noise [41] have been proposed and have been found relevant for certain types of images in the context of narrow band active polarimetric imagers. It is of course very attractive to generalize them to the wideband case. However, since they are more complex to parametrize and to compute, new problems of optimization will appear.

A second axis of potential development is to consider the multi-spectral case. For scenes where the contrast varies rapidly with the wavelength, measurement of the polarimetric image in different wavebands can provide more discriminant information than broadband imaging. In this case, one has to jointly optimize the number and central wavelength of the bands, but also their widths. To solve this multi-parameter optimization problem, the techniques we have developed for single bandwidth optimization will be useful.

Finally, concerning the work on differential phase contrast microscopy, I showed that PDPC imaging was successful to generate images with quality similar to standard DPC imaging for most biological samples. However it could not perform effectively in case of birefringent samples. Therefore, it would be interesting to design a PDPC imaging setup which is able to measure simultaneously the global phase information, that is the usual output of DPC, and the birefringent properties of a sample, which can be very useful, for example, in biological applications.

Résumé de la thèse

Les systèmes d'imagerie polarimétrique permettent de révéler des contrastes invisibles à l'œil humain et aux capteurs d'imagerie classiques, car ces derniers sont insensibles à l'état de polarisation de la lumière. Les imageurs polarimétriques ont montré leur intérêt dans différents domaines d'application tels que la télédétection, l'inspection industrielle ou l'imagerie biomédicale.

Ces systèmes se répartissent en deux catégories: les systèmes passifs et les systèmes actifs. Dans les systèmes d'imagerie polarimétrique passive, la source d'illumination de la scène est la lumière naturelle. Comme cette lumière est dépolarisée, ces systèmes peuvent seulement mesurer la manière dont les différents éléments de la scène repolarisent la lumière incidente. Bien que ces systèmes aient montré leur intérêt, en particulier dans les applications de télédétection à longue distance, ils ne tirent parti que d'un aspect très partiel des propriétés polarimétriques de la scène. A l'inverse, dans les systèmes d'imagerie polarimétriques actifs, on contrôle à la fois l'état de polarisation de la source d'illumination et la manière dont l'état de polarisation de la lumière diffusée par la scène est analysé. Ils permettent donc de tirer parti de toutes les propriétés polarimétriques de la scène, représentées par la matrice de Mueller de chaque pixel de l'image.

Un système d'imagerie polarimétrique actif est organisé de la manière suivante (Figure 5.18). La source de lumière est contrôlée par un générateur d'état de polarisation (PSG) qui peut générer un état de polarisation quelconque sur la sphère de Poincaré. Cet état de polarisation est représenté par le vecteur de Stokes \mathbf{S} . Il illumine un point de la scène de matrice de Mueller M_{\bullet} , et la lumière diffusée par la scène a donc l'état de polarisation $M_{\bullet}\mathbf{S}$. Cette lumière est utilisée pour former une image de la scène, mais avant d'être mesurée par le détecteur, elle est analysée par un composant appelé "analyseur d'état de polarisation" (PSA) qui projette l'état de polarisation de la lumière incidente sur un état représenté par le vecteur de Stokes \mathbf{T} . L'intensité de la lumière atteignant chaque pixel du détecteur est donc:

$$I_{\bullet} \propto \frac{I_0}{2} \mathbf{T}^T M_{\bullet} \mathbf{S}. \quad (5.5)$$

C'est ainsi qu'est mesurée l'image polarimétrique active d'une scène.

Dans l'imageur utilisé lors de cette thèse, le PSG et le PSA sont réalisés à partir de matrices de cristaux liquides contrôlées électriquement appelées LCVR. Comme ces cellules introduisent un déphasage différentiel sur leurs deux axes propres, leur effet sur la polarisation est très dépendant de la longueur d'onde. En d'autres termes, ils sont très chromatiques. C'est pourquoi on interpose en général un filtre spectral à bande étroite (typiquement 10 nm) devant le capteur d'image. Si la source d'illumination est à large spectre, cela a pour effet de réduire de manière très importante le flux de photons participant à la formation de l'image et donc de réduire le rapport signal à bruit de manière significative.

Le premier objectif de ce travail de thèse a été d'étudier ce qui se passe lorsqu'on retire ce filtre. Dans cette analyse, on a pris en compte le fait que l'objectif n'est pas de réaliser une mesure précise de l'état de polarisation, mais simplement de faire apparaître un contraste entre deux régions de la scène. Dans la seconde partie de la thèse, nous avons appliqué des techniques polarimétriques à la simplification des mesures de contraste de phase en microscopie.

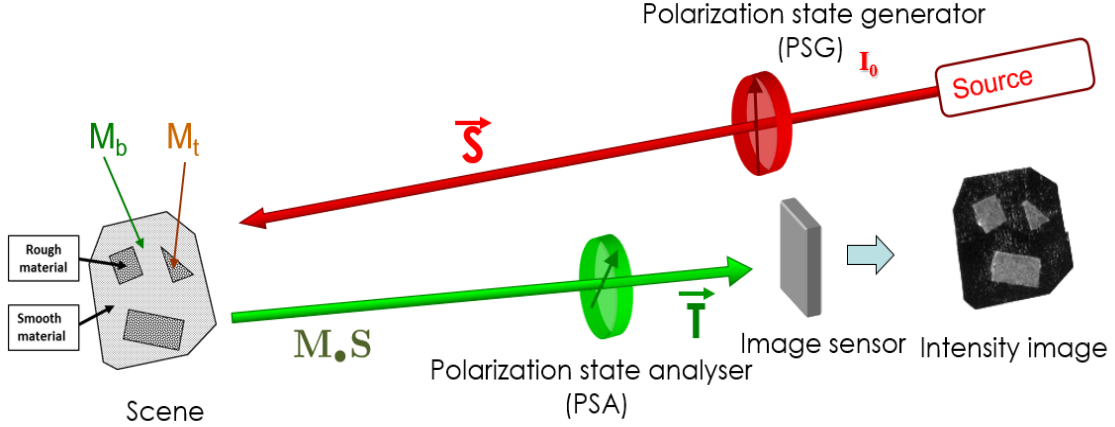


Figure 5.18: Schéma de principe d'un imageur polarimétrique actif.

Principe de l'optimisation du contraste polarimétrique adaptatif en lumière à spectre large

Définissons tout d'abord l'expression du contraste entre deux zones d'une image obtenue par un imageur polarimétrique actif en présence d'une illumination à spectre étroit.

Les propriétés de polarisation de la scène ainsi que celles des éléments optiques des PSG et PSA dépendent de la longueur d'onde d'illumination λ . Les vecteurs de Stokes générés/analysés par le PSG/PSA peuvent donc être écrits de la manière suivante:

$$\mathbf{S} = \begin{bmatrix} 1 \\ \mathbf{s}_{\theta_1}(\lambda) \end{bmatrix}, \mathbf{T} = \begin{bmatrix} 1 \\ \mathbf{t}_{\theta_2}(\lambda) \end{bmatrix} \quad (5.6)$$

où \mathbf{s}_{θ_1} et \mathbf{t}_{θ_2} représentent les vecteurs de Stokes réduits, de dimension 3 et de norme unité, du PSG et du PSA respectivement. Dans les expressions \mathbf{s}_{θ_1} et \mathbf{t}_{θ_2} , $\{\theta_1, \theta_2\}$ représente l'ensemble des tensions qui permettent de contrôler les LCVR (il y en a 4 pour le PSG et 4 pour le PSA). D'autre part, on peut modéliser la matrice de Mueller d'un point de la scène de la manière suivante:

$$\mathbf{M}_{\bullet} = \begin{bmatrix} \mathbf{M}_{0,\bullet}(\lambda) & \mathbf{m}_{\bullet}^T(\lambda) \\ \mathbf{n}_{\bullet}(\lambda) & \tilde{\mathbf{M}}_{\bullet}(\lambda) \end{bmatrix} \quad (5.7)$$

où $\mathbf{M}_{0,\bullet}(\lambda)$ représente le premier élément, $\mathbf{m}(\lambda)$ et $\mathbf{n}(\lambda)$ deux vecteurs à 3 dimensions de norme 1, $\tilde{\mathbf{M}}$ une matrice 3×3 et T correspond à la transposition de matrices. On suppose que l'objet à détecter possède une matrice de Mueller M_t et le fond une matrice M_b . On peut montrer que le contraste entre la cible et le fond dans l'image issue de l'imageur polarimétrique actif a l'expression suivante:

$$C_{\lambda}(\theta_1, \theta_2) = \frac{\tau^2}{32\sigma^2} \rho^2(\lambda) \left[\Delta M_0(\lambda) + \Delta \mathbf{m}^T(\lambda) \mathbf{s}_{\theta_1}(\lambda) + \mathbf{t}_{\theta_2}^T(\lambda) (\Delta \mathbf{n}(\lambda) + \mathbf{D}(\lambda) \mathbf{s}_{\theta_1}(\lambda)) \right]^2, \quad (5.8)$$

où τ est le temps d'exposition du capteur, $\rho(\lambda)$ son efficacité quantique, $I_0(\lambda)$ l'intensité de l'illumination, σ^2 la variance du bruit supposé additif et gaussien, et

$$\begin{aligned} \Delta M_0(\lambda) &= M_{0,t}(\lambda) - M_{0,b}(\lambda), & \Delta \mathbf{m}(\lambda) &= \mathbf{m}_t(\lambda) - \mathbf{m}_b(\lambda) \\ \Delta \mathbf{n}(\lambda) &= \mathbf{n}_t(\lambda) - \mathbf{n}_b(\lambda), & \mathbf{D}(\lambda) &= \tilde{\mathbf{M}}_t(\lambda) - \tilde{\mathbf{M}}_b(\lambda) \end{aligned} \quad (5.9)$$

| Paramètres | Scene |
|------------|------------------------------|
| α_t | 135° |
| α_b | 150° |
| A_t | 90° × 550/360° |
| A_b | 300° × 550/360° |
| d_t | [0, -0.75, 0] ^T |
| d_b | [0.37, 0.65, 0] ^T |

Table 5.2: Paramètres définissant la scène utilisée dans les simulations.

Pour rendre cette équation plus lisible, définissons

$$\begin{aligned}\chi_{\theta_1}(\lambda) &= \Delta M_0(\lambda) + \Delta \mathbf{m}^T(\lambda) \mathbf{s}_{\theta_1}(\lambda) \\ \mathbf{u}_{\theta_1}(\lambda) &= \Delta \mathbf{n}(\lambda) + \mathbf{D}(\lambda) \mathbf{s}_{\theta_1}(\lambda)\end{aligned}\quad (5.10)$$

L'expression du contraste prend donc la forme simplifiées suivante:

$$C_\lambda(\theta_1, \theta_2) = \frac{\tau^2}{32\sigma^2} \rho^2(\lambda) \left[\chi_{\theta_1}(\lambda) + \mathbf{t}_{\theta_2}^T(\lambda) \mathbf{u}_{\theta_1}(\lambda) \right]^2. \quad (5.11)$$

Les tensions θ_1 et θ_2 du PSA et du PSG peuvent être optimisées de manière à maximiser cette valeur du contraste. Cependant, les états optimaux obtenus dépendent de la longueur d'onde de travail λ . Or le fait d'ajouter un filtre spectral devant une source de lumière à large spectre pour sélectionner la valeur de λ réduit drastiquement le nombre de photons pénétrant dans le système. Une solution consiste donc à retirer le filtre, et à étudier comment évolue le contraste.

En présence d'un illumination à large spectre, l'expression du contraste est simplement une intégrale de l'équation (5.11) sur les longueurs d'onde, ce qui donne:

$$C_{\Delta\lambda}(\theta_1, \theta_2) = \frac{\tau^2}{32\sigma^2} \left(\int_{\Delta\lambda} \rho(\lambda) \left[\chi_{\theta_1}(\lambda) + \mathbf{t}_{\theta_2}^T(\lambda) \mathbf{u}_{\theta_1}(\lambda) \right] d\lambda \right)^2, \quad (5.12)$$

où $\Delta\lambda$ est la largeur spectrale du système. Ce contraste est potentiellement plus important puisqu'on intègre sur un spectre plus large, mais le système est affecté d'une "aberration polarimétrique" puisque le PSA et le PSG sont chromatiques, ce qui doit conduire à une baisse du contraste. L'objectif est donc d'étudier, dans différentes configurations, le résultat du compromis entre ces deux effets antagonistes.

Optimisation du contraste polarimétrique dans une scène idéale

Nous avons tout d'abord procédé à une étude numérique. Nous avons considéré pour cela une scène où la cible et le fond sont tous deux composés de retardateurs et de diatténuateurs. Leurs matrices de Mueller peuvent être représentées par $\mathbf{M}_\bullet = \mathbf{R}(\phi_\bullet^\lambda, \alpha_\bullet) \mathbf{P}(\mathbf{d}_\bullet)$ où $\mathbf{R}(\phi_\bullet^\lambda, \alpha_\bullet)$ représente la matrice de Mueller d'un retardateur avec une orientation α_\bullet , un déphasage $\phi_\bullet^\lambda = 2\pi A_\bullet / \lambda$ où A_\bullet est une constante, et $\mathbf{P}(\mathbf{d}_\bullet)$ est la matrice de Mueller d'un diatténuateur pur où \mathbf{d}_\bullet le vecteur de diatténuation, qui décrit à la fois l'amplitude et l'axe de diatténuation. Ce vecteur est différent pour les deux régions (cf. tableau 5.2).

Considérons tout d'abord le cas où un filtre spectral étroit centré sur 550 nm est utilisé dans le système d'imagerie. Dans ce cas, on peut déterminer les valeurs de θ_1 et θ_2 qui maximisent le contraste. La figure 5.19 (b) montre la valeur du contraste $C_\lambda(\theta_1, \theta_{2,\text{opt}}^\lambda)$ à $\lambda = 550$ nm.

J'ai également tracé sur la figure 5.19 la même courbe pour d'autres valeurs de λ . Afin de souligner la différence entre ces courbes, j'ai représenté sur la figure 5.19 (b) la position du maximum de contraste par

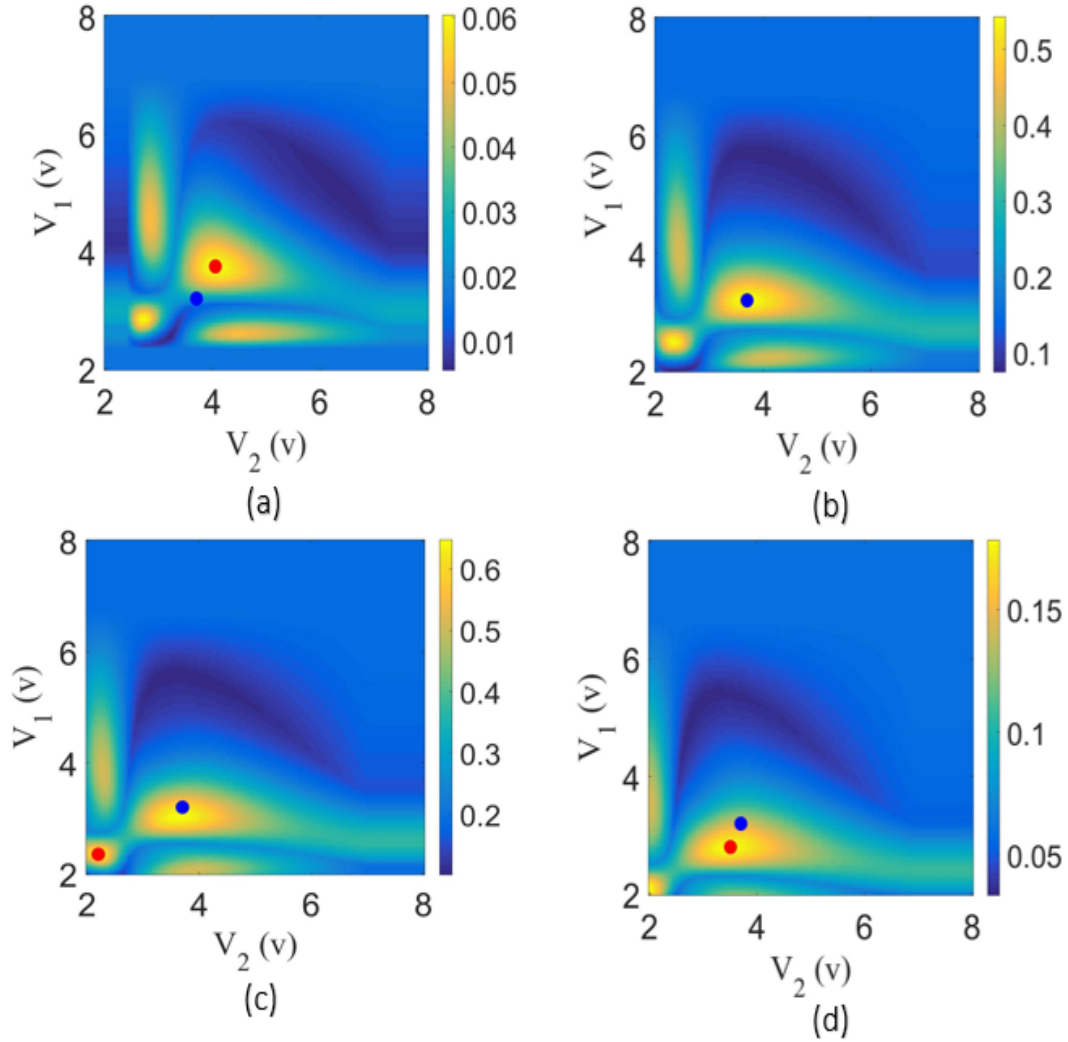


Figure 5.19: Cartes de contraste en fonction des tensions (θ_1, θ_2) (a) 450 nm (b) 550 nm (c) 600 nm (d) 700 nm. Le point bleu sur toutes les cartes représente les coordonnées $(\theta_{1,opt}^\lambda)$ du maximum de contraste à $\lambda = 550$ nm. Le point rouge sur les cartes (a), (c) and (d) représente les coordonnées $(\theta_{1,opt}^\lambda)$ du maximum de contraste à leurs longueurs d'onde respectives.

un point bleu. Sur les autres images de cette figure, correspondant à d'autres valeurs de λ , j'ai représenté par un point bleu la position du maximum du contraste pour cette longueur d'onde et par un point rouge la position du maximum de contraste pour $\lambda = 550\text{nm}$. On peut constater que les points rouges et bleus ne sont pas superposés, ce qui signifie qu'il n'y a pas un unique jeu de tensions $(\theta_{1,\text{opt}}^\lambda, \theta_{2,\text{opt}}^\lambda)$ qui donne un optimum de contraste commun à toutes ces longueurs d'ondes.

Si on implémente les tensions de commande optimales pour $\lambda = 550\text{nm}$ sur le système et qu'on élargit le spectre d'illumination, on constate l'effet des deux tendances antagonistes qui s'exercent sur le contraste. D'une part, l'augmentation du flux de photons entraîne une amélioration du contraste. De fait, si la scène et le système d'imagerie étaient indépendants de λ , le contraste de l'équation (5.12) aurait l'expression suivante:

$$C_{\Delta\lambda} = C_0 \times (\Delta\lambda)^2 \quad (5.13)$$

où $C_0 = \tau^2 \rho(\lambda_0) C_\lambda(\theta_{1,\text{opt}}^\lambda, \theta_{2,\text{opt}}^\lambda) / 4\sigma^2$ et λ_0 est la longueur d'onde centrale du filtre spectral. Le contraste varierait donc comme le carré de la largeur spectrale, comme représenté sur la figure ?? (ligne verte).

D'autre part, en raison de la dépendance spectrale de la scène, du PSG et du PSA, la configuration choisie $(\theta_{1,\text{opt}}^\lambda, \theta_{2,\text{opt}}^\lambda)$, optimale pour 550 nm ne l'est plus pour les autres longueurs d'onde. La ligne bleue représente l'évolution du contraste défini dans l'équation (5.12) lorsque les tensions de commande sont optimales pour $\lambda = 550\text{ nm}$. On constate que dans ce cas, l'augmentation du flux de photon compense toujours la perte de précision polarimétrique puisque le contraste augmente toujours lorsque le spectre s'élargit. La perte de contraste comparée au cas idéal $C_0 \Delta\lambda^2$ reste cependant importante. Enfin, si on recherche la configuration (θ_1, θ_2) qui maximise le contraste de l'équation (5.12) pour chaque valeur de la largeur spectrale, on peut voir que le contraste peut être encore augmenté (courbe rouge en pointillés sur la figure ??).

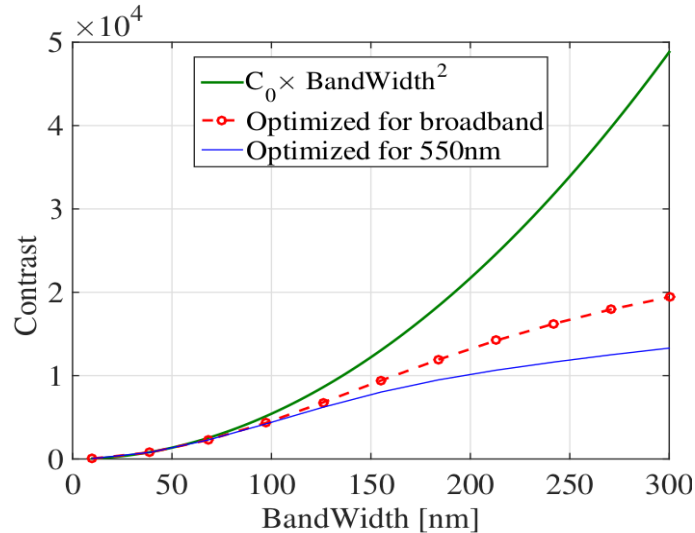


Figure 5.20: Contraste en fonction de la largeur spectrale, avec $\tau^2/\sigma^2 = 1$.

Optimisation de la largeur spectrale de l'illumination à partir de mesure spectrales de la matrice de Mueller

J'ai ensuite vérifié expérimentalement les conclusions réalisées sur ces simulations. Pour cela, j'ai utilisé une scène synthétique composée de deux zones en papier de verre de caractéristiques identiques recouvertes

de morceaux de bande adhésive transparente d'épaisseurs et d'orientations différentes. Le schéma de la scène est représenté sur la figure 5.21(a). Nous définissons la zone centrale comme la cible et l'autre comme le fond. La figure 5.21(b) montre une image d'intensité standard de cette scène, on constate que les deux régions ne sont pas distinguables l'une de l'autre à l'oeil nu. .

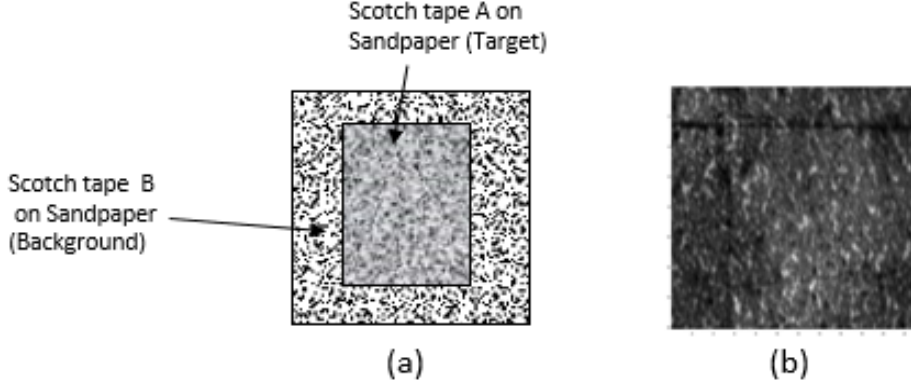


Figure 5.21: (a) Schéma de la scène. (b) Image d'intensité de la scène, $\tau = 300$ ms.

L'objectif est de déterminer les tensions de commande qui permettent d'optimiser le contraste pour différentes valeurs de la largeur spectrale. Se pose tout d'abord un problème de d'optimisation. En effet, comme le contraste de l'équation (5.11) dépend des propriétés spectrales du PSG, du PSA et des matrices de Mueller de la scène, celles-ci doivent être connues. Les réponses spectrales du PSA et du PSG ont été calibrées sur l'imagerie polarimétrique utilisé au laboratoire. D'autre part, les matrices de Mueller spectrales de la scène ont été estimées à différentes longueurs d'onde allant de 450 nm to 700 nm. Les matrices de Mueller moyennes normalisées de la cible et du fond sont représentées sur la figure 5.22. On peut constater qu'elles ont une forme très proche de celles d'un retardateur partiel, ce qui s'explique par la présence du ruban adhésif, légèrement biréfringent.

Pour cette scène, j'ai déterminé les configurations optimales du PSA et du PSG en fonction de la largeur de bande $\Delta\lambda$ de l'illumination:

$$(\theta_{1,opt}^{\Delta\lambda}, \theta_{2,opt}^{\Delta\lambda}) = \underset{\theta_1, \theta_2}{\operatorname{argmax}} [C_{\Delta\lambda}(\theta_1, \theta_2)]. \quad (5.14)$$

Pour le calcul de ce contraste, j'ai remplacé l'intégrale de l'équation (5.11) par une somme discrète sur les longueurs d'ondes auxquelles les matrices de Mueller spectrales ont été estimées:

$$C_{\Delta\lambda}(\theta_1, \theta_2) = \frac{\tau^2}{32\sigma^2} \left(\sum_{\lambda=\lambda_i}^{\lambda=\lambda_f} \rho(\lambda) [\chi_{\theta_1}(\lambda) + \mathbf{t}_{\theta_2}^T(\lambda) u_{\theta_1}(\lambda)] \delta\lambda \right)^2, \quad (5.15)$$

où $\delta\lambda = \frac{\lambda_f - \lambda_i}{n}$. Les symboles λ_i , λ_f , n , et $\delta\lambda$ représentent respectivement la longueur d'onde initiale, finale, le nombre de division de la bande spectrale et le pas en longueur d'onde.

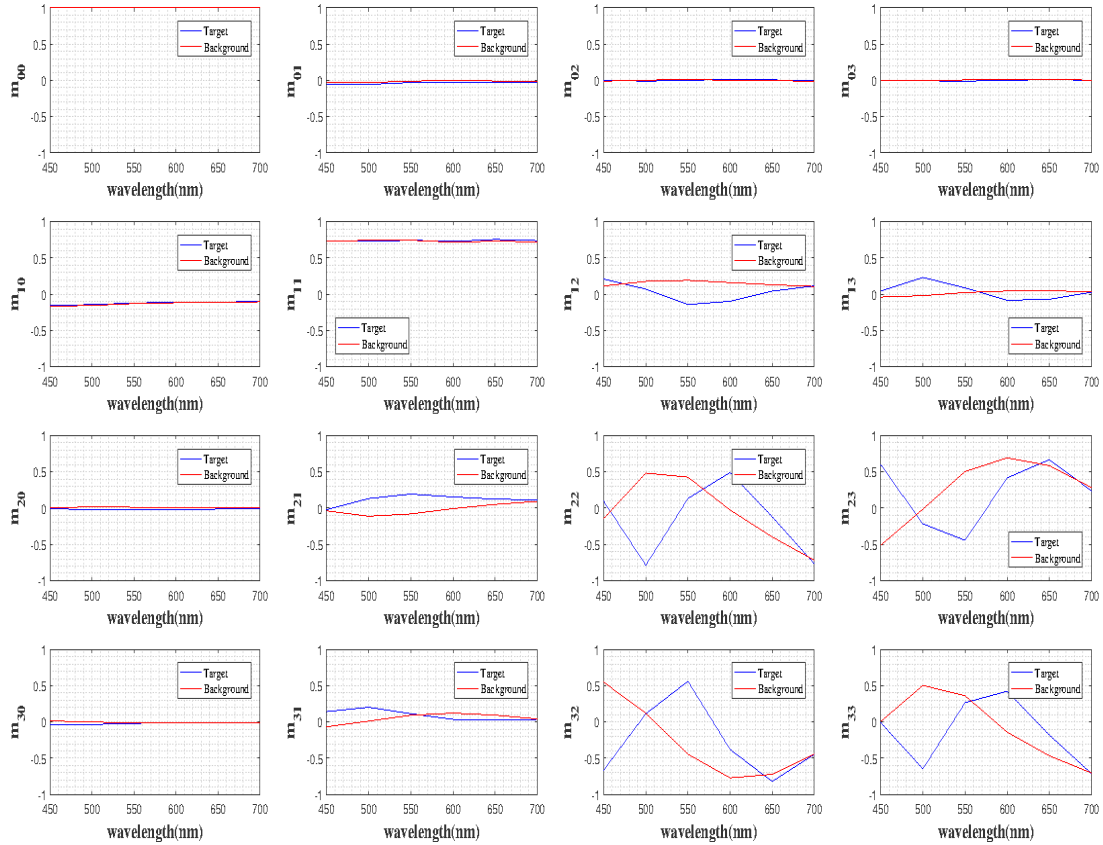


Figure 5.22: Matrice de Mueller normalisée des régions choisies comme cible et fond. Les matrices sont normalisées par rapport au coefficient M_{11} . Les 16 éléments de la matrice sont tracés en fonction de la longueur d'onde en allant de 450 nm à 700 nm par pas de 50 nm.

Les tension optimales déterminées ont ensuite été implémentées sur l'imageur polarimérique. J'ai obtenu les images représentées sur la figure 5.23. On constate clairement qu'il existe un optimum du contraste sur l'image 5.23.b, qui correspond à une largeur spectrale de 100 nm.

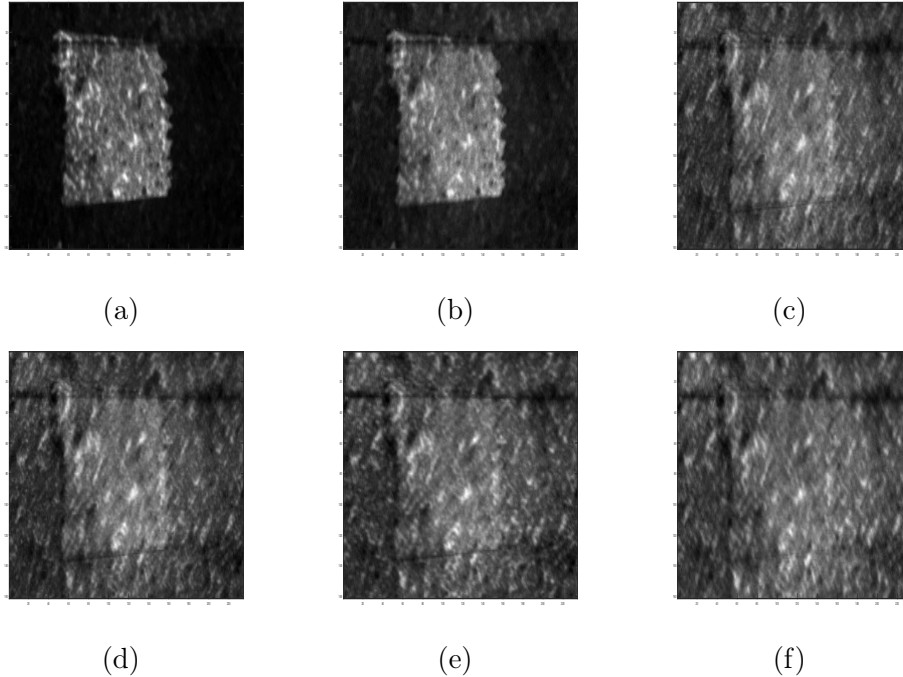


Figure 5.23: Images à contraste optimisé pour différentes dynamiques spectrales, $\Delta\lambda_R$ (et différentes largeurs spectrales, $\Delta\lambda$) (a) 550 nm (10 nm) (b) 500 nm - 550 nm (100 nm) (c) 500 nm - 600 nm (150 nm) (d) 450 nm - 600 nm (200 nm) (e) 450 nm - 650 nm (250 nm) (f) 450 nm - 700 nm (300 nm). Temps d'intégration total de la caméra, $\tau = 300$ ms.

Microscopie à contraste de phase basée sur la polarisation

Dans la dernière partie de ma thèse, j'ai appliqué mon expertise en imagerie polarimétrique à un autre domaine de recherche. J'ai collaboré avec l'entreprise Carl Zeiss pour concevoir un prototype de microscope à contraste de phase basé sur la polarisation.

La microscopie de contraste de phase permet de faire l'image d'objets transparents qui n'apparaissent pas dans les images de microscopie classique. Il existe différentes méthodes pour mettre en œuvre ce type de microscopie. Celle que j'ai étudiée repose sur l'acquisition de deux images produites par illuminations obliques et symétriques générées à partir d'un panneau de LED. Dans la version classique de cette technique, chacune des deux images est acquise de manière successive en allumant alternativement une moitié du panneau de LED. L'objectif du projet était de s'affranchir de cet éclairage alternatif en couvrant chaque moitié du panneau de LED par deux polariseurs orientés de manière orthogonale. La séparation des deux moitiés de l'éclairage se fait avec une caméra dont chaque pixel est sensible à une des polarisation. Ainsi, on réalise une image de contraste de phase à partir de l'acquisition d'une seule image, et on supprime l'éclairage alternatif qui peut être gênant pour l'observateur.

J'ai réalisé une preuve de concept de cette technique. Comme nous ne disposons pas d'une caméra polarimétrique pixellisée, j'ai utilisé une caméra classique précédée devant laquelle on place alternativement des analyseurs de directions orthogonales. Les effets du processus d'interpolation qui aurait lieu dans une

caméra polarimétrique pixellisée ont été simulés numériquement.

La figure 5.24 montre un exemple d'images obtenues. L'échantillon observé est une fine section ($15\mu\text{m}$ d'épaisseur) d'un petit poisson. Comparons tout d'abord l'image obtenue par imagerie de contraste de phase classique utilisant deux illuminations successives (DPC, Figure 5.24.a) et l'image de contraste de phase en polarisation, utilisant les deux polariseurs en illumination et en analyse (PDPC, Figure 5.24.b). Les images 5.24.d et 5.24.e représentent des extraits des deux images précédentes. On constate que ces deux images sont très semblables, ce qui valide le principe de remplacer l'illumination alternative par des polariseurs. Les figures 5.24.c et 5.24.f représentent l'image PDPC où l'interpolation des pixels de même polarisation qui aurait lieu dans le système réel a été simulée numériquement. On constate qu'elle reste proche de l'image PDPC non-interpolée, bien que légèrement plus floue.

Des analyses plus poussées ont démontré que la méthode mise en oeuvre est une alternative prometteuse à la technique d'illumination successive lorsque les échantillons observés sont "neutres" polarimétriquement. Lorsque ce n'est pas le cas (échantillon présentant de la biréfringence par exemple) cette propriété interfère avec les deux polarisations d'illumination. Une perspective intéressante à ce travail est d'étudier les moyens de rendre la méthode développée robuste à ce type d'échantillons.

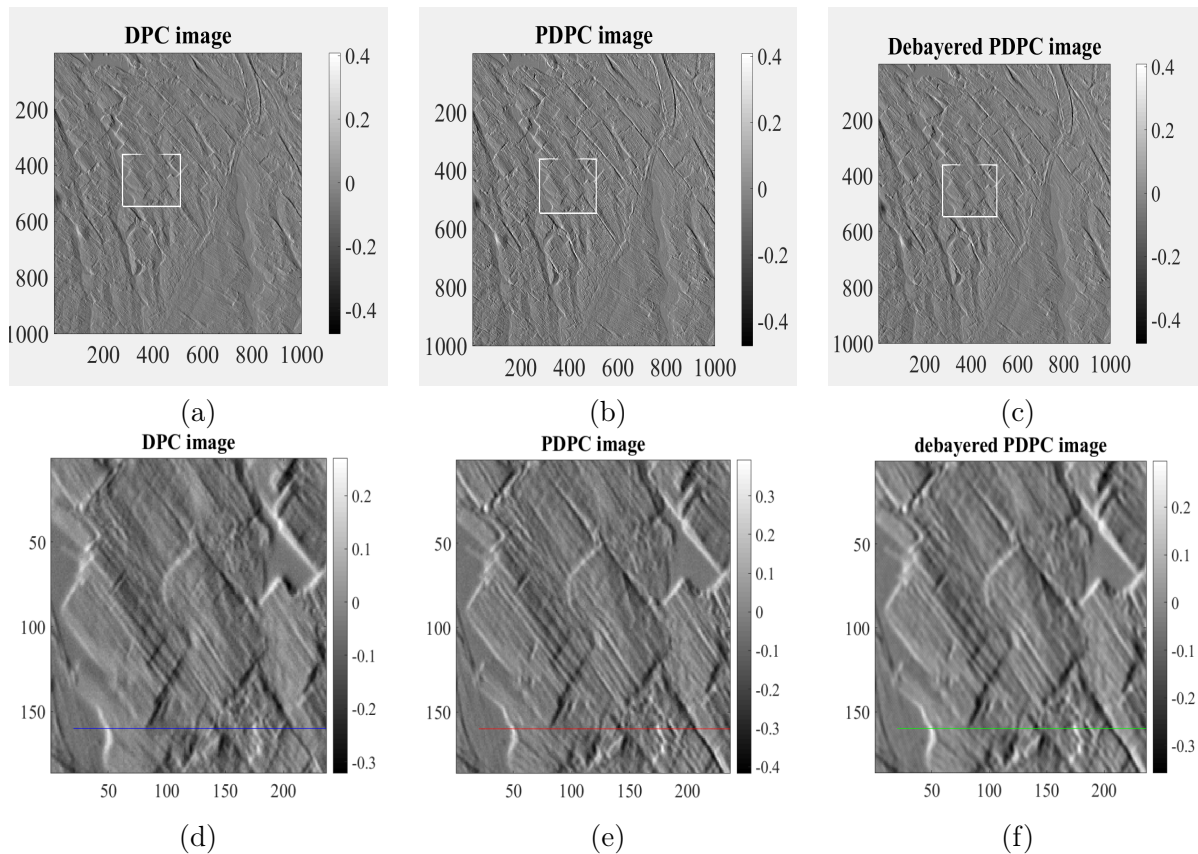


Figure 5.24: Comparaison des images DPC et PDPC d'une fine section ($15\mu\text{m}$ d'épaisseur) d'un petit poisson. (a) Image DPC (b) Image PDPC (c) Image PDPC interpolée (d) Zoom de la région entourée d'un carré blanc sur la figure 5.24.a (e) Zoom de la figure 5.24.b (f) Zoom de la figure 5.24.c.

Conclusion

Dans ce travail de thèse, j'ai démontré qu'il est possible d'augmenter de manière significative le contraste dans une image polarimétrique active même lorsque l'illumination est large spectralement et que les composants de l'imageur ont des propriétés polarimétriques chromatiques. En effet, l'augmentation du flux de photons rendue possible par la suppression filtre spectral compense dans de nombreux cas la perte de précision polarimétrique due aux propriétés chromatiques des composants.

A partir de simulations et d'expériences réelles, j'ai montré qu'il existe une largeur spectrale d'illumination optimale permettant de maximiser le contraste. En d'autres termes, la largeur spectrale d'illumination peut être considérée comme un paramètre supplémentaire dans l'optimisation d'un système d'imagerie polarimétrique actif. La perspective la plus intéressante de ce travail est de prendre en compte l'aspect multi-spectral, en mesurant une image à différentes longueurs d'ondes. Dans ce cas, il faudra déterminer à la fois le nombre optimal de bandes spectrales et leurs largeurs optimales en fonction de la scène ou de l'ensemble de scènes observé. Une autre perspective est de prendre en compte des modèles de bruit plus réalistes que le bruit additif gaussien qui a été considéré dans cette étude.

J'ai également démontré au cours de cette thèse qu'une technique polarimétrique permet d'accélérer et de simplifier les mesures de microscopie à contraste de phase pour des échantillons non-biréfringents. L'étude des échantillons présentant des propriétés polarimétriques à l'aide de cette technique est la perspective naturelle de ce travail.

Appendix A

Optimal contrast in the case of pure retarders for monoband architecture

Let us consider a scene where the target and the background are pure retarders. Their Mueller matrix can thus be expressed as $\mathbf{M}_\bullet = \mathbf{R}(\phi_\bullet^\lambda, \alpha_\bullet)$ where α_\bullet is the orientation of the retarder and ϕ_\bullet^λ the induced phase delay. The Mueller matrices can thus be rewritten in the form

$$\mathbf{M}_\bullet(\lambda) = \begin{bmatrix} 1 & \mathbf{0}^T \\ \mathbf{0} & \tilde{\mathbf{M}}_\bullet(\lambda) \end{bmatrix}$$

where $\tilde{\mathbf{M}}_\bullet(\lambda)$ is a rotation matrix. For the sake of readability, we will not write explicitly the dependence over λ in the remainder of the appendix.

With simple calculus it can be shown that the expression of the contrast in Equation (2.20) and of the optimal Stokes vector in Eq. (2.21) can be simplified as follows

$$C_\lambda(\boldsymbol{\theta}_1, \boldsymbol{\theta}_2) = \frac{\tau^2}{4\sigma^2} (\rho \mathbf{t}_{\boldsymbol{\theta}_2}^T \mathbf{D} \mathbf{s}_{\boldsymbol{\theta}_1})^2 \quad (\text{A.1})$$

$$\mathbf{t}_{\boldsymbol{\theta}_2^{\text{opt}}} = \frac{\mathbf{D} \mathbf{s}_{\boldsymbol{\theta}_1}}{\|\mathbf{D} \mathbf{s}_{\boldsymbol{\theta}_1}\|} \quad (\text{A.2})$$

and one can see that

$$C_\lambda(\boldsymbol{\theta}_1, \boldsymbol{\theta}_2^{\text{opt}}) = C_\lambda^{\text{opt}}(\boldsymbol{\theta}_1) = \frac{\tau^2}{4\sigma^2} \rho^2 \mathbf{s}_{\boldsymbol{\theta}_1}^T \mathbf{D}^T \mathbf{D} \mathbf{s}_{\boldsymbol{\theta}_1} \quad (\text{A.3})$$

If we now perform the singular value decomposition of the matrix \mathbf{D} , we obtain

$$\mathbf{D} = \mathbf{X}^T \boldsymbol{\Lambda} \mathbf{Y} \quad (\text{A.4})$$

where \mathbf{X} and \mathbf{Y} are unitary matrices, and $\boldsymbol{\Lambda}$ is a diagonal matrix with the singular values of \mathbf{D} on the diagonal. Using Eq. (A.4) in Eq. (A.3), we get

$$C_\lambda^{\text{opt}}(\boldsymbol{\theta}_1) = C_\lambda^{\text{opt}}(\mathbf{y}) = \frac{\tau^2}{4\sigma^2} \rho^2 \mathbf{y}^T \boldsymbol{\Lambda}^T \boldsymbol{\Lambda} \mathbf{y} \quad (\text{A.5})$$

where $\mathbf{y} = \mathbf{Y} \mathbf{s}_{\boldsymbol{\theta}_1}$ with $\mathbf{y} = [y_1, y_2, y_3]^T$ and $\|\mathbf{y}\| = 1$.

Moreover, it can be shown that, if the target and background are both pure retarders, \mathbf{D} possesses two non null identical eigenvalues, noted ℓ in the following. Therefore, $\boldsymbol{\Lambda}$ is of the form

$$\boldsymbol{\Lambda} = \begin{pmatrix} \ell & 0 & 0 \\ 0 & \ell & 0 \\ 0 & 0 & 0 \end{pmatrix}$$

and the contrast can be written as

$$C_{\lambda}^{\text{opt}}(\mathbf{y}) = \zeta^2 \|\mathbf{\Lambda}\mathbf{y}\|^2 = \zeta^2 \ell^2 [y_1^2 + y_2^2] \quad (\text{A.6})$$

with $\zeta = \tau\rho/2\sigma$. Therefore, the optimal contrast is obtained for any vector \mathbf{y} verifying $y_1^2 + y_2^2 = 1$ and thus for which $y_3 = 0$. The vectors that verify this condition can be written as

$$\mathbf{y} = \begin{pmatrix} \cos(\theta) \\ \sin(\theta) \\ 0 \end{pmatrix}$$

for any value of $\theta \in [0, 2\pi]$. Therefore, there is a infinite number of configurations that lead to a maximum contrast.

Bibliography

- [1] Steven L Jacques, Jessica C Ramella-Roman, and Ken Lee. Imaging skin pathology with polarized light. *Journal of biomedical optics*, 7(3):329–340, 2002.
- [2] J Scott Tyo, Dennis L Goldstein, David B Chenault, and Joseph A Shaw. Review of passive imaging polarimetry for remote sensing applications. *Applied optics*, 45(22):5453–5469, 2006.
- [3] Olivier Morel, Florence Toti, Bénédicte Hugel, Babé Bakouboula, Laurence Camoin-Jau, Françoise Dignat-George, and Jean-Marie Freyssinet. Procoagulant microparticles. *Arteriosclerosis, thrombosis, and vascular biology*, 26(12):2594–2604, 2006.
- [4] Michael Richert, Xavier Orlik, and Antonello De Martino. Adapted polarization state contrast image. *Optics express*, 17(16):14199–14210, 2009.
- [5] M Felton, KP Gurton, JL Pezzaniti, DB Chenault, and LE Roth. Measured comparison of the crossover periods for mid-and long-wave ir (mwir and lwir) polarimetric and conventional thermal imagery. *Optics express*, 18(15):15704–15713, 2010.
- [6] Angelo Pierangelo, André Nazac, Abdelali Benali, Pierre Validire, Henri Cohen, Tatiana Novikova, Bicher Haj Ibrahim, Sandeep Manhas, Clément Fallet, Maria-Rosaria Antonelli, et al. Polarimetric imaging of uterine cervix: a case study. *Optics express*, 21(12):14120–14130, 2013.
- [7] Julien Fade, Swapnesh Panigrahi, Anthony Carré, Ludovic Frein, Cyril Hamel, Fabien Bretenaker, Hema Ramachandran, and Mehdi Alouini. Long-range polarimetric imaging through fog. *Applied optics*, 53(18):3854–3865, 2014.
- [8] Nicolas Vannier, François Goudail, Corentin Plassart, Matthieu Boffety, Patrick Feneyrou, Luc Leviandier, Frédéric Galland, and Nicolas Bertaux. Active polarimetric imager with near infrared laser illumination for adaptive contrast optimization. *Applied optics*, 54(25):7622–7631, 2015.
- [9] Silvano Fineschi, Luca Zangrilli, Guglielmo Rossi, Luca Gori, Marco Romoli, Gianni Corti, Gerardo Capobianco, Ester Antonucci, and Emanuele Pace. Kpol: liquid crystal polarimeter for k-corona observations from the score coronagraph. In *Proc. SPIE*, volume 5901, page 59011I, 2005.
- [10] Nathan J Pust and Joseph A Shaw. Dual-field imaging polarimeter using liquid crystal variable retarders. *Applied optics*, 45(22):5470–5478, 2006.
- [11] Ying Zhang, Huijie Zhao, and Na Li. Polarization calibration with large apertures in full field of view for a full stokes imaging polarimeter based on liquid-crystal variable retarders. *Applied optics*, 52(6):1284–1292, 2013.
- [12] R Oldenbourg and G Mei. New polarized light microscope with precision universal compensator. *Journal of microscopy*, 180(2):140–147, 1995.

- [13] Guillaume Anna, Hervé Sauer, François Goudail, and Daniel Dolfi. Fully tunable active polarization imager for contrast enhancement and partial polarimetry. *Applied optics*, 51(21):5302–5309, 2012.
- [14] Matthieu Boffety, Haofeng Hu, and François Goudail. Contrast optimization in broadband passive polarimetric imaging. *Optics letters*, 39(23):6759–6762, 2014.
- [15] Emil Wolf. *Progress in optics*. Elsevier Science, 2009.
- [16] Edward Collett. *Field guide to polarization*. SPIE Bellingham, WA, 2005.
- [17] Dennis H Goldstein. *Polarized light*. CRC press, 2016.
- [18] Francisco J Duarte. Optical device for rotating the polarization of a light beam, April 18 1989. US Patent 4,822,150.
- [19] Serge Huard. *Polarisation de la lumière*. 1994.
- [20] Shih-Yau Lu and Russell A. Chipman. Interpretation of mueller matrices based on polar decomposition. *J. Opt. Soc. Am. A*, 13(5):1106–1113, May 1996.
- [21] Russell A Chipman. Handbook of optics. *Polarimetry, 2nd ed. M. Bass ed. McGraw Hill, New York*, 2, 1995.
- [22] Russell A Chipman, Elizabeth A Sornsin, and J Larry Pezzaniti. Mueller matrix imaging polarimetry: An overview. In *International Symposium on Polarization Analysis and Applications to Device Technology*, pages 5–12. International Society for Optics and Photonics, 1996.
- [23] Guillaume Anna and François Goudail. Optimal mueller matrix estimation in the presence of poisson shot noise. *Optics express*, 20(19):21331–21340, 2012.
- [24] MP Rowe, JS Tyo, N Engheta, and EN Pugh. Polarization-difference imaging: a biologically inspired technique for observation through scattering media. *Optics letters*, 20(6):608–610, 1995.
- [25] Arnaud Bénéière, Mehdi Alouini, François Goudail, and Daniel Dolfi. Design and experimental validation of a snapshot polarization contrast imager. *Applied optics*, 48(30):5764–5773, 2009.
- [26] Steven M Kay. *Fundamentals of statistical signal processing, vol. ii: Detection theory. Signal Processing. Upper Saddle River, NJ: Prentice Hall*, 1998.
- [27] François Goudail, Philippe Réfrégier, and Guillaume Delyon. Bhattacharyya distance as a contrast parameter for statistical processing of noisy optical images. *JOSA A*, 21(7):1231–1240, 2004.
- [28] Thomas M Cover and Joy A Thomas. *Elements of information theory*. John Wiley & Sons, 2012.
- [29] H Vincent Poor. Elements of hypothesis testing. In *An introduction to signal detection and estimation*, pages 5–44. Springer, 1994.
- [30] Osamu Matoba and Bahram Javidi. Three-dimensional polarimetric integral imaging. *Optics letters*, 29(20):2375–2377, 2004.
- [31] Firooz A Sadjadi. Passive three-dimensional imaging using polarimetric diversity. *Optics letters*, 32(3):229–231, 2007.

- [32] Francois Parnet, Julien Fade, Noé Ortega-Quijano, Ludovic Frein, Mehdi Alouini, et al. Free-space active polarimetric imager operating at $1.55 \mu\text{m}$ by orthogonality breaking sensing. *Optics Letters*, 42(4):723–726, 2017.
- [33] Sophie Brasselet. Polarization-resolved nonlinear microscopy: application to structural molecular and biological imaging. *Advances in Optics and Photonics*, 3(3):205, 2011.
- [34] Michael Shribak. Complete polarization state generator with one variable retarder and its application for fast and sensitive measuring of two-dimensional birefringence distribution. *JOSA A*, 28(3):410–419, 2011.
- [35] KM Twietmeyer and RA Chipman. Optimization of mueller matrix polarimeters in the presence of error sources. *Optics express*, 16(15):11589–11603, 2008.
- [36] S Chandrasekhar. Liquid crystals, (1992). *Cambridge University, Cambridge*.
- [37] Jörg Schirmer and Theodor Schmidt-Kaler. Liquid crystal phase retarder with broad spectral range. *Optics Communications*, 176(4):313–317, 2000.
- [38] Lijo Thomas, Matthieu Boffety, and François Goudail. Improving target discrimination ability of active polarization imagers by spectral broadening. *Optics express*, 23(26):33514–33528, 2015.
- [39] Lijo Thomas, Haofeng Hu, Matthieu Boffety, and François Goudail. Contrast optimization in broadband polarimetric imaging. In *SPIE Commercial+ Scientific Sensing and Imaging*, pages 98530K–98530K. International Society for Optics and Photonics, 2016.
- [40] François Goudail. Optimal mueller matrix estimation in the presence of additive and poisson noise for any number of illumination and analysis states. *Optics Letters*, 42(11):2153–2156, 2017.
- [41] Guillaume Anna, François Goudail, and Daniel Dolfi. Polarimetric target detection in the presence of spatially fluctuating mueller matrices. *Optics letters*, 36(23):4590–4592, 2011.
- [42] Frits Zernike. Phase contrast, a new method for the microscopic observation of transparent objects. *Physica*, 9(7):686–698, 1942.
- [43] G Nomarski. Differential microinterferometer with polarized waves. *J. Phys. Radium*, 16(9):9S–11S, 1955.
- [44] DK Hamilton and CJR Sheppard. Differential phase contrast in scanning optical microscopy. *Journal of microscopy*, 133(1):27–39, 1984.
- [45] Bechara Kachar. Asymmetric illumination contrast: a method of image formation for video light microscopy. *Science*, 227(4688):766–768, 1985.
- [46] Shalin B Mehta and Colin JR Sheppard. Quantitative phase-gradient imaging at high resolution with asymmetric illumination-based differential phase contrast. *Optics letters*, 34(13):1924–1926, 2009.
- [47] Guoan Zheng, Christopher Kolner, and Changhui Yang. Microscopy refocusing and dark-field imaging by using a simple led array. *Optics letters*, 36(20):3987–3989, 2011.
- [48] Lei Tian, Jingyan Wang, and Laura Waller. 3d differential phase-contrast microscopy with computational illumination using an led array. *Optics letters*, 39(5):1326–1329, 2014.

- [49] Lei Tian and Laura Waller. Quantitative differential phase contrast imaging in an led array microscope. *Optics express*, 23(9):11394–11403, 2015.
- [50] Guillaume Anna, François Goudail, Pierre Chavel, and Daniel Dolfi. On the influence of noise statistics on polarimetric contrast optimization. *Applied optics*, 51(8):1178–1187, 2012.

Titre : Imagerie polarimétrique active à large spectre pour l'amélioration du contraste et la microscopie

Mots clefs : imagerie polarimétrique, traitement du signal, microscope de contraste de phase, imagerie multispectrale

Résumé : L'imagerie de polarisation est une technique permettant de révéler des contrastes qui n'apparaissent pas dans les images d'intensité classiques. En d'autres termes, elle permet de transformer une différence de propriétés polarimétriques en différence de niveau de gris. Elle trouve des applications en décamouflage, télédétection, microscopie, etc. Les imageurs polarimétriques utilisent souvent des modulateurs de polarisation basés sur des matrices de cristaux liquides rapides et fiables. Cependant, les LCVR contrôlent l'état de polarisation de la lumière à seulement une longueur d'onde donnée, et si le système est utilisé à d'autres longueurs d'ondes, il a des performances réduites. Si la lumière qui illumine la scène à un spectre large, il est donc nécessaire d'insérer un filtre spectral de bande étroite dans la voie d'imagerie, ce qui a pour effet de réduire la quantité de lumière entrant dans le système et donc le rapport signal à bruit des images.

Un moyen de résoudre ce problème est d'utiliser des modulateurs de polarisation achromatiques, mais cela induit un coût et une complexité accrus qui peuvent ne pas être nécessaires si l'objectif est d'améliorer la performance de détection de cible en augmentant le contraste entre l'objet d'intérêt et le fond. Dans cette thèse, j'étudie l'impact d'un élargissement du spectre d'illumination sur la performance de détection de cible par des systèmes d'imagerie polarimétriques utilisant des composants chromatiques. A travers des simulations, je montre tout d'abord qu'élargir le spectre d'illumination peut augmenter le contraste car l'augmentation du flux de lumière compense la perte de précision polarimétrique. De plus, en prenant en compte les caractéristiques polarimétriques chromatiques des composants, on peut accroître encore l'augmentation du contraste. Ces résultats sont ensuite validés à travers des expériences réelles d'imagerie polarimétrique active. Ils

démontrent que la largeur du spectre d'éclairage peut être considérée comme un paramètre additionnel pour optimiser ces systèmes d'imagerie. Afin de mettre en pratique l'expertise acquise en imagerie polarimétrique active à un autre domaine, j'ai collaboré avec un partenaire industriel (Carl Zeiss, Germany) pour doter un microscope optique d'une capacité polarimétrique. L'imagerie d'un échantillon fin et transparent est un problème difficile. Par exemple, la coloration de l'échantillon peut ajouter des détails parasites et n'est pas applicable à l'imagerie du vivant. Une technique prometteuse est le contraste de phase différentiel (DPC) qui consiste à extraire le gradient de phase de l'objet à partir de deux images illuminées de manière asymétrique et acquises selon des angles complémentaires. La source de lumière est une matrice de LED programmables qui peut générer différents motifs d'illumination. Cependant, cette méthode d'imagerie prend du temps et les flashes intermittents émis par la source peuvent rendre l'observation inconfortable.

J'ai donc proposé une solution alternative consistant à installer deux polariseurs avec des axes orthogonaux devant la source de lumière et une caméra sensible à la polarisation qui peut détecter simultanément des polarisations orthogonales. La lumière polarisée atteint la caméra sensible à la polarisation après avoir traversé l'échantillon transparent. Les composantes orthogonales sont extraites de l'image acquise par un procédé de débayerisation. A travers différentes expériences, je compare les performances de cette méthode innovante avec la méthode de DPC classique. Je montre qu'elles fournissent des qualités d'images similaires dans la plupart des cas alors que la nouvelle méthode permet de diviser le temps d'acquisition par deux, tout en supprimant les flashes intermittents.

Title : Broadband active polarization imaging for contrast improvement and microscopy

Keywords : polarization imaging, phase contrast microscopy, signal processing, multispectral imaging

Abstract : Polarization imaging is a technique which reveals contrasts that do not appear in classical intensity images. It transforms the difference in polarimetric properties of a scene into difference in gray level of an image. This technique has found applications in decamouflaging, remote sensing, microscopy etc. Polarimetric imagers often use polarization modulation devices based on liquid crystal variable retarders (LCVR), which are fast and reliable. However, LCVR control the polarization state of light only at one given nominal wavelength, and performance loss might be observed if imaging is performed at other wavelengths, due to the wavelength dependence of the LCVR. If the light source that illuminates the scene has a broad spectrum, it is thus necessary to insert a narrowband spectral filter in the imaging path. However, spectral filtering significantly decreases the amount of light entering the system and thus the signal-to-noise ratio of polarimetric images.

A way to circumvent this issue is to achromatize the polarization modulators. However, this comes at the price of higher complexity and cost, and this may not be needed if the objective is to improve target detection performance by increasing the target/background discriminability (or contrast). In the thesis, we present the investigation of the impact of broadening the spectrum of the light entering the system on the discriminability performance of active polarimetric systems. Through simulations, we show that broadening the bandwidth of the illumination can increase the contrast between two regions, as the increase of light flux compensates for the loss of polarimetric precision. Moreover, we show that taking into account the chromatic characteristics of the components of the imaging system, it is possible to further enhance the contrast. We validate these findings through experiments in active polarimetric imaging configuration, and demonstrate that the spectral bandwidth can be considered as an additional parameter

to optimize polarimetric imaging set-ups.

We collaborated with an industrial partner (Carl Zeiss, Germany) to implement polarization imaging in optical microscopy. Imaging thin and transparent specimen in microscopy is a challenging task. Staining the sample is a solution but it adds false/spurious details to the image, thus not suitable for live imaging. Recently, differential phase contrast (DPC) imaging by asymmetric illumination is proved to be a desirable choice. This works on the principle that the phase gradient of a transparent specimen can be extracted from two images, illuminated and recorded at complementary angles. Then, DPC is computed as normalized difference between two images. Here the light source is programmable LED array and different pattern of illumination can be generated. This imaging method consumes more time and intermittent flash of light from light source makes sample observation inconvenient for the observer.

A practical solution we propose is to install two polarization foils with orthogonal polarization axes below the light source side by side and a polarization sensitive camera which can detect orthogonal eigen polarization states at a time in the existing setup. The polarization foils separate light waves from complementary angles since orthogonally polarized light waves do not interact with each other. The polarized light reaches polarization sensitive camera after passing through transparent sample. The pixels sensitive to horizontal and vertical polarization detect horizontal and vertical polarized light respectively. Then horizontal and vertical polarized light information are separated from the recorded image and reconstructed the missing information using debayering process. Through experiments, we show that polarization based DPC and standard DPC images have similar quality in most cases and the new technique reduces time consumption by half.